Ultrashort light pulses over large spectral ranges: novel sources and dispersion-scan-based spatiotemporal diagnostics

Miguel Noronha da Canhota

MAP-FIS doctoral Program in Physics
Department of Physics and Astronomy
Faculty of Sciences
University of Porto
2018

Supervisor
Prof. Helder Manuel Paiva Rebelo Cerejo Crespo
Dept. of Physics and Astronomy, FCUP, Portugal

Co-supervisor
Prof.ª Rosa Maria Weigand Talavera
Dept. of Optics, Faculty of Physics, Complutense
University of Madrid, Spain

Ultrashort light pulses over large spectral ranges: novel sources and dispersion-scan-based spatiotemporal diagnostics

Acknowledgments

I would like to thank my advisors Helder Crespo and Rosa Weigand. Thanks to Helder for receiving me in the femtolab and giving enough latitude to pursue my own ideas, some of which are presented in this thesis. Thanks to Rosa for the help, support and extreme patience with me.

Thanks to the people who shared the lab and/or helped me throughout these years ("*a irmandade*"), Francisco Silva (Chico), Ana Sofia (A.S. Silva), Cledson Gonçalves (*"Pé voador do Nordeste*") and Miguel Miranda (*"Aligner Extraordinaire*").

Thanks to Rosa Romero (*"Sr.ª Presidente*"), CEO of Sphere Ultrafast Photonics for lending a single-shot d-scan to perform measurements with the STARFISH technique in Salamanca, and for helpful suggestions in chapter 3.

Thanks to Benjamin Alonso and Iñigo Sola (ALF-USAL) for the collaboration work in the spatio-temporal pulse characterization (chapter 5) with the STARFISH technique.

Thanks also to Francisco Carpinteiro, Fernando (Oficina de mecânica), Pedro Cruz (Oficina de electrónica) e D. Isabel Alves (IFIMUP) for their help in the maintenance of the lab equipment as well as with the logistics and paperwork.

Last but not least, I would like to thank my family support, specially my niece Adriana, whom I hope will someday understand why the author was not always available to play.

Summary

Ultrashort laser pulses have multiple applications in spectroscopy, imaging and micromachining, as well as in basic research. It is thus important to be able both to generate and characterize ultrashort pulses. The dispersion scan (d-scan), is a temporal characterization technique for ultrashort laser pulses, based on a simple, in-line setup, capable of measuring the shortest pulses in the optical region of the electromagnetic spectrum to date. This thesis builds upon the d-scan technique and extends its applicability to the UV region of the electromagnetic spectrum.

Chapter 1 contains a brief description of the field of Nonlinear and Ultrafast Optics. In chapter 2 we make a short review on the main ultrashort pulse characterization techniques, apart from the dispersion scan. Chapter 3 contains a description of d-scan and its properties.

In chapter 4 we develop a new variant of the d-scan technique based on the nonlinear optical effect of self-diffraction, i.e., SD d-scan, and use it to characterize ultrashort pulses from a hollow-core fiber. A comparative study is made with the conventional d-scan technique based on second-harmonic generation.

Chapter 5 describes the temporal characterization by d-scan of a novel source of supercontinuum generation (in the visible and infrared part of the electromagnetic spectrum) based on using multiple thin plates (multiplate continuum, MPC), as well as a spatio-temporal characterization of the beam with the STARFISH technique.

In chapter 6 we apply the SD d-scan technique to the characterization of a novel source of broadband UV laser pulses based on MPC. Challenges to the measurement of such pulses are described, and an improvement of the SD d-scan technique is introduced, namely, the dual SD d-scan, which allows for the simultaneous retrieval of two pulses in different spatial portions of the same beam.

Chapter 7 describes the pulse retrieval of third-harmonic generation (THG) d-scan traces taken from the spectrum of the high-harmonic generation (HHG) generated in-situ, i.e., directly from a gas target, when driven from an ultrashort pulse.

Chapter 8 contains the final remarks and future prospects.

Resumo

Os impulsos laser ultra-curtos têm aplicações importantes em espectroscopia, imagiologia e micro-maquinação, e também em investigação fundamental. A capacidade de gerar, caracterizar e controlar impulsos ultra-curtos é assim muito importante. A técnica de dispersion-scan (d-scan) é uma técnica de caracterização de impulsos laser ultra-curtos baseada num sistema simples e capaz de medir os impulsos ópticos mais curtos da actualidade. Neste trabalho faz-se uma extensão da técnica de d-scan para impulsos ultra-curtos na região ultravioleta do espectro electromagnético.

O capítulo 1 contém uma breve descrição da área da óptica não-linear e ultra-rápida. No capítulo 2 fazemos uma curta revisão sobre os principais métodos de caracterização de impulsos ultra-curtos, excluindo a técnica de d-scan.No capítulo 3 descrevemos a técnica de d-scan e as suas propriedades.

No capítulo 4 desenvolvemos uma nova variante da técnica de d-scan baseada no efeito óptico não-linear de “self-diffraction” (SD d-scan) e utilizamo-la para caracterizar impulsos no regime de um único ciclo óptico (sub-4-femtosegundos) provenientes de um compressor de fibra oca, comparando os resultados com os resultados obtidos pela técnica convencional de d-scan baseada do efeito de geração de segundo harmónico.

O capítulo 5 descreve a caracterização temporal, pela técnica de d-scan, de uma nova fonte de supercontínuo na região do visível e infravermelho do espectro electromagnético, baseada em propagação não-linear em lâminas finas de vidro (MPC), assim como a caracterização espaço-temporal desta fonte através da técnica de STARFISH.

No capítulo 6 aplicamos a técnica de SD d-scan à caracterização de uma nova fonte de impulsos ultracurtos de banda larga no ultravioleta, produzida por MPC. Descrevemos os desafios com que deparamos na medida de tais impulsos, e introduzimos um melhoramento da técnica de SD d-scan, nomeadamente o dual SD d-scan, o qual nos permite a reconstrução simultânea de dois impulsos diferentes desconhecidos.

O capítulo 7 descreve a reconstrução de impulsos ultracurtos intensos a partir de dados obtidos com a técnica de d-scan baseada no fenómeno de geração de terceiro harmónico (THG) directamente num jacto gasoso usado em experiências de interacção laser-matéria no regime de altas intensidade não-perturbativo (geração de harmónicos elevados).

O capítulo 8 contém os comentários finais e considerações sobre trabalhos futuros.

List of publications

M. Canhota, F. Silva, R. Weigand, and H. M. Crespo, "Inline self-diffraction dispersion-scan of over octave-spanning pulses in the single-cycle regime," Opt. Lett. 42, 3048 (2017).

In preparation

- M. Canhota, R. Weigand, and H. Crespo,“Dual Self-diffraction d-scan for the measurement of inhomogeneous light beams”

- M. Canhota, R. Weigand, and H. Crespo,“Redundancy in the dispersion-scan technique”

- Helder Crespo, Miguel Canhota, Tobias Witting, John Tisch, “Direct measurement of intense sub-4-fs pulses in a gas target by third-harmonic dispersion-scan”

Talks

- Miguel Canhota, Francisco Silva, Rosa Weigand, Helder Crespo, "Self-Diffraction Dispersion-Scan (SD d-scan): a new ultrashort pulse characterization scheme", oral presentation at the 1st Doctoral Congress in Engineering, Doctoral Symposium in Engineering Physics, Porto, Portugal, June 13-15, 2015

- Miguel Canhota, Francisco Silva, Rosa Weigand, Helder Crespo, “Self-diffraction and transient-grating dispersion-scan and its application to the measurement of sub-4-fs pulses”, oral presentation at Ultrafast Optics – UFO 2015, Beijing, China, 16-21 August 2015

- Miguel Canhota, Francisco Silva, Rosa Weigand, Helder Crespo, “Self-diffraction dispersion-scan and its application to the measurement of over octave-spanning pulses in the single-cycle regime”, CLEO®/Europe-EQEC 2017, Munich, Germany

- H. M. Crespo, M. Canhota, T. Witting and J. W. G. Tisch "In situ characterization of intense few-pulses: towards precise control in strong field light-matter interaction", CLEO®/Europe-EQEC 2017, Munich, Germany

Posters

- Miguel Canhota, Rosa Weigand, Helder Crespo, "Dispersion-scan measurements of few-cycle pulses compressed with the multiplate continuum process", CLEO/Europe-EQEC 2017, Munich, Germany
- Miguel Canhota, Rosa Weigand, Helder Crespo, “Dual Self-Diffraction Dispersion-scan for Measuring Spatially Inhomogeneous Ultrashort Pulses”, at Ultrafast Phenomena (UP2018), July 2018, Hamburg, Germany
- Helder Crespo, Miguel Canhota, Tobias Witting, John Tisch, “Direct measurement of intense sub-4-fs pulses in a gas target by third-harmonic dispersion-scan”, at Ultrafast Phenomena (UP2018), July 2018, Hamburg, Germany

Proceedings

Miguel Canhota, Helder Crespo, Rosa Weigand, "Four-wave-mixing assisted pulse shaping of femtosecond UV pulses", Proc. SPIE 8785, 8th Iberoamerican Optics Meeting and 11th Latin American Meeting on Optics, Lasers, and Applications, 87854I (18 November 2013); doi: 10.1117/12.2026192.

Awards

EPS-QEOD Travel Grant Student Awards for CLEO®/Europe-EQEC 2017 conference.

Nomenclature

AOPDF	Acousto-optic programmable dispersive filter
CEO	Carrier-Envelope Offset
CEP	Carrier-Envelope Phase
CPA	Chirped-pulse amplification
CPA	Chirped-pulse amplification
d-scan	Dispersion Scan
DCM	Dispersion compensation mirror
FROG	Frequency Resolved Optical Gating
FTSI	Fourier transfrom spectral interferometry
HCF	Hollow-core fiber
KLM	Kerr Lens Modelocking
LC-SLM	Liquid-cyrstal spatial light modulator
MIIPS	Multiphoton Intrapulse Interference Phase Scan
MPC	Multiplate Continuum
SCG	Supercontinuum Generation
SHG	Second Harmonic Generation
SPIDER	Spectral Phase Interferometry for Direct Electric Field Reconstruction

Contents

List of Figures

List of Tables

1 Introduction

‘Listen very carefully, I shall say this only once!”

’Allo ’Allo!

1.1 Ultrashort laser pulses

Ultrashort laser pulses are laser pulses with durations in the order of picoseconds (10^{-12} s) or less. Much like the uncertainty relationship between position and momentum in quantum mechanics, quantities like the standard deviation of an ultrashort laser pulse $E(t)$ in time, σ_t, and in frequency, σ_ω, are related by the following equation [1, 2],

$$\sigma_t \sigma_\omega \geq \kappa, \tag{1.1}$$

where

$$\sigma_t^2 = \int_{-\infty}^{+\infty} t^2 \left|E(t)\right|^2 dt, \tag{1.2}$$

$$\sigma_\omega^2 = \int_{-\infty}^{+\infty} \omega^2 \left|\tilde{E}(\omega)\right|^2 d\omega, \tag{1.3}$$

where $\tilde{E}(\omega)$ is the Fourier transform of $E(t)$ and κ is a scalar of the order of unity. The chosen convention for the direct Fourier transform and inverse Fourier transform are,

$$\tilde{E}(\omega) = \int_{-\infty}^{+\infty} E(t) e^{-i\omega t} dt \tag{1.4}$$

$$E(t) = \frac{1}{2\pi} \int_{-\infty}^{+\infty} \tilde{E}(\omega) e^{i\omega t} d\omega \tag{1.5}$$

Since σ_t and σ_ω can be regarded as the “spread” of the pulse in the time and frequency, respectively, Eq. 1.1 shows that one cannot have an arbitrarily short pulse without a broad spectrum and vice-versa.

The expression for the electric field of a pulse in the time domain, $E(t)$ is given by

$$E(t) = |E(t)|\, e^{-i\phi(t)} e^{i\omega_0 t} \tag{1.6}$$

where ω_0 is the carrier frequency, and $|E(t)|$ is the pulse amplitude, which in turn is the square-root of the pulse intensity, $I(t)$, and $\phi(t)$ is the temporal phase. The pulse intensity determines the pulse profile as well as its duration which is commonly given by its fullwidth at half-maximum (FWHM). In the frequency domain, Eq. (1.6) is written as

$$\tilde{E}(\omega) = \left|\tilde{E}(\omega)\right| e^{-i\varphi(\omega)} \tag{1.7}$$

where $\varphi(\omega)$ is the spectral phase. The field expressions are not unique, as they depend on signal conventions as well as the conventions for the forward and inverse Fourier transform. Refer to Annex 1 (in section 8), for the other possible types of conventions.

For gaussian pulses, we have,

$$|E(t)| = e^{-\alpha t^2} \tag{1.8}$$

where α can be related to the pulse full-width at half-maximum (FWHM; Δt_{FWHM}) by the following relation

$$\alpha = \frac{2ln(2)}{\Delta t_{FWHM}^2} \tag{1.9}$$

In the Fourier domain, the pulse can be represented as follows

$$\tilde{E}(\nu) \propto e^{-\frac{\pi^2}{\alpha}(\nu-\nu_0)^2} \tag{1.10}$$

where $\nu = \omega/2\pi$. For sech-squared pulses,

$$|E(t)| = sech\left(\frac{t}{\tau}\right) \tag{1.11}$$

and

$$\tilde{E}(\nu) \propto sech\left[\frac{\pi^2}{\tau}(\nu - \nu_0)\right] \tag{1.12}$$

where τ is related to Δt_{FWHM}, as follows

$$\tau = \frac{\Delta t_{FWHM}}{ln\left(3 + 2\sqrt{2}\right)} \tag{1.13}$$

These pulse shapes are useful in simulations (pulse propagation, calculation of nonlinear effects, etc., since they have a known analytical expression), as well as in the estimation of pulse duration through nonlinear autocorrelations (see chapter 2).

1.1.1 Instantaneous frequency and chirp

A non-constant temporal phase leads to an temporal variation of the total phase of a pulse. The variation of $\phi(t)$ in time gives rise to a varying frequency, which will be referenced as the instantaneous frequency, $\omega_{inst}(t)$

$$\omega_{inst}(t) = \omega_0 - \frac{d\phi}{dt} \tag{1.14}$$

Let us illustrate the effect of $\phi(t)$ on the field. If $\frac{d\phi}{dt} \neq 0$ then the field has chirp, and so the pulse has a time-dependent instantaneous frequency. Consider a gaussian pulse of 8 fs of duration, centered at 800 nm (0.375 PHz) will be used, upon which we will impart a linear, a quadratic and a cubic temporal phase. From Eq. 1.14, we see that a linear temporal phase $\phi(t) = at$ will (due to the Fourier shift theorem) lead to only a shift in the pulse central frequency, having now a maximum at ~0.38 PHz, as Figure 1.1 depicts.

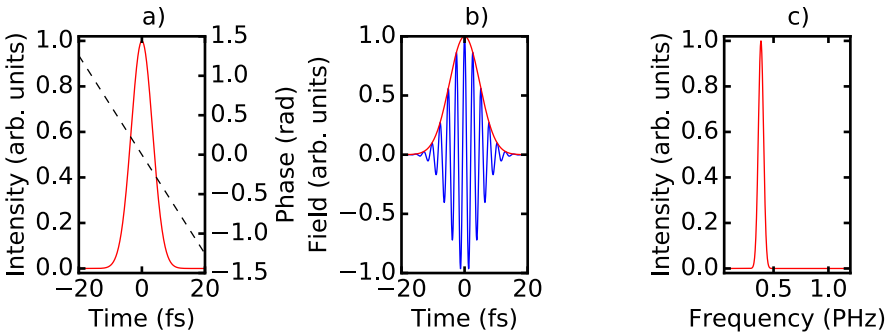

Figure 1.1: Gaussian pulse with linear temporal phase $\phi(t) = at$ ($a = -2\pi \times 10^{13}$ rad s^{-1}). a) Pulse profile (red), temporal phase (dashed black). b) Pulse electric field (blue), pulse amplitude (red). c) Pulse spectrum, was shifted by ~0.01 THz from the original value of 0.375 PHz.

A quadratic temporal phase $\phi(t) = bt^2$ leads to a linear variation (also known as linear chirp) of $\omega_{inst}(t)$, which translates into an increase of the frequency of oscillation of the electric field as seen in Figure 1.2. For our sign convention, if $b < 0$ the chirp is positive and longer wavelengths arrive before shorter wavelengths. If $b > 0$ the chirp is negative and shorter wavelengths arrive before longer ones. This quadratic term also contributes

for the broadening of the spectrum of the pulse (Figure 1.2c).

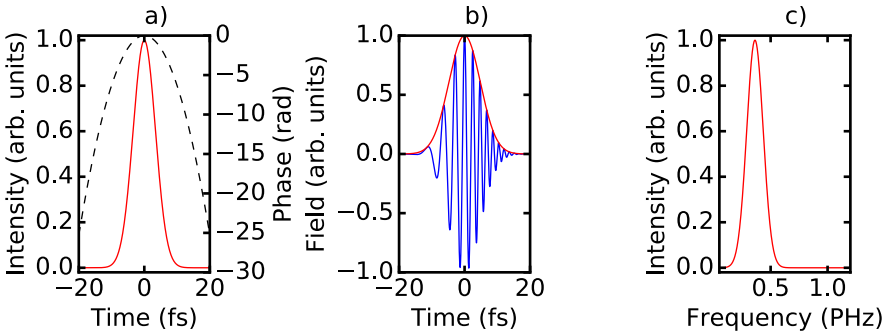

Figure 1.2: Gaussian pulse with quadratic temporal phase $\phi(t) = bt^2$ ($b = -(8\pi \times 10^{13})^2$ rad s^{-2}). a) Pulse profile (red), temporal phase (dashed black). b) Pulse electric field (blue), pulse amplitude (red). c) Pulse spectrum.

A cubic temporal phase leads to a quadratic chirp, as evidenced by the increase in the frequency of oscillation of the electric field near the pulse extremities (Figure 1.3b). The cubic temporal phase is also responsible for the emergence of pre- or post-peaks in the spectrum (Figure 1.3c)).

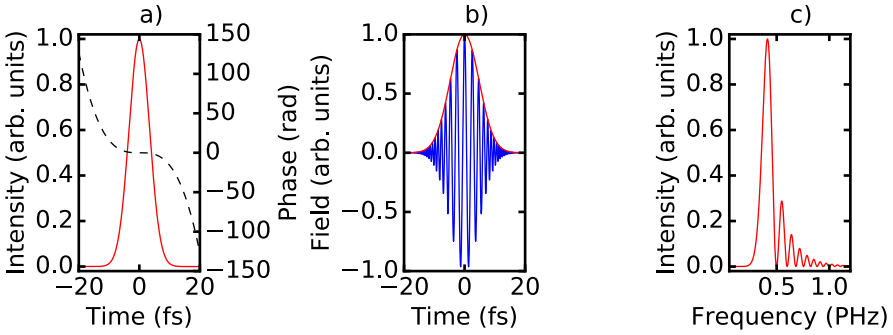

Figure 1.3: Gaussian pulse with cubic temporal phase $\phi(t) = ct^3$ ($c = -(8\pi \times 10^{13})^3$ rad s^{-3}). a) Pulse profile (red), temporal phase (dashed black). b) Pulse electric field (blue), pulse amplitude (red). c) Pulse spectrum.

Unlike in the case of the spectral phase, one cannot directly manipulate the temporal phase, as practically all phase modulators work in the spectral domain. The importance of the temporal phase cannot be discarded though, since the self-phase modulation effect (SPM, to be introduced later) relies on the modulation of the temporal phase for spectrum broadening. The effect of the spectral phase on the temporal profile of the pulse is described in section 1.7.

1.2 Time-Bandwidth Product (TBP)

A broad spectrum is a necessary, but not sufficient condition to have a short pulse. In fact, for a given broad spectrum we may have a relatively longer pulse than expected. This is due to existence of a non-constant spectral phase. In this section we will introduce a numerical quantity, namely, the time-bandwith product (TBP), which tell us how compressed a pulse is, i.e., how close is the actual pulse from the shortest pulse obtainable for a given spectrum.

We start by considering a gaussian pulse with central frequency ω_0 in time domain

$$E(t) = E_o e^{-\alpha t^2} e^{i\omega_0 t} \tag{1.15}$$

Its Fourier transform is given by Eq. (1.10). Both E and $\tilde{E}$ have a FWHM of Δt_{FWHM} and $\Delta\nu_{FWHM}$ respectively, which are functions that are directly or inversely proportional to α. This dependence on α can be removed, by making the product

$$\Delta t_{FWHM}\Delta\nu_{FWHM} = K \tag{1.16}$$

where K is a dimensionless constant dependent on the temporal pulse shape. Eq. (1.16), while derived using gaussian pulses, it is not restricted to them. One can arrive at a similar equation by using other kind of pulse, like an hyperbolic secant pulse,

$$E(t) = E_0 e^{i\omega_0 t} sech\left(\frac{t}{\tau}\right) \tag{1.17}$$

With the help of residue calculus from Complex Analysis, it can be shown that its Fourier transform is

$$\tilde{E}(\nu) \propto \tau sech\left[\pi^2\tau(\nu - \nu_0)\right] \tag{1.18}$$

As it was done in the case of the gaussian pulse, we can calculate Δt_{FWHM} and $\Delta\nu_{FWHM}$ and end up with Eq. (1.16), with a different value for the constant K (see table 1).

Any pulse that observes Eq (1.16), regardless of pulse shape (and for a suitable constant K), is said to be transform-limited (TL), in other words, it is the shortest pulse attainable for a given spectrum, i.e., when its spectral phase is constant. When the spectral phase is not constant, then the pulse is no longer transform-limited (thus the pulse duration is longer) and so, the strict equality in Eq. (1.16) becomes a strict inequality. The general situation can be described by Eq. (1.19)

$$\Delta t_{FWHM} \Delta \nu_{FWHM} \geq K \tag{1.19}$$

Table 1 shows the values of K for different pulse shapes [3], where the expressions for the single-sided exponential and symmetric exponential pulses are given by

$$E(t) = \frac{E_0}{2} e^{-\frac{ln(2)}{2} \frac{t}{\Delta t_{FWHM}}} \quad , t \geq 0 \tag{1.20}$$

$$E(t) = \frac{E_0}{2} e^{-ln(2) \frac{t}{\Delta t_{FWHM}}} \tag{1.21}$$

respectively.

Shape	TBP
Gaussian	0.441
Hyperbolic secant	0.315
Square	0.886
Single-sided exponential	0.110
Symmetric exponential	0.142

Table 1: TBP constant (K) for different types of pulses.

1.3 Ultrafast pulse generation

In general, a laser cavity can support several longitudinal modes [4], separated by a mode spacing $\Delta \nu$,

$$\Delta \nu = \frac{c}{2L} \tag{1.22}$$

where c is the speed of light and L is the length of the laser cavity. Figure 1.4 shows the intensity of oscillation of a single mode (a), the resultant intensity of two modes in phase (b), and that of eight modes with random phase (c) and with zero phase (d). We see that as the number of oscillating modes increases, it is possible to create periodic pulse shapes with short temporal duration if and when there is a fixed relationship between the phases of consecutive longitudinal modes (Figure 1.4d). Such coherent addition of oscillating modes results in an increased peak intensity (as it scales with N^2 instead of N as in the case of an incoherent sum, with N being the number of modes).

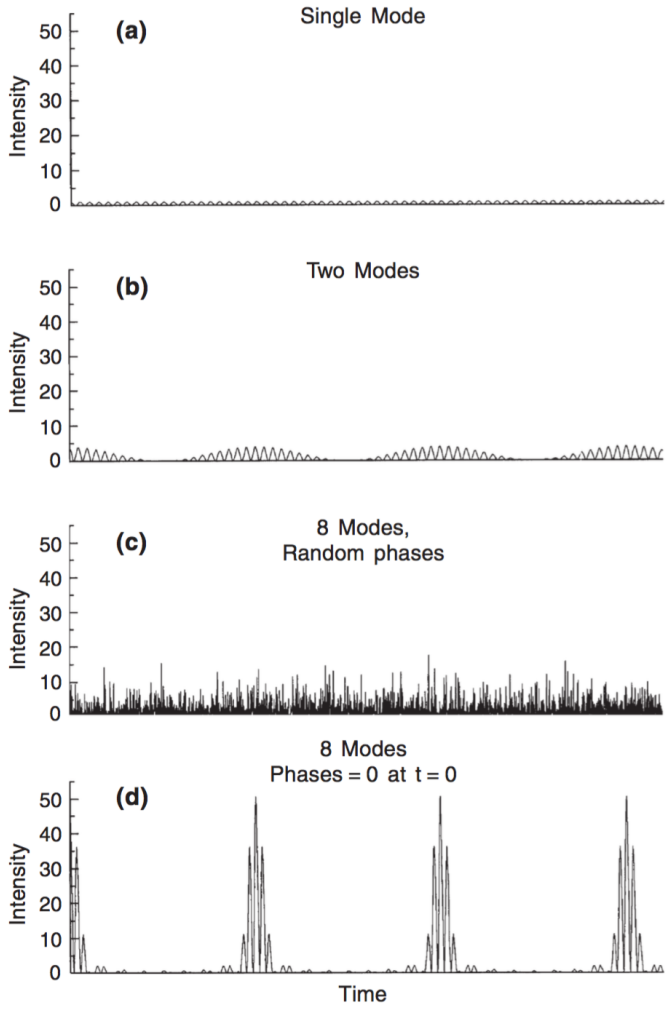

Figure 1.4: Intensity of a laser with a) a single mode b) two modes c) 8 modes with random phases and d) 8 modes with the same phase [5].

Since the pulse duration decreases with increasing number of oscillating modes, the general guideline for the design of ultrafast lasers relies on the choice of an adequate laser medium. The Ti:Sapphire crystal was found to be a suitable material for the development of ultrafast laser systems [6], due to its large emission bandwidth and the capability of supporting Kerr-lens modelocking (KLM; as defined in the following text). The Kerr effect [7, 8] is a third-order nonlinear optical effect that entails an intensity dependent refractive index, $n(I)$, in an optical medium

$$n(I) = n_0 + n_2 I, \tag{1.23}$$

where n_0 is the linear refractive index, I is the pulse intensity and n_2 is the nonlinear refractive index. It is this effect that enables a type of modelocking named Kerr-lens modelocking [9]. The design and description of KLM based Ti:Sapphire lasers are beyond the scope of this work, cf. [10] for a review in this topic.

1.4 Applications

Ultrashort laser pulses are nowadays a very useful tool in a vast variety of areas. In medicine precise contactless surgery procedures have been possible through them [11]. In solid-state physics they can produce high-quality ablation of materials and hence be used for micromachining [12], and they are also able to nanostructure surfaces conferring them specific properties, such as superhydrophobia [13]. They have also allowed for studying the evolution of systems in very short time scales using techniques such as pump-probe configurations [14, 15]. The stabilization of the carrier-envelope phase and its control has permitted to generate optical frequency combs which have revolutionized the field of metrology [16, 17]. Laser fields have been demonstrated to accelerate particles up to relativistic velocities [18]. The processes induced in matter by ultrashort laser pulses create secondary light sources, and nowadays it is possible to generate coherent radiation in the terahertz [19, 20], ultraviolet and extreme ultraviolet (XUV) [21] region, departing from visible and/or infrared laser pulses, the latter giving rise to the field of attoscience. More references on the different application fields can be found in [22].

1.5 Ultrafast pulses and Nonlinear Optics

Short pulse durations imply high peak intensities, where the electric field of the pulse is comparable or even higher than the typical electrostatic field that binds an electron to an atom. In these situations we can expand the electric polarization, P, as a multilinear function of the electric field E,

$$P_i = \sum_j \frac{\epsilon_0}{2} \left(\chi^{(1)}_{ij} E_j + \chi^{(2)}_{ijk} E_j E_k + \chi^{(3)}_{ijkl} E_j E_k E_l + \ldots + c.c \right) \tag{1.24}$$

where

$$P^{(1)}_i = \sum_j \frac{\epsilon_0}{2} \left(\chi^{(1)}_{ij} E_j + c.c \right) \tag{1.25}$$

is the term associated with linear optics, $\chi^{(2)}_{ijk}$ and $\chi^{(3)}_{ijkl}$ are the second and third-order susceptibilities, the subscript triplet (i, j, k) denotes the projection of a tensor quantity along a chosen axis (x, y, z) , and $c.c$ denotes the complex conjugate. The most striking effect of nonlinear terms is that we can express the electric polarization vector as a product of more than one electric field, in contrast with the term associated with linear optics.

A fruitful consequence of this apparently simple multiplication is that we can generate coherent light in newer frequencies, as shown below. Let us ignore, for now, the tensorial nature of the nonlinear phenomena and adopt a scalar approach (i.e., considering only a linear polarization of a pulse), which is enough for our approach (the interested reader may see [23, 24, 25] for a more general description of nonlinear phenomena). For example, let us focus on the following term

$$P = \epsilon_0 \chi^{(2)} E^2 \tag{1.26}$$

Using the Convolution Theorem of the Fourier transform, $\mathcal{F}$, this equation can be expressed as a convolution,

$$E^2(t) = \mathcal{F}^{-1}\left\{\int_{-\infty}^{+\infty} \tilde{E}(\Omega)\tilde{E}(\omega - \Omega)d\Omega\right\} \tag{1.27}$$

where $\mathcal{F}^{-1}$ denotes the inverse Fourier transform. Let us assume that ω, is the central wavelength of $\tilde{E}(\omega) = \mathcal{F}\left[E(t)\right]$. We can see that the convolution will achieve its maximum value if and only if $\tilde{E}(\omega)$ and $\tilde{E}(\omega - \Omega)$ are well overlapped in the frequency domain, i.e, when $(\omega - \Omega) = \Omega$, or equivalently, $\omega = 2\Omega$. Similar reasoning can be applied to other multiplicative terms involving $\chi^{(2)}$, and in fact can also be extended to $\chi^{(3)}$ and higher-order susceptibility tensors ($\chi^{(n)}$) since the multiple convolutions can be computed sequentially.

Another interesting application of nonlinear optics is the spectral broadening of a ultrashort pulse through a third-order nonlinear effect such as the self-phase modulation (SPM). SPM is characterized by an refractive index, $n(I)$, dependent on the pulse intensity, I

$$n(I) = n_0 + n_2 I, \tag{1.28}$$

where n_2 is the nonlinear refractive index. As the pulse intensity $I(t)$ is a time dependent quantity, it modulates the refractive index seen by the pulse which determines the amount of phase acquired by the pulse during propagation, $\phi_{SPM}(t) = \frac{2\pi z}{\lambda_0} n(I)$, where λ_0 is the carrier wavelength and z is the propagation length. The radial instantaneous frequency

is given by

$$\omega(t) = \omega_0 - \frac{d\phi_{SPM}}{dt}. \tag{1.29}$$

The effect of this self-phase modulation translates into a broadening of the pulse spectrum, as new frequencies are generated (see Figure 1.5) during the pulse propagation in the nonlinear medium. Figure 1.5 shows the simulation of SPM for a gaussian pulse with 25 fs of pulse duration, propagation length of 50 cm in fused silica and pulse intensity of 10 GW/cm^2.

Other third-order nonlinear effect such as the self-diffraction (SD) will be discussed in chapter 4 and chapter 6.

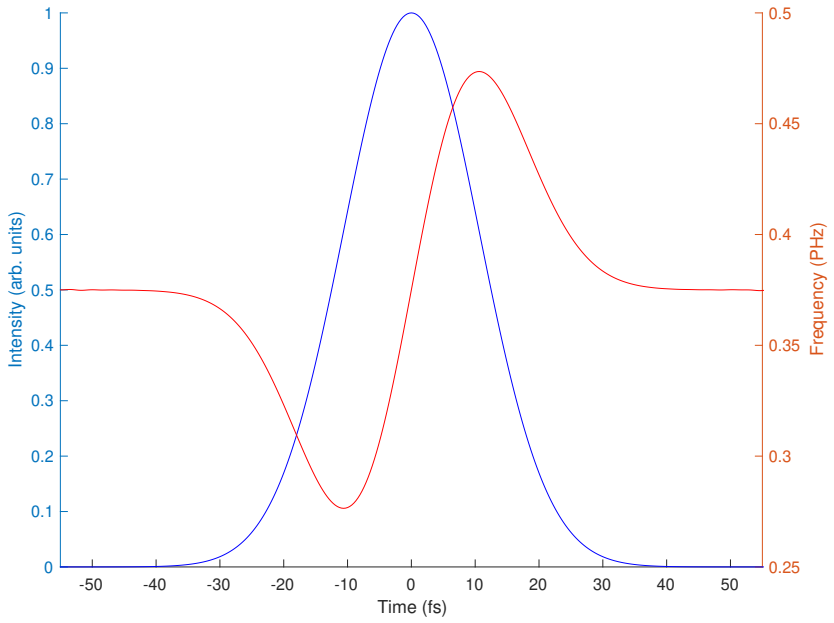

Figure 1.5: Simulation of SPM (without dispersion) with a gaussian pulse. The pulse temporal profile (blue) remains unchanged while the range of frequencies get broadened as evidenced by the variation of the instantaneous frequency $f = \frac{\omega(t)}{2\pi}$ with time (red).

1.6 Phase-matching

While the existence of nonlinear optics allows us to generate coherent radiation in other spectral regions, it is important to evaluate the efficiency of such conversion process.

Taking as an example the second-harmonic generation (SHG),

$$\nabla^2\vec{E} - \frac{n^2}{c^2}\frac{\partial^2\vec{E}}{\partial t^2} = \frac{\partial^2\vec{P}_{NL}}{\partial t^2}, \tag{1.30}$$

it can be shown [25] that the output power of the SHG, assuming monochromatic plane waves, can be given by

$$Power_{SHG} \propto \frac{sin^2\left(\frac{\Delta k}{2}L\right)}{\left(\frac{\Delta k}{2}L\right)^2} \times L^2, \tag{1.31}$$

where Δk is the phase-mismatch and L is the thickness of the SHG crystal. Eq. 1.31 tell us that to maximize the conversion efficiency we must have $\Delta k = 0$. For a medium with one single refractive index, $\Delta k = 0$ is impossible to obtain since the refractive index is a monotonically increasing function of frequency. One way of achieving phase-matching is to use birefringent materials, more specifically uniaxial crystals (e.g., BBO, KDP), where the refractive index, $n(\theta)$, can be varied through the angle between propagation and the crystal optical axis, θ. For an uniaxial crystal, $n(\theta)$ is given by

$$\frac{1}{n^2(\theta)} = \frac{cos^2(\theta)}{n_o^2} + \frac{sin^2(\theta)}{n_e^2}, \tag{1.32}$$

where n_o and n_e are the refractive indices along the ordinary and extraordinary axes of the crystal. In this case, with the ability to tune the refractive index (as a function of θ), the phase-mismatch, for the case of SHG becomes $\Delta k = k(\theta, 2\omega) - 2k(\omega)$, where Δk can be minimized or set to zero for a given value of θ. Unlike the previous type of phase-matching, it is also possible to achieve phase-matching through the control of the crystal temperature, i.e., noncritical phase-matching (also known as temperature phase-matching) [26].

1.7 Dispersion

Ultrashort pulses generally get distorted as they travel to the places where they are needed/put to use far from the laser source. Should these pulses travel through air, glass or any other transparent media, they will suffer the effects of dispersion, i.e, a different refractive index for every frequency/wavelength leading to pulse distortion. It should be noted that the output of a laser is not forcibly compressed temporally. To describe these effects, let us consider the electric field in the frequency domain, $\tilde{E}$,

$$\tilde{E}(\omega) = \left|\tilde{E}(\omega)\right| e^{-i\varphi(\omega)}, \tag{1.33}$$

where φ is defined as the spectral phase. For pulses with the spectrum centered[1] around ω_0, we can expand φ as a Taylor expansion,

$$\varphi(\omega) = \varphi(\omega_0) + \frac{d\varphi}{d\omega}(\omega - \omega_0) + \frac{1}{2!}\frac{d^2\varphi}{d\omega^2}(\omega - \omega_0)^2 + \frac{1}{3!}\frac{d^3\varphi}{d\omega^3}(\omega - \omega_0)^3 \ldots \tag{1.34}$$

When $\varphi(\omega)$ is constant, the pulse is said to be transform-limited (TL), i.e., it attains the shortest pulse duration for a given pulse spectrum. The first term of $\varphi(\omega)$ is the Carrier-Envelope Phase (CEP), $\varphi(\omega_0)$, also known as Carrier-Envelope Offset (CEO). Conceptually, it is a constant phase offset[2] that does not influence the temporal profile of an ultrashort pulse. However, for few-cycle pulses, it is a crucial parameter (along with its stabilization) that affects physical phenomena driven by ultrashort pulses, like high-harmonic generation (HHG). The stabilization and determination of the CEP is beyond the scope of this thesis, and the interested reader should refer to [27, 28, 29]. The next term in Eq. 1.34 is due to the group-delay, t_g, given by

$$t_g = \frac{d\varphi}{d\omega}, \tag{1.35}$$

and it represents the amount of time taken for a wave packet at a given frequency/wavelength to traverse an optical element. If $t_g(\omega)$ is constant for all ω, then the ultrashort pulse undergoes a bulk shift in time, otherwise, it will suffer distortions due to higher-order dispersion. If we consider higher-order terms, we see that they imply a non-constant group-delay, i.e, a frequency dependent group-delay which naturally leads to the distortion of the original pulse. Higher-order terms of this expansion in Eq 1.34, i.e, the nonlinear terms (notice that they are associated to $n \geq 2$ powers of $(\omega - \omega_0)$) are important for ultrafast optics because they are responsible for temporal pulse broadening and distortion. Figure 1.6 shows a initial gaussian pulse (capable of supporting a TL 5 fs duration) affected by a group-delay (GD) of 20 fs, a group-delay dispersion (GDD) of 20 fs^2 and a third-order dispersion of 80 fs^3. The group-delay translates into a shift of the pulse in time, the GDD broadens the pulse in time and the TOD gives rise to pre/post-pulses depending on the negative/positive sign of the TOD.

[1] Here we talk about the nominal central frequency (or its corresponding wavelength, e.g, 800 nm. It is also possible to use another convention, i.e, the weighted average frequency of a broadband spectrum.

[2] CEP is constant when the CEP is stabilized (cf. references in the text)

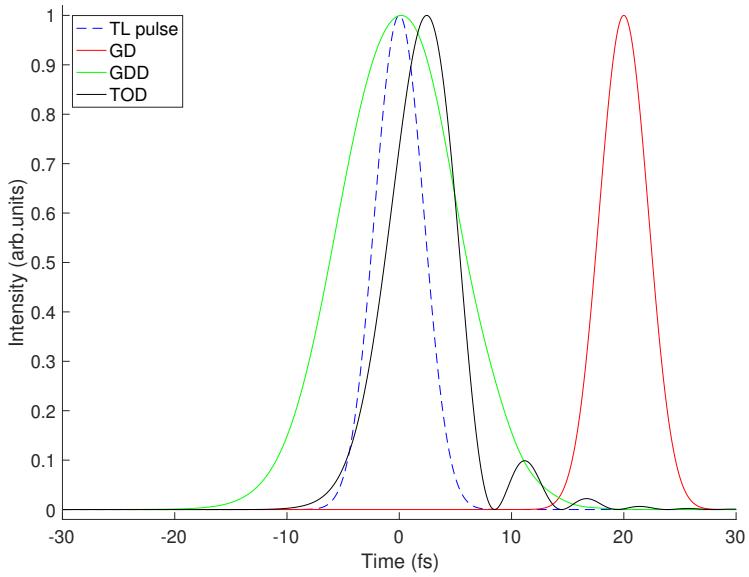

Figure 1.6: A gaussian pulse capable of supporting a TL duration of 5 fs affected by group-delay (20 fs), group-delay dispersion (20 fs^2) and third-order dispersion (80 fs^3).

1.8 Dispersion compensation

Dispersion arises from differences in the optical path length (OPL) between different wavelengths, and as such, can be compensated for (up to a certain order) by judiciously manipulating the OPL. Some strategies for dispersion compensation rely on geometrical OPL manipulation, e.g., using reflective diffraction gratings or a pair of prisms, while other strategy relies on both the path length manipulation as well as in the modulation of the refractive index of the medium crossed by the pulse or the phase introduced by engineered optical elements, e.g., dispersion-compensation mirrors (DCMs). Pulse compression using diffraction gratings [30] and prisms pairs [31] are two main methods to generate (variable) negative dispersion, though they exhibit an inherent high cubic (and higher) order dispersion, along with their respective disadvantages, e.g., in the case of diffraction gratings, the compressor has high losses [32], as only the first diffraction order is used. In the case of the prism pair, it is usually necessary to have a long prism separation [33] in order to achieve the desired compensation. The third-order dispersion of each scheme (prism pair and grating) can be compensated by combining both setups [34], albeit suffering from the same aforementioned disadvantages. Besides diffraction gratings and prisms, a new way for dispersion compensation was invented [35]. This new strategy involves the creation of special mirrors, i.e., dispersion-compensation mirrors (DCMs) comprised of several unevenly spaced dielectric layers, each with alternating

refractive indices, resulting in a custom design with a target (negative) group-delay dispersion and a high reflectivity. Figure 1.7 illustrates the working concept of DCMs, i.e., longer wavelengths travel a longer distance (penetration depth) inside the stack of dielectric layers compared to shorter wavelengths, before being reflected. This effect amounts to an effective negative group-delay.

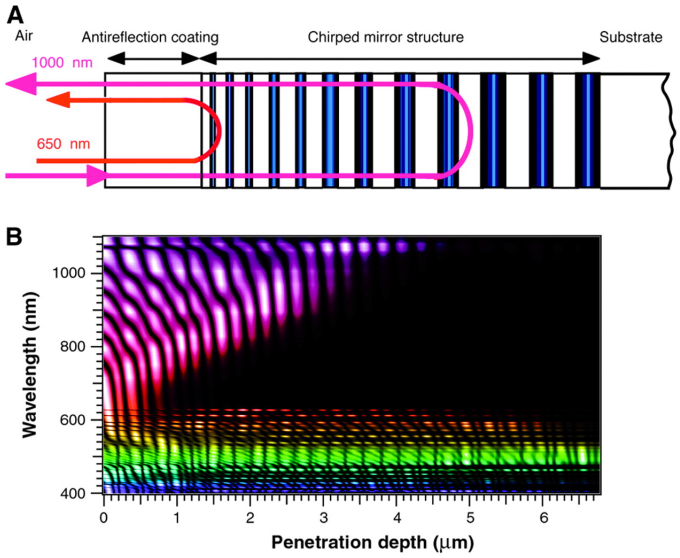

Figure 1.7: A) Structure of a DCM showing layers of different thickness and of alternating refractive indices. B) Penetration depth as a function of wavelength for a DCM (used as part of a laser design) that provides compensation in the 650 to 1050 nm region. The region around 500 nm is designed for transmission of the pump laser. [36]

Due to the nature of design of these mirrors [3], said mirrors contain residual GDD ripples, as exemplified in Figure 1.8.

[3] https://www.laseroptik.de/en/coatings/dispersive-coatings/chirped-mirrors-and-matched-pairs

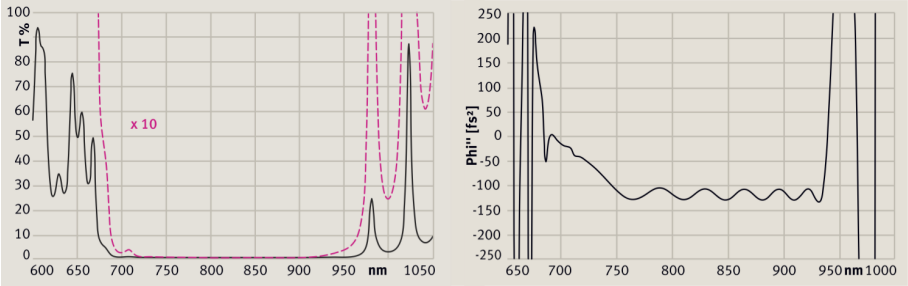

Figure 1.8: DCM designed for the 730-930 nm range, with a nominal GDD of -125 fs². Left) Transmission curve; right) DCM GDD curve, where ripples are visible around the nominal GDD value. (See footnote in previous page).

The DCM mirrors need not be identical to each other, i.e., a pulse compression scheme can be achieved by using mirrors designed at different incident angles (Double-angle DCMs), with different dispersion characteristics in order to provide an overall negative dispersion with less ripples (compared to regular DCMs) over a broad wavelength range [37]. Unlike gratings and prisms, DCMs provide a fixed dispersion, and are normally used in conjunction with a pair of wedges. The typical characteristic reflectance, the GDD of each mirror and overall GDD of one example of double-angle DCMs (PC70[4], Ultrafast Innovations GmBH) is shown in Figure 1.9.

The research and development of DCMs is a very active field. Given their importance in the generation and compression of ultrashort pulses, special focus is given to methods that allow compensation of pulses with an over-octave spectrum [38, 39, 40, 41].

1.9 Chirped pulse amplification (CPA)

Dispersion plays a key role in the amplification of ultrashort pulses. The technique which is known as chirped-pulse amplification (CPA) [42] relies on the temporal stretching (e.g., by a factor of 100000) the input pulse using either a grating stretcher or a piece of bulk glass, and thus, lowering its peak power. This stretched pulse then travels through a laser crystal where it is amplified. The emerging pulse is then recompressed, using a pulse compressor (e.g., diffraction grating pair, or prism pair), reaching a shorter duration and a higher peak power. The CPA has a widespread use in Ti:sapphire laser amplifiers.

[4] http://ultrafast-innovations.com/index.php/database/article/160-pc70

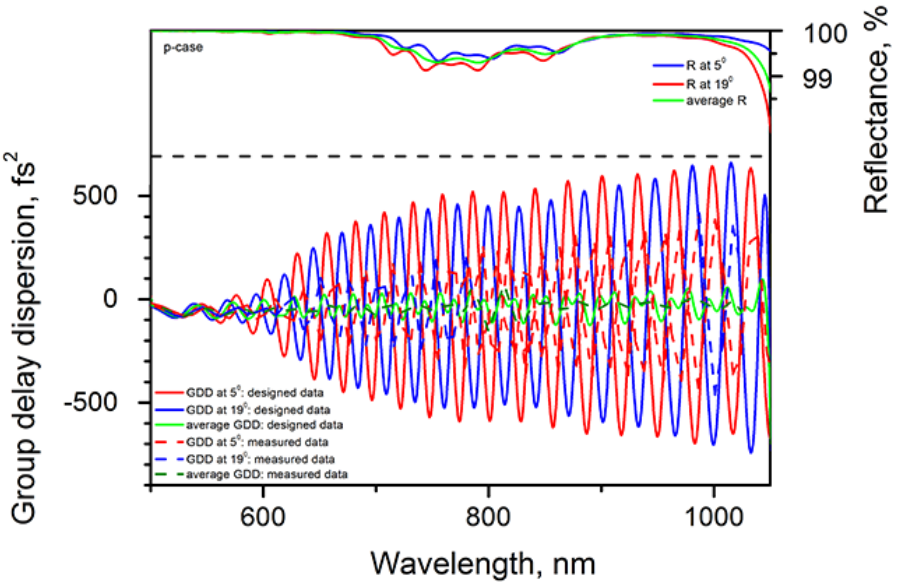

Figure 1.9: Ultrafast Innovations PC70 (see footnote in previous page).

2 Pulse Measurement

"Wir müssen wissen - wir werden wissen!" (We must know - we will know!)

David Hilbert

This chapter contains a brief review of pulse characterization methods developed prior to d-scan, where some of them only provide estimates of pulse duration while others are able to provide the spectrum and the spectral phase of a pulse from which the complete pulse profile and duration can be derived. Nonlinear optics has been and still is a boon for ultrafast optics for it not only provides the means to generate short pulses but also the means to measure them. So far, most popular methods for the measurement of the temporal profile of the electric field rely on media with a certain optical nonlinearity, be it of second order, $\chi^{(2)}$, or third order, $\chi^{(3)}$. We start by describing techniques based on autocorrelation and then move on to techniques that are able to characterize the full electric field (up to a constant phase), such as frequency-resolved optical gating (FROG) and spectral phase interferometry for direct electric field reconstruction (SPIDER). Some techniques capable of doing spatio-temporal and spatio-spectral characterization will also be described.

2.1 Autocorrelation

Autocorrelation techniques were the first methods employed to estimate pulse duration [43, 44], and so these techniques saw widespread use in the following decades. It is important to point out that not all autocorrelation methods are able to provide the pulse duration of a pulse, i.e., unlike autocorrelation techniques based on the use of nonlinear effects, such as the intensity and interferometric autocorrelators, linear autocorrelators don't provide extra information beyond the pulse spectrum, as it will be shown.

2.1.1 Field autocorrelation

A Michelson interferometer is used to create two identical replicas of an incident pulse separated in time by an amount $\tau = \frac{2L}{c}$, where L is the path length difference between the interferometer arms and c is the speed of light (cf. Figure 2.1). The intensity of the total field is measured at the exit of the interferometer using, e.g., a photodiode.

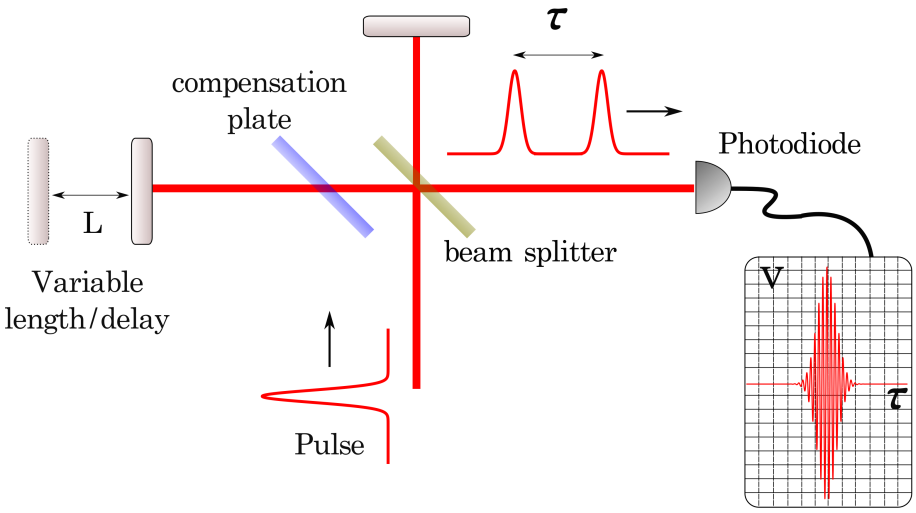

Figure 2.1: Field autocorrelation set-up (collinear arrangement).

The signal measured by the (slow) photodiode is proportional to,

$$I = \int_{-\infty}^{+\infty} |E(t) + E(t-\tau)|^2 \, dt. \tag{2.1}$$

This equation can be further expanded into

$$I(\tau) = \int_{-\infty}^{+\infty} |E(t)|^2 \, dt + \int_{-\infty}^{+\infty} |E(t-\tau)|^2 \, dt + 2Re\left\{\Gamma^{(2)}(\tau)\right\}, \tag{2.2}$$

where the field autocorrelation, $\Gamma^{(2)}(\tau)$, is given by

$$\Gamma^{(2)}(\tau) = \int_{-\infty}^{+\infty} E(t)E^*(t-\tau) \, dt. \tag{2.3}$$

The Wiener–Khinchin theorem tells us that $\mathcal{F}\left\{\Gamma^{(2)}\right\}$ is the spectrum of the pulse, or in other words,

$$\mathcal{F}\left\{\Gamma^{(2)}(\tau)\right\} = \left|\tilde{E}(\nu)\right|^2, \tag{2.4}$$

so we see that the field autocorrelation does not give us any additional information besides the spectrum, i.e., no information on the pulse phase.

Knowing that the linear detection implemented via the Michelson interferometer does not yield any new information about our pulse [45], we now turn to the autocorrelation techniques which use nonlinear effects such as SHG.

2.1.2 Second-order intensity autocorrelation

The intensity autocorrelation is based on the non-collinear interaction of two temporally separated replicas of the pulse in a SHG crystal, generating an upconverted signal that is recorded by a photodetector, such as a photodiode or photomultiplier tube, as depicted in Figure 2.2.

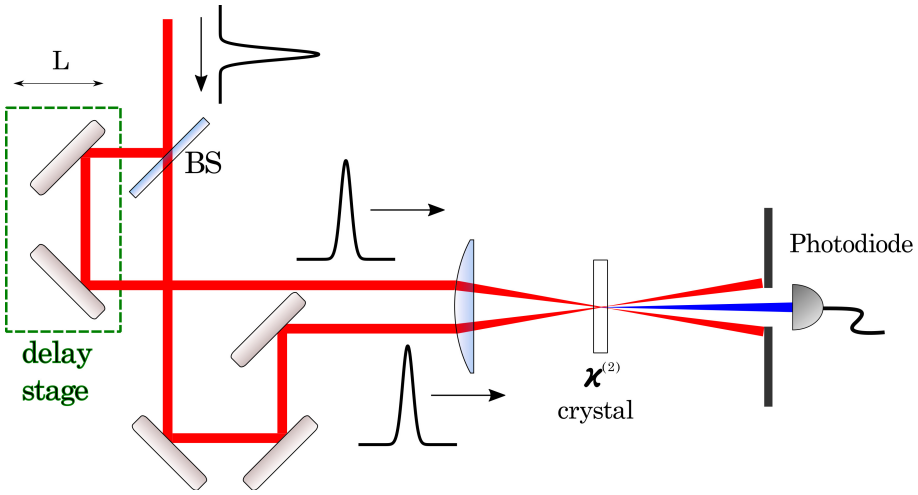

Figure 2.2: Intensity autocorrelation scheme.

In this setup, two pulse replicas are produced by splitting the initial beam with a beam splitter, but unlike the case of field autocorrelation, the resulting replicas are not collinear. Like in the Michelson interferometer, one of the replicas can have a variable optical path, which can change by moving a delay stage. When both beams are focused in a SHG crystal, they will generate a signal $A(\tau)$,

$$A(\tau) = \int_{-\infty}^{+\infty} I(t)I(t-\tau)dt, \tag{2.5}$$

where $I(t) = |E(t)|^2$ is the intensity of the pulse. The intensity autocorrelation, $A(\tau)$, is a quantity that describes how well $I(t)$ overlaps with a shifted copy of itself. With

knowledge of $A(\tau)$, and assuming a certain pulse shape (e.g., gaussian, hyperbolic secant, square, etc.) for $I(t)$ (a common, if not necessary, practice), it is possible to relate the FWHM of A, Δt_A, with the pulse own FWHM, Δt_{FWHM}. For a square pulse, $\Delta t_A = 1 \times \Delta t_{FWHM}$, and for a gaussian pulse, $\Delta t_A = 1.41 \times \Delta t_{FWHM}$. Other pulse shapes have different constant factors [45].

In Figure 2.3, a square shape pulse and a gaussian pulse are shown along with their respective intensity autocorrelation.

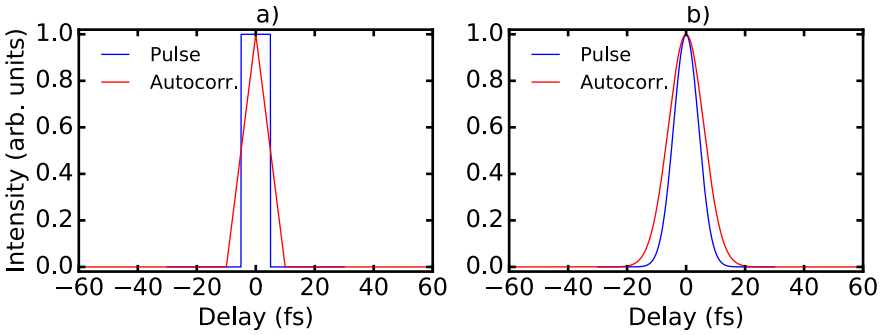

Figure 2.3: Intensity autocorrelation of a) a square pulse and b) a gaussian pulse, with the same FWHM duration of 10 fs.

2.1.3 Second-order interferometric autocorrelation

Interferometric autocorrelation [5, 45], also known as fringe-resolved autocorrelation (FRAC), is a collinear nonlinear autocorrelation. The basic setup is given in Figure 2.4. The pulse is split in two replicas, one of which is delayed in time by an amount τ. Both beams are then focused into a type-I SHG crystal, which generates an upconverted signal, while the fundamental beam is blocked by a filter and/or a polarizer.

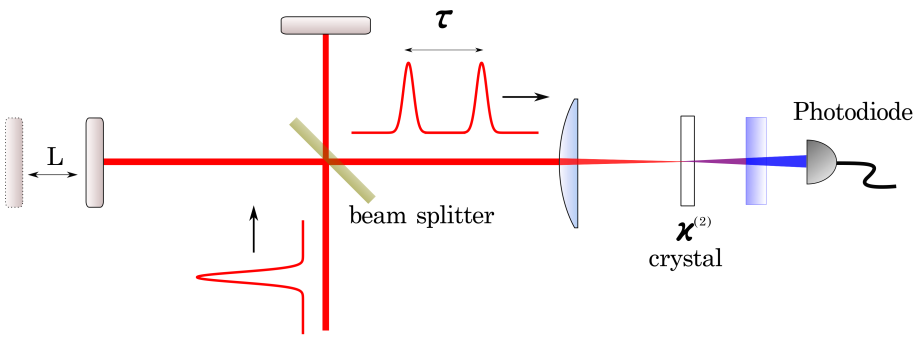

Figure 2.4: Interferometric autocorrelation scheme.

The signal detected by the photodiode is given by

$$I_{FRAC}(\tau) = \int_{-\infty}^{+\infty} \left| [E(t) + E(t-\tau)]^2 \right|^2 dt. \tag{2.6}$$

Figure 2.5 represents a simulation of an interferometric autocorrelation using a 10-fs gaussian pulse centered at 800 nm.

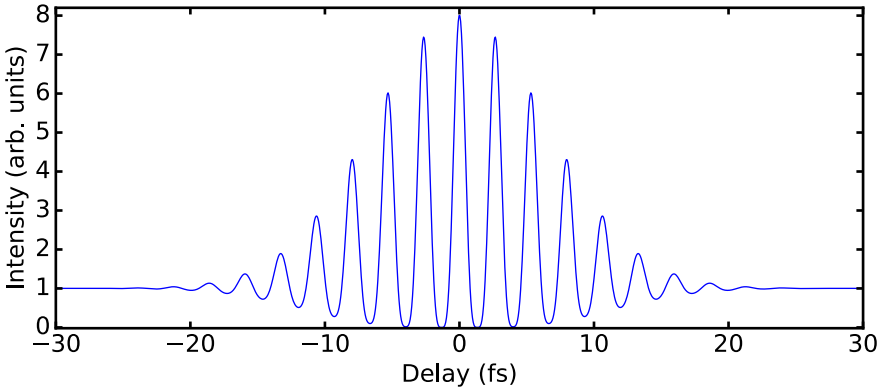

Figure 2.5: Interferometric autocorrelation of a TL, 10 fs gaussian pulse.

An ideal interferometric autocorrelation has a ratio of 8:1 from peak to baseline [45], as it can be shown that $I_{FRAC}(\tau = 0) = 16 \int_{-\infty}^{+\infty} E^4(t)dt$, and $I_{FRAC}(\tau \to \infty) = 2 \int E^4(t)dt$.

It is also worth pointing out that it has been shown [46] that both intensity and interferometric autocorrelation methods have ambiguities, in the sense that different pulses can have similar autocorrelations, showing that autocorrelation methods are inadequate for the determination of the pulse shape.

2.2 FROG

The frequency-resolved optical gating (FROG) [47] method can be viewed as a spectrally resolved nonlinear autocorrelation, i.e., keeping the same setup as in the intensity autocorrelation but replacing the photodiode with a spectrometer. The nonlinear spectrum is then recorded as function of the delay τ. The basic setup is given in Figure 2.6.

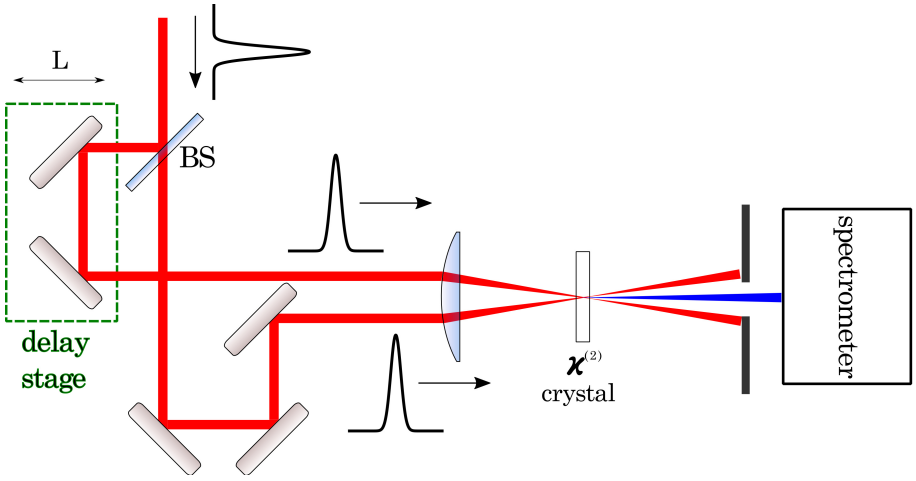

Figure 2.6: SHG FROG setup.

In FROG, the quantity of interest is the overlap, for a given delay τ, between an unknown pulse, $E(t)$, and a gate pulse, $G(t)$, which is derived from the unknown pulse itself. In the case of SHG FROG, $G(t) = E(t)$ (which is not trivial to obtain for a broadband few-cycle pulse). By varying the time delay between the pulse and the gate and measuring the resulting nonlinear spectrum, we are able to obtain a FROG trace, $I_{FROG}(\omega, \tau)$, given by,

$$I_{FROG}(\omega, \tau) = \left| \int_{-\infty}^{+\infty} E_{sig}(t, \tau) e^{-i\omega t} dt \right|^2 , \tag{2.7}$$

where $E_{sig}(t, \tau) = E(t) \times E(t - \tau)$. Other types of FROG based on third-order nonlinearities [48] are mentioned in Table 2, but will not be described here.

Nonlinearity	$E_{sig}(t, \tau)$	Description
$\chi^{(2)}$	$E(t)E(t-\tau)$	Second-harmonic generation (SHG)
$\chi^{(3)}$	$E^2(t)E^*(t-\tau)$	Self-diffraction (SD)
$\chi^{(3)}$	$E^2(t)E(t-\tau)$	Third-harmonic generation (THG)
$\chi^{(3)}$	$E(t)\left\|E(t-\tau)\right\|^2$	Polarization-gated (PG)

Table 2: Types of FROG

Figure 2.7 shows four simulated SHG-FROG traces, using a gaussian pulse centered at 800 nm, capable of supporting a TL 10 fs pulse, with 80 fs^2 of GDD, 400 fs^3 of TOD and 10000 fs^4 of FOD, respectively.

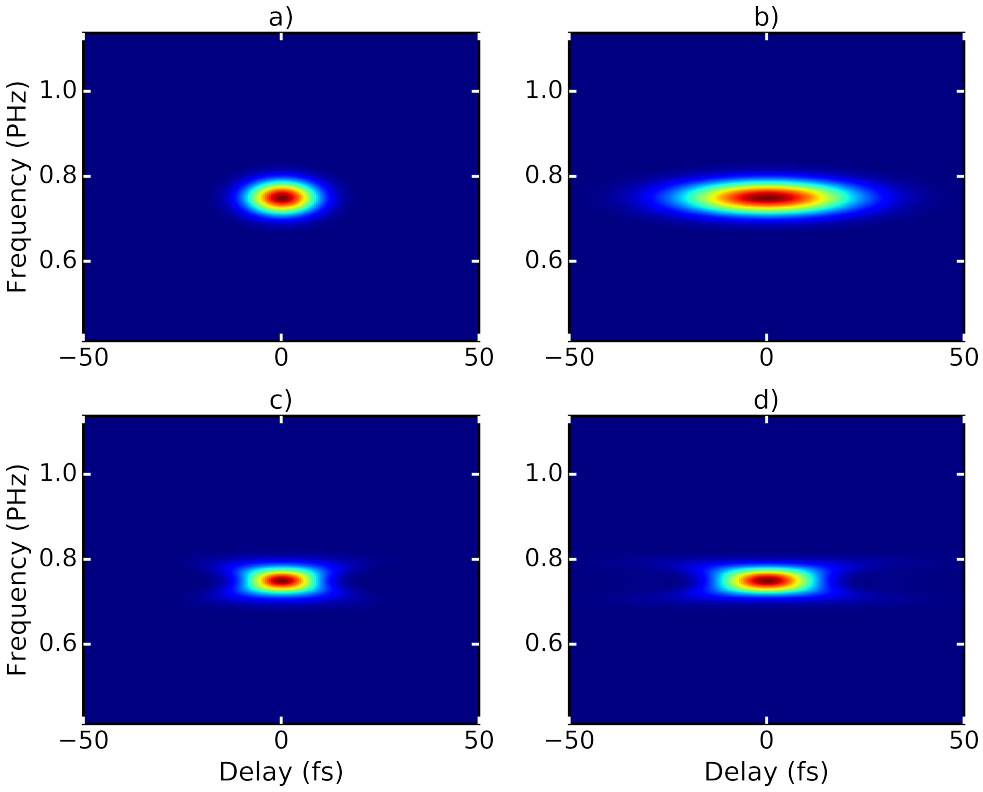

Figure 2.7: SHG FROG traces for a) TL pulse b) pulse with linear chirp c) pulse with TOD and d) pulse with FOD; see text for details.

It should be noted that in the SHG variant of FROG, the traces are symmetric with respect to the delay variable τ. This can understood by the fact that SHG FROG is given by the squared absolute value of an autocorrelation, and autocorrelations observe the following property, $A(\tau) = A^*(-\tau)$. Hence SHG FROG suffers from a time direction ambiguity.

The amplitude and spectral phase of the input field can be retrieved by comparing the measured trace with a trace simulated by Eq. 2.7. There are several algorithms for the retrieval of FROG traces, like the basic algorithm [49, 48], the generalized projections algorithm (GP) [50], and the principal component generalized projections algorithm (PCGP) [51, 52]. The basic algorithm generates a new FROG signal in the frequency domain $\tilde{E}'_{sig}(\omega,\tau)$ from the measured FROG trace $I_{FROG}(\omega,\tau)$

$$\tilde{E}'_{sig}(\omega,\tau) = \frac{\tilde{E}_{sig}(\omega,\tau)}{\left|\tilde{E}_{sig}(\omega,\tau)\right|}\sqrt{I_{FROG}(\omega,\tau)}, \tag{2.8}$$

where $\tilde{E}_{sig}(\omega,\tau)$ is the Fourier transform of $E_{sig}(t,\tau)$ (from table 2, e.g., $E(t)\left|E(t-\tau)\right|^2$ in the case of PG-FROG) that is calculated using a initial guess for the electric field $E^{(k)}(t)$, where k denotes the iteration number of the algorithm. The next iteration $E^{(k+1)}(t)$ is then obtained by integration

$$E^{(k+1)}(t) = \int_{-\infty}^{+\infty} E_{sig}^{(k)}(t,\tau)d\tau,$$

where $E_{sig}^{(k)}(t,\tau) = \mathcal{F}^{-1}\left[\tilde{E}'_{sig}(\omega,\tau)\right]$. The GP algorithm works by requiring that the desired solution obeys two constraints, namely, the mathematical constraint, e.g., $E_{sig} = E(t)E(t-\tau)$ in the case of SHG-FROG, and the data constraint set by Eq. 2.7. The set of solutions for one constraint may not satisfy the other constraint, thus a series of projections (as defined in [50]) are taken until reaching a solution that satisfies both constraints. The PCGP algorithm is briefly described in section 3.6.1.

2.3 SPIDER

SPIDER stands for spectral phase interferometry for direct electric field reconstruction [53, 54]. It is a special case of Fourier transform spectral interferometry (FTSI) (cf., [55]), but unlike in the case of FTSI, the reference pulse is derived from the unknown pulse itself, making it a self-referenced technique. Figure 2.8 shows the SPIDER setup schematic. Part of the pulse goes to a Michelson interferometer to generate two pulse replicas separated by a time delay, τ. Another part of the pulse goes through a pulse stretcher (e.g. a SF10 glass block). The two replicas and the stretched pulse are recombined and focused into a type-II SHG crystal which performs sum-frequency generation (SFG), resulting in two temporally delayed and frequency-shifted pulses which produce the SPIDER interferogram recorded by a spectrometer.

The SPIDER interferogram can be written as [55],

$$S(\omega) = D^{(dc)}(\omega) + e^{-i\omega\tau}D^{(-ac)}(\omega) + e^{i\omega\tau}D^{(+ac)}(\omega), \tag{2.9}$$

where

$$D^{(dc)}(\omega) = \left|\tilde{E}(\omega-\Omega)\right|^2 + \left|\tilde{E}(\omega)\right|^2 \tag{2.10}$$

is the dc part, which does not contain any information, τ is the temporal delay between replicas, and

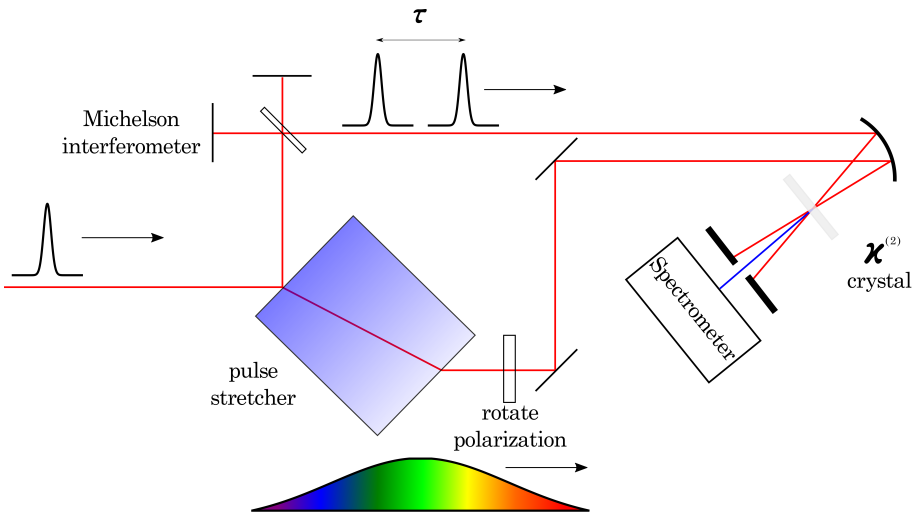

Figure 2.8: SPIDER setup.

$$D^{(\pm ac)}(\omega) = \left|\tilde{E}(\omega-\Omega)\tilde{E}(\omega)\right| exp\left\{\mp i\left[\varphi(\omega)-\varphi(\omega-\Omega)\right]\right\} \tag{2.11}$$

contains the ac terms. The spectral shear, Ω, arises from the sum-frequency generation between the stretched pulse and the two replicas. This can be understood by noting that the instantaneous frequency of the stretched pulse is linearly dependent on time. Hence, in the SFG crystal, each replica will mix with a different frequency from the stretched pulse. The spectral shear, Ω, is given by [55],

$$\Omega = -\frac{\tau}{\varphi''}, \tag{2.12}$$

where φ'' is the GDD imparted by the stretcher block.

A simulated SPIDER interferogram is shown in Figure 2.9, using a a gaussian pulse centered at 800 nm, capable of supporting a TL duration of 10 fs, with an added TOD of 200 fs^3, a spectral shear of 10^{13} fs^{-1} and a delay of 200 fs. To extract the spectral phase of the pulse, it is necessary to Fourier transform the interferogram to the time domain. We can see three main contributions: the dc part at the center, and the ac terms at $-\tau$ and τ (cf. Figure 2.9). Since both ac terms contain the same information on the spectral phase, we only need to choose one of them. We do so by multiplying the interferogram (in the time domain) by a supergaussian filter centered on one of the ac terms, e.g. the contribution located at $t = \tau$.

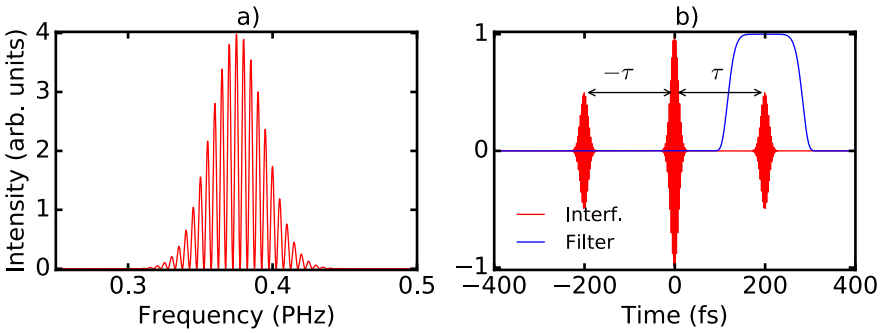

Figure 2.9: Simulated SPIDER interferogram (using a gaussian pulse) in the a) spectral domain and b) time domain.

The respective selection in the time domain is Fourier transformed again to the frequency domain, producing a new interferogram (not to be confused with the SPIDER interferogram), with a phase given by,

$$\varphi(\omega) - \varphi(\omega - \Omega) - \omega\tau, \tag{2.13}$$

where $\omega\tau$ is the contribution due to the time delay and $\varphi(\omega) - \varphi(\omega - \Omega)$ can be interpreted as a finite difference proportional to the group-delay (cf. Figure 2.10; using the same simulation parameters as in Figure 2.9), i.e.,

$$\theta(\omega) = \varphi(\omega) - \varphi(\omega - \Omega) \approx \frac{d\varphi}{d\omega}\Omega, \tag{2.14}$$

from which the spectral phase can be retrieved by integration,

$$\varphi(\omega) = \frac{1}{\Omega}\int \theta(\omega)d\omega. \tag{2.15}$$

It is important to note that, before retrieving the phase, we must remove the dependence on τ, a task that can be accomplished by making an additional measurement of an interferogram with no spectral shearing [56] and subtract its phase from Eq. 2.13. Another alternative for phase retrieval is to follow a concatenation process of $\theta(\omega)$ [55].

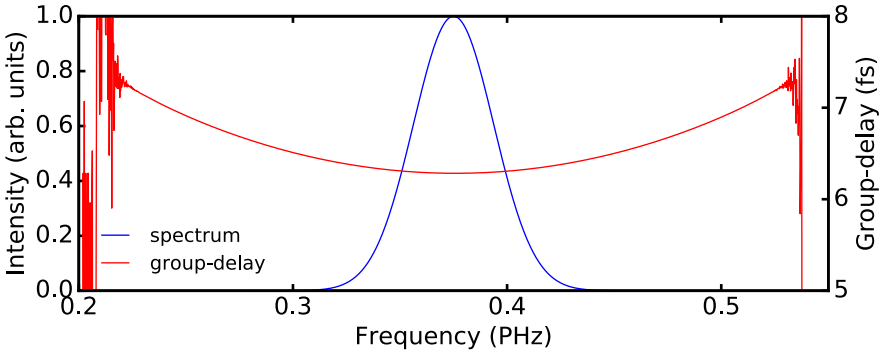

Figure 2.10: Spectrum and retrieved group-delay of the gaussian pulse with TOD mentioned in the text.

2.4 MIIPS

Multiphoton Intrapulse Interference Phase Scan (MIIPS) is a method to measure and compress a pulse based on the use of a pulse shaper, which includes a liquid-crystal spatial light modulator (LC-SLM) to change the spectral phase of the pulse to be measured [57].

The MIIPS schematic is shown in Figure 2.11. A pulse to be measured traverses a pulse shaper which imparts an additional spectral phase term. Subsequently the beam goes through a SHG crystal and the nonlinear signal is measured with a spectrometer.

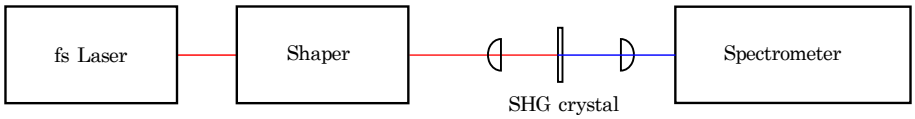

Figure 2.11: Basic scheme for a MIIPS setup.

The total spectral phase, $\Phi(\omega, \delta)$, is given by,

$$\Phi(\omega, \delta) = \varphi(\omega) + \varphi_{shaper}(\omega, \delta), \tag{2.16}$$

where $\varphi(\omega)$ is the unknown phase of the pulse and $\varphi_{shaper}(\omega, \delta)$ is the extra term introduced by the shaper. The SHG signal is given as a convolution which can be represented by [58, 57]

$$I(\omega, \delta) = \left| \int_{-\infty}^{+\infty} |E(\omega + \Omega)|\, |E(\omega - \Omega)|\, e^{i\{\Phi(\omega+\Omega,\delta)+\Phi(\omega-\Omega,\delta)\}} d\Omega \right|^2 . \tag{2.17}$$

The expansion of the expression inside the complex exponential only contains even powers of Ω,

$$\Phi(\omega+\Omega,\delta)+\Phi(\omega-\Omega,\delta)=2\Phi(\omega,\delta)+\Phi''(\omega,\delta)\Omega^2+\ldots \tag{2.18}$$

The term $2\Phi(\omega,\delta)$ does not depend on Ω, and so it can be taken out of the integral, i.e., the MIIPS trace is not dependent on the absolute phase. From literature [58, 57], a common choice for φ_{shaper} is a sinusoidal function,

$$\varphi_{shaper}(\omega,\delta)=\alpha\times cos(\gamma\omega-\delta), \tag{2.19}$$

where the parameters α and γ, are fixed parameters. δ is a parameter that can be swept over a continuous interval, e.g., from 0 to 4π. A typical MIIPS trace is depicted in Figure 2.12, which was obtained from a gaussian pulse centered at 800 nm, capable of supporting a TL 10 fs pulse, with additional TOD of 500 fs^3, and $\alpha=4$ (rad), $\gamma=10$ fs.

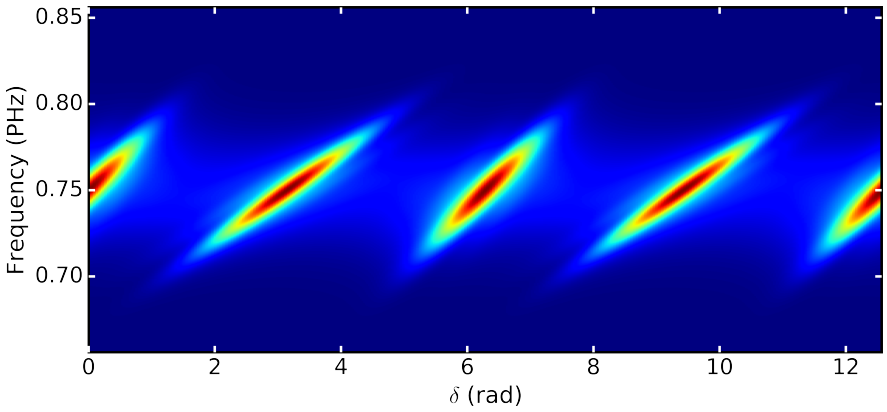

Figure 2.12: Simulated MIIPS trace. See text for details.

For each (radial) frequency ω, there is a value of δ that maximizes the intensity of the MIIPS trace. The maximum of the trace is obtained when,

$$\Phi(\omega+\Omega,\delta)+\Phi(\omega-\Omega,\delta)=0, \tag{2.20}$$

in other words, and ignoring the term $2\Phi(\omega,\delta)$, it means that the maximum condition can be reduced to,

$$\Phi''(\omega,\delta_{max})=\frac{d^2\Phi}{d\omega^2}=0. \tag{2.21}$$

Eq. 2.21 implies that,

$$\Phi''(\omega, \delta_{max}) = \varphi''(\omega) + \varphi''_{shaper}(\omega, \delta_{max}) = 0, \tag{2.22}$$

from which we can retrieve the GDD of the unknown pulse

$$\varphi''(\omega) = -\varphi''_{shaper}(\omega) = -\alpha\gamma^2 cos(\gamma\omega - \delta_{max}). \tag{2.23}$$

To obtain the spectral phase, φ'' is numerically integrated twice. This results in a phase $\varphi^1(\omega)$, that describes most of the distortion of the initial pulse, with respect to a TL MIIPS trace [58]. As higher-order terms in the Taylor expansion (of Eq. 2.18) were not taken into account, this results in an additional source of error, and successive iterations are required to minimize it [58]. By feeding back $\varphi^{(1)}(\omega)$ to the shaper, a new MIIPS trace is generated, from which a new phase can be obtained $\varphi^{(2)}(\omega)$ with the aforementioned procedure, and so on. After several iterations of the MIIPS procedure, the unknown spectral phase can be given by the sum of the phases obtained through successive iterations,

$$\varphi(\omega) - \left[\varphi^{(1)}(\omega) + \varphi^{(2)}(\omega) + \varphi^{(3)}(\omega) + \varphi^{(4)}(\omega) + \ldots\right] \approx 0. \tag{2.24}$$

As a consequence of this procedure, the final pulse is compressed to a nearly transform-limited duration.

2.5 Other methods

This review of pulse measurement techniques is far from exhaustive. There are other methods deserving of mention such as the two-dimensional shearing interferometry (2DSI) [59], the self-referenced spectral interferometry (SRSI) [60] as well as other FROG [61] and SPIDER [62] variations. For a comprehensive review on pulse measurement, the reader is referred to [63].

2.6 Spatiotemporal characterization

Ultrashort pulses, namely, pulses with a broad spectrum and a convenient spectral phase distribution, can experience a spatially dependent transformation, when the beam is manipulated with optical refractive or diffractive elements [64, 65]. The knowledge of this space-time coupling, i.e., the spatial dependence of the temporal properties of a pulse is important in the optimization of the beam properties as mentioned in [66].

An extensive review of the techniques for the spatiotemporal characterization of ultrashort laser pulses is out of the scope of this work. Some of the techniques are the "spatial encoded arrangement for temporal analysis by dispersing a pair of light E-fields" (SEA-TADPOLE) [67], the "spatially and temporally resolved intensity and phase evaluation device: full information from a single hologram" (STRIPED FISH) [68, 69], the Shackled-FROG [70, 71], and the spatially encoded arrangement for SPIDER (SEA-F-SPIDER) [72, 73]. In the following we describe a technique that will be used in chapter 5.3 for the characterization of a supercontinuum process in thin solid media.

2.6.1 Spectral interferometry and STARFISH

Another spatiotemporal pulse characterization technique is the "spatiotemporal amplitude-and-phase reconstruction by Fourier-transform of interference spectra of highly-complex-beams" (STARFISH) [74], which will be featured later in this work. Before explaining the STARFISH technique, it is useful to consider the concept of Fourier transform spectral interferometry. Fourier transform spectral interferometry (FTSI; SI for short), of which SPIDER is a self-referenced variant, was shown to be useful in the measurement of the temporal profile of a pulse. As interference is a very general phenomenon which can happen across the time and/or spatial domain, it is enticing to explore such phenomena in a newer direction, i.e., in the spatial or even spatiotemporal characterization of pulses. A common setup to accomplish a spatiotemporal interferogram is the Mach-Zehnder interferometer [75], as depicted in Figure 2.13.

The beam is split into two replicas beams traveling through two distinct interferometer arms, where the length of one of the arms can be varied by a delay stage. Another beamsplitter will then serve as a beam combiner, thus generating the spatiotemporal interferogram, which is then analyzed by a wavefront sensor. The equation for the interferogram, $S(\omega, \vec{\mathbf{r}})$, is given by,

$$S(\omega,\vec{\mathbf{r}}) = S_{test}(\omega,\vec{\mathbf{r}}) + S_{ref}(\omega,\vec{\mathbf{r}}) + 2\sqrt{S_{test}(\omega,\vec{\mathbf{r}})S_{ref}(\omega,\vec{\mathbf{r}})}\, cos\left[\varphi_{test}(\omega,\vec{\mathbf{r}}) - \varphi_{ref}(\omega,\vec{\mathbf{r}}) - \omega\tau\right], \tag{2.25}$$

which is a typical equation for SI, now with an added dependence on the transverse spatial dimensions $\vec{\mathbf{r}} = (x, y)$. $S_{test}(\omega, \vec{\mathbf{r}})$ and $S_{ref}(\omega, \vec{\mathbf{r}})$ represent the spectrum of the test and reference signal, respectively, for each transverse position, while $\varphi_{test}(\omega, \vec{\mathbf{r}})$ and $\varphi_{ref}(\omega, \vec{\mathbf{r}})$ are the phases of the pulse beam under test and a reference beam (often derived from the test pulse itself). Finally, τ represents the time delay between both

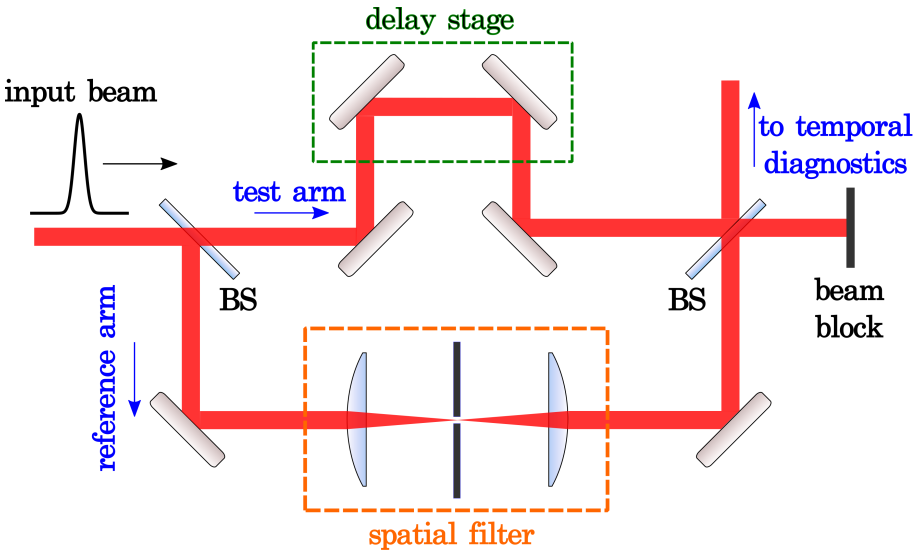

Figure 2.13: Scheme for a SI setup.

beams.

The extraction of the phase of the test pulse phase, $\varphi_{test}(\omega, \vec{\mathbf{r}})$ is done in a similar way as in SI [55], but now an extra step is required since we have no knowledge of the phase of the reference pulse, $\varphi_{ref}(\omega, \vec{\mathbf{r}})$. This situation can be solved by spatially filtering the reference pulse, resulting in a flat wavefront. Under such conditions $\varphi_{ref}(\omega, \vec{\mathbf{r}}) = \varphi_{ref}(\omega)$. The determination of $\varphi_{test}(\omega, \vec{\mathbf{r}})$ is easier now, since we only need to characterize $\varphi_{ref}(\omega)$ using a temporal diagnostic, a task that can be accomplished by a temporal characterization method/diagnostic, such as FROG, SPIDER or d-scan (d-scan will be introduced in chapter 3).

While the spatiotemporal SI works, it has some issues to address, namely the potential occurrence of nonlinear effects while focusing the beam into the spatial filter (pinhole) [75]. In order to avoid such undesired effects, a better approach should get rid of the focusing altogether.

The STARFISH is a spatiotemporal pulse characterization technique that relies in spectral interference between a (delayed) reference pulse an a pulse under test. Unlike other free-space-based methods, STARFISH relies on a two-port fiber-coupler interferometer and a spectrometer, translating into a simple to implement and alignment free spatio-spectral characterization method [74]. The spatio-temporal characteristics can be obtained from the spatio-spectral data via Fourier Transform. The STARFISH schematic is shown in Figure 2.14. A beam under test is split into two replicas by a beamsplitter. Both beams are then steered into a custom designed two-port single-mode fiber (4 μm

diameter) able to support a broadband spectral region from 680 nm to 900 nm, enabling the characterization of ultrashort pulses from a Ti:sapphire oscillator [76] and a hollow-core fiber (HCF) [77]. The fiber port for the test arm is mounted on a motorized stage for a transverse spatial scan. The reference fiber port is placed at a location that covers all spectral components of the beam.

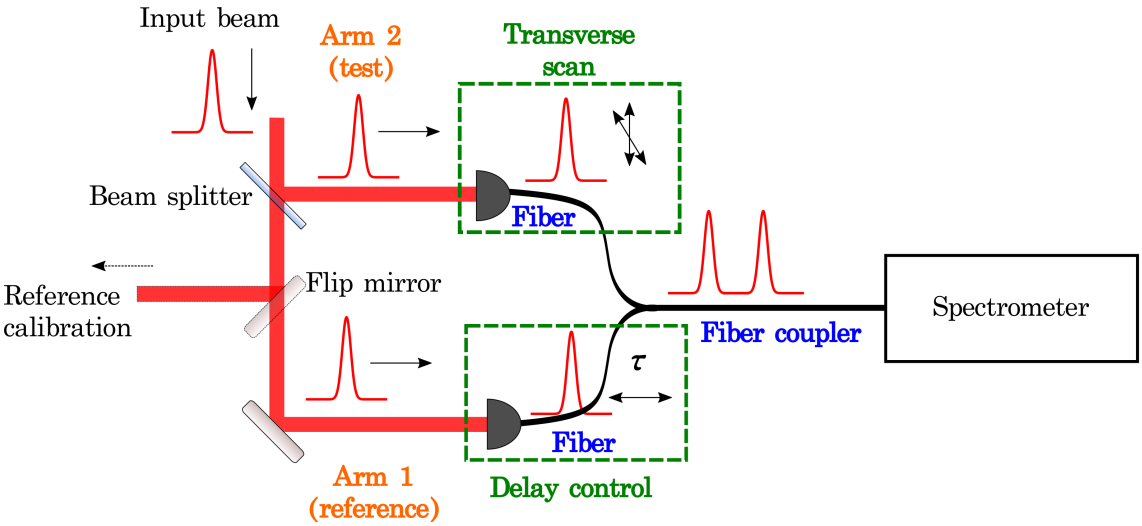

Figure 2.14: Schematic of the STARFISH technique.

The equation for the STARFISH interferogram is the same as Eq. 2.25, so the same treatment described above for the SI can carry over to the treatment of STARFISH.

This method was successfully applied to the measurement of a Ti:sapphire oscillator [76] as well as a the characterization of pulses from a HCF [77].

3 The d-scan technique

"If I have seen further it is only by standing on the shoulders of giants"

Sir Isaac Newton

The author thanks Miguel Miranda, creator of the d-scan technique, for the short but very fruitful discussions on d-scan, as well as the sound advices. This chapter tries to gather the fundamental properties of this technique, explore the property of redundancy (through studies of pulse retrieval under different trace sampling conditions), as well as comment on new developments from the literature. The sign convention on electric fields adopted in this thesis lead to a slight variation in the d-scan related equations of most d-scan papers. Please refer to the annex on sign conventions.

3.1 Dispersion scan (d-scan)

The d-scan technique [78, 79] is a novel method for the measurement and compression of ultrashort pulses that does not rely on spectral shearing nor on spectrally resolved autocorrelation. It relies instead on the manipulation of the spectral phase of a single pulse under test using a pulse compressor and the subsequent measurement of the spectrum arising from the interaction of said pulse on a medium with an optical nonlinearity (Figure 3.1). We will now concentrate on d-scan setups with pulse compressors comprised of DCMs and a pair of glass wedges. Other compressor types will be mentioned later.

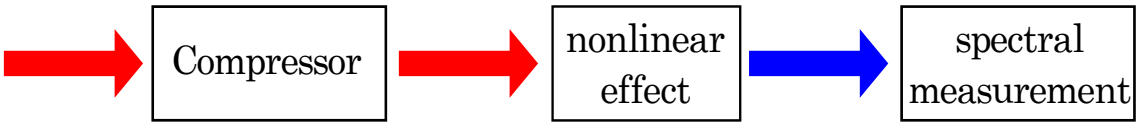

Figure 3.1: General sequence used in a generic d-scan measurement.

To understand the principle of d-scan technique, let us recall how we express the electric field of a pulse (in frequency domain), $\tilde{E}$,

$$\tilde{E}(\omega) = \left|\tilde{E}(\omega)\right| e^{-i\varphi(\omega)}, \tag{3.1}$$

it becomes clear that to fully characterize $\tilde{E}(\omega)$, it is necessary to determine two quantities, namely, its amplitude, $\left|\tilde{E}(\omega)\right|$, and spectral phase, $\varphi(\omega)$. One of these quantities, the amplitude is readily obtainable since it can be extracted from the pulse spectrum,

$$\mathcal{S}(\omega) \propto \left|\tilde{E}(\omega)\right|^2. \tag{3.2}$$

The other quantity $\varphi(\omega)$ is more tricky to obtain, as there is no device that can directly measure the spectral phase in the same way as the spectrometer can measure the spectral amplitude. Eq. 3.2 has a degree of freedom that can be exploited for pulse characterization, i.e., it is insentitive to the phase. Transformations like the following,

$$\tilde{E}(\omega) \rightarrow \tilde{E}(\omega)e^{-i\rho(\omega)}, \tag{3.3}$$

where $\rho(\omega)$ is an additional, arbitrary spectral phase, leaves Eq. 3.2 invariant. It is not difficult to obtain a quantity that is dependent on the spectral phase of a pulse. For that, we will rely on a nonlinear optical effect, e.g., second-harmonic generation (SHG). The SHG effect, which for the case of an instantaneous nonlinearity amounts to squaring the fundamental electric field in the time domain (cf. Eq. 3.4), yields a nonlinear signal whose spectrum depends on ρ and can be measured by a spectrometer.

$$\tilde{E}(\omega)e^{-i\rho(\omega)} \xrightarrow{\mathcal{F}^{-1}} E(t,\rho) \xrightarrow{\times E(t,\rho)} E^2(t,\rho) \xrightarrow{\mathcal{F}} \tilde{E}_{SHG}(\omega,\rho) \rightarrow \left|\tilde{E}_{SHG}(\omega,\rho)\right|^2 = S_{SHG}(\omega,\rho). \tag{3.4}$$

An easy choice for $\rho(\omega)$ comes from the conventional few-cycle compressor made of DCMs and a pair of glass wedges. Hence the varying compressor phase is $\rho(\omega) = zk(\omega)$, where z is the amount of glass (i.e., wedge insertion) the pulse travels through (with reference to the amount of glass that maximizes the nonlinear signal, $z = 0$) and $k(\omega)$ the absolute value of the wavevector in the media, which can be, e.g., BK7 glass or fused silica. The pulse (in the frequency domain) can then be described by $\tilde{E}(\omega)e^{-izk(\omega)}$. Figure 3.2 shows a typical setup for SHG-based d-scan, where the pulse emerges from the compressor (DCMs + wedges) with a total phase given by $\Phi(\omega, z) = \varphi(\omega) + zk(\omega)$. The beam is then focused on a type-I BBO crystal, creating the SHG signal, $S_{SHG}(\omega,\rho)$, that is measured by the spectrometer. Recording the nonlinear spectrum $S_{SHG}(\omega,\rho)$ as a function of glass insertion allows us to obtain the so-called d-scan trace. Figure 3.3 shows four simulated traces calculated with Eq. 3.4 using a sech-squared pulse centered at 800 nm, capable of supporting a TL 4 fs pulse. Each trace has a different phase $\varphi(\omega)$, namely, a flat phase, a phase with pure GDD of 30 fs^2, one with TOD of 60 fs^3, and

another with FOD of 350 fs^4.

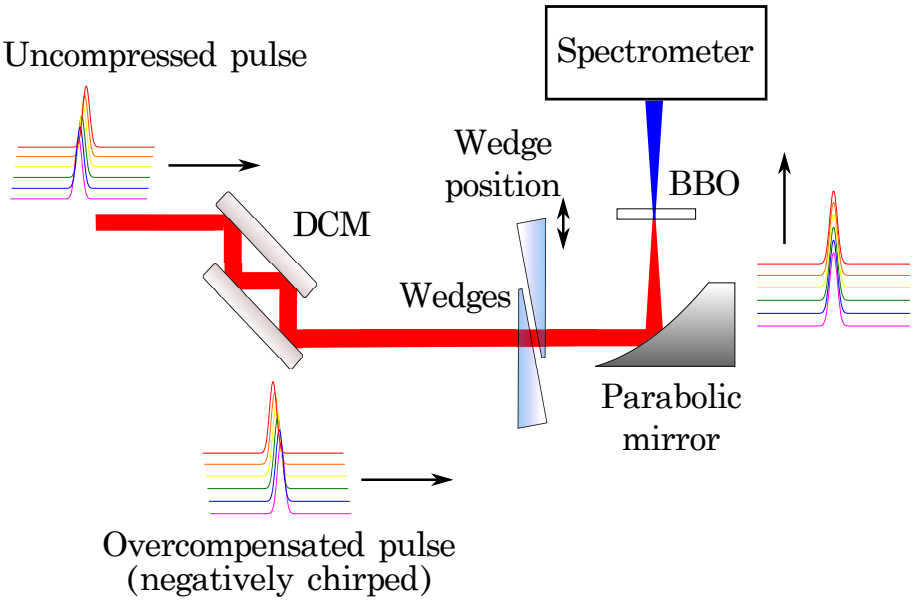

Figure 3.2: D-scan schematic.

With the fundamental spectrum, $\mathcal{S}(\omega)$, the measured d-scan trace, $S_{meas}(\omega, z)$, and knowing the equation to simulate a d-scan trace [78], $S_{sim}(\omega, z)$,

$$S_{sim}(\omega, z) = \left| \int_{-\infty}^{+\infty} E_{SHG}(t, z) e^{-i\omega t} dt \right|^2 = \left| \int_{-\infty}^{+\infty} \left(\int_{-\infty}^{+\infty} \tilde{E}(\Omega) e^{-izk(\Omega)} e^{i\Omega t} d\Omega \right)^2 e^{-i\omega t} dt \right|^2, \tag{3.5}$$

we are able to retrieve the spectral phase by using a mathematical optimization algorithm (e.g. Nelder-Mead, the fast iterative retrieval algorithm [80]), where the root-mean-square (rms) error, G, between the acquired, $S_{meas}(\omega, z)$, and simulated traces $S_{sim}(\omega, z)$, is minimized,

$$G = \sqrt{\frac{1}{N_\nu N_z} \sum_{i,j} \left(S_{meas}(\omega_i, z_j) - \mu_i S_{sim}(\omega_i, z_j) \right)^2}, \tag{3.6}$$

being N_ν and N_z the number of points in the frequency and insertion ranges, respectively. The response function, $\mu(\omega)$, is a multiplicative factor that accounts for the phase-matching and pulse propagation inside the nonlinear medium, and can be obtained by differentiating G with respect to μ [78], leading to,

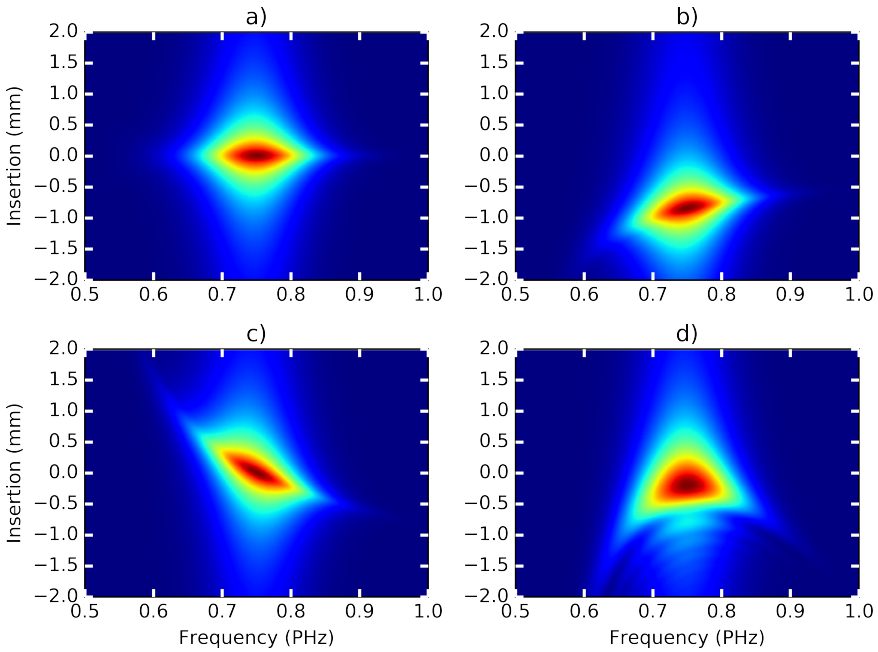

Figure 3.3: Examples of simulated SHG d-scan traces. a) Transform-limited pulse; b) with group-delay dispersion of 30 fs^2; c) with third-order dispersion of 100 fs^3; d) with fourth-order dispersion of 350 fs^4.

$$\mu_i = \frac{\sum_j S_{meas}(\omega_i, z_j) S_{sim}(\omega_i, z_j)}{\sum_j S^2_{sim}(\omega_i, z_j)}. \tag{3.7}$$

The full pulse temporal profile can now be reconstructed as long as the fundamental spectrum of the pulse is known. The simulated trace, $S_{sim}(\omega, z)$ is updated whenever the simulated phase, $\varphi(\omega)$, is updated. The d-scan algorithm has the flexibility in the choice of representation of the simulated spectral phase, in the sense that it can be expressed, e.g., either as a Fourier polynomial (i.e., a trigonometric polynomial) or a regular polynomial [78]. In this way, it is only necessary for the optimization algorithm to choose the coefficients of the polynomials, rather than explicitly retrieve all points of the spectral phase. This reduced number of variables to be determined also leads to a relatively faster retrieval process. When the minimization algorithm stops, either by reaching a set number of iterations or a certain error threshold, it returns the spectral phase, and with it, we make a trivial Fourier transform to the time domain so as to determine the pulse duration, and most importantly, the pulse temporal profile.

Interpretation of d-scan traces

As previously seen in chapter 2, FROG traces can be interpreted as spectrograms as they show the pulse's nonlinear spectral content as a function of delay. In d-scan, not only is it possible to extract quantitative information of a pulse under test but also very intuitive qualitative information. It will be shown that a d-scan trace can also have an intuitive interpretation. A d-scan trace is not dependent on the absolute phase nor on a linear phase, i.e., a phase $\varphi(\omega) = \varphi_0 + a(\omega - \omega_0)$ will leave the trace, $S(\omega, z)$, invariant (the demonstration relies in the direct substitution of the linear phase in Eq. 3.5). Hence, a d-scan trace will only be dependent on higher-order dispersion, e.g., GDD and higher. From Figure 3.3, we observe that transform-limited pulses or pulses with constant group-delay are symmetric with respect to the axis defined by the optimal compression position ($z = 0$). A pulse with positive quadratic phase will shift to a lower position in the insertion range by an amount that is proportional to its GDD, because the amount of insertion necessary to reach a optimal compression is lower, thus, this position is reached sooner. The amount of displacement can be obtained with $\Delta z = -\frac{d^2\varphi}{d\omega^2} \diagup \frac{d^2k}{d\omega^2}$. The tilt of the trace in the case of a pulse with pure GDD arises because the phase of the pulse is not the only phase that contributes to the calculation of the trace, as the contribution of the pulse compressor, $zk(\omega)$ is also involved. Pulses with a cubic phase, $\varphi \propto (\omega - \omega_0)^3$, have a linear second derivative, $\frac{d^2\varphi}{d\omega^2}$, which translates into a monotonic variation of the optimal compression position as a function of frequency, no shift is observed, since $\frac{d^2\varphi}{d\omega^2}(\omega_0) = 0$. Pulses with quartic phase have a quadratic second derivative, and this translates into a typical "arch"-like structure.

Despite the considered phases being having either even or odd symmetry (excluding the TL case), the shown traces don't fully reflect this symmetry, indeed, all of them seem to have an additional tilt which is attributed to $k(\omega)$, a function which exhibits no symmetry (neither even nor odd), and contributes to the total phase $\Phi(\omega, z) = \varphi(\omega) + zk(\omega)$ in a non-uniform way depending on frequency. This tilt is most obvious, e.g., in the cases of quadratic and quartic phases. In the quadratic phase case, frequencies equidistant from the central frequency are compensated at different values of insertion. In the quartic phase case, the "arch"-like structure decays at different rates for frequencies equidistant from the central frequency, and so on.

3.2 Redundancy

A convenient property to have for pulse characterization is redundancy, i.e., the flexibility to discard, when necessary, part of the acquired data while still being able to recover and retrieve relevant results. This concept was first approached in [78], though this concept was exemplified with a rather conservative example, i.e., a trace that was only clipped on the sides (along the wavelength range) with low signal, leaving the most intense part of the trace intact. However, the study of the redundancy property of the d-scan technique when clipping along the glass insertion domain was not explored yet, and it is the focus of this subsection. In this subsection, we will explore new results pertaining to the concept of redundancy of d-scan. Through simulations, we show that the d-scan retrieval process has more flexibility on the choice of how and where to clip a trace and apply these same choices to common scenarios that may arise when trying to retrieve experimentally acquired d-scan traces. In the following simulations, a gaussian pulse centered at 800 nm, capable of supporting 10 fs pulse when transform-limited, with a spectral phase, $\varphi(\omega) = \frac{1}{2}cos(\alpha_1 \times (\omega - \omega_0)) \times sinh(\alpha_2 \times (\omega - \omega_0 - \alpha_3))$, where $\alpha_1 = 20$ fs, $\alpha_2 = 15$ fs and $\alpha_3 = 0.4 \times 10^{14}$ rad/s was used. Knowing the exact pulse spectral phase allows us to compute the rms field error ϵ, [81] to compare how close the retrieved electric field is to the exact electric field

$$\epsilon = \left| \frac{1}{2\pi} \int_{-\infty}^{+\infty} \left[\tilde{E}(\omega) - \tilde{E}_{ret}(\omega) \right]^2 d\omega \right|^{\frac{1}{2}}, \tag{3.8}$$

where $\tilde{E}(\omega)$ is the exact electric field and $\tilde{E}_{ret}(\omega)$ is the retrieved electric field. All retrieved fields have a sub-2% rms field error. Consider the case shown in Figure 3.4, which corresponds to a scenario where we assume that the acquired trace is saturated only near the optimal compression position. A retrieval attempt using the full trace including the saturated region leads to inaccurate results. Nevertheless we clip part of the trace that is saturated (i.e., clipping along the glass insertion axis) and perform again the retrieval routine.

Even though the central, more intense (and in this case saturated) portion of the trace was removed prior to retrieval, we can clearly see that the d-scan algorithm successfully retrieved the spectral phase using only the remaining part of the trace. It is therefore possible to clip traces along the the glass insertion range and this property proves useful for the aforementioned case (saturation).

We now explore another scenario where only part of the trace is contained inside the trace window (normally, due to not having enough positive/negative dispersion range in

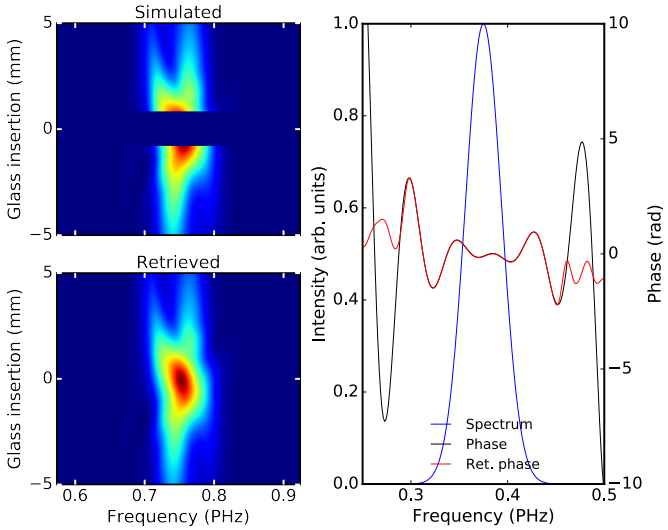

Figure 3.4: Phase retrieval of a d-scan trace clipped in the center.

the compressor) as depicted in Figure 3.5.

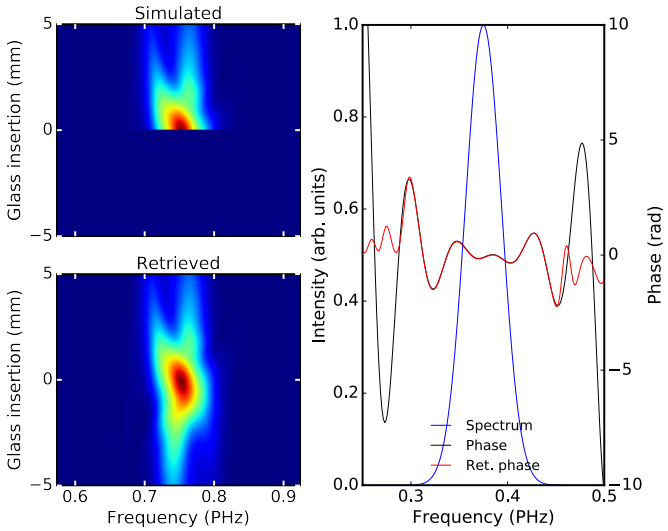

Figure 3.5: Phase retrieval of a partially dispersion-scanned trace.

There is no saturation in this case, but we start from a partial trace, nevertheless, the successful phase retrieval from a partial trace is evident.

Pulse retrieval while leveraging the redundancy property can be done even when the omitted parts of the trace are not contiguous zones, as shown in Figure 3.6.

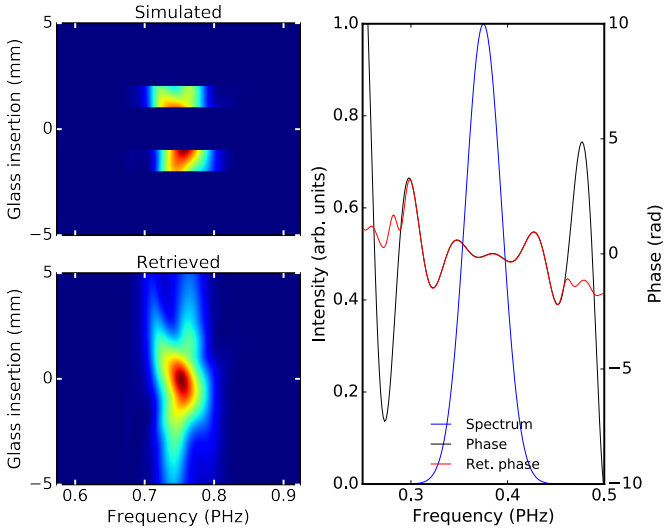

Figure 3.6: Phase retrieval from a trace with non-contiguous zones discarded.

Another scenario arises when bad sampling parameters along the insertion axis are chosen (e.g., scanning speed faster than nonlinear spectrum acquisition), cf. Figure 3.7 and Figure 3.8 for the even and uneven spacing cases, respectively.

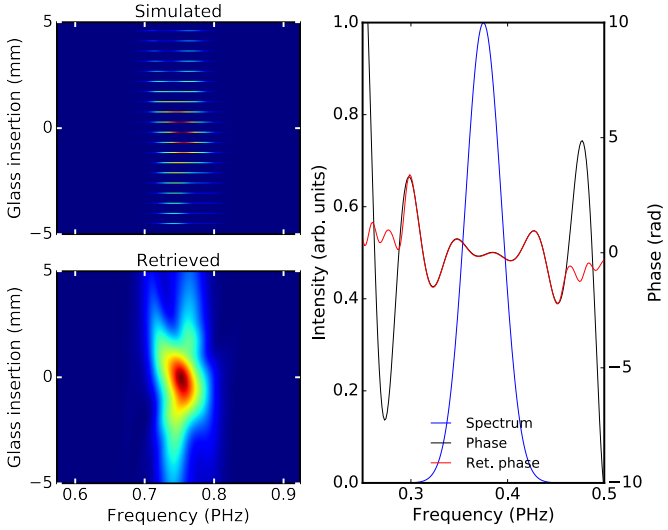

Figure 3.7: Phase retrieval when the traces is badly sampled in the insertion range; with just 10% of total trace (21 spectra of 210).

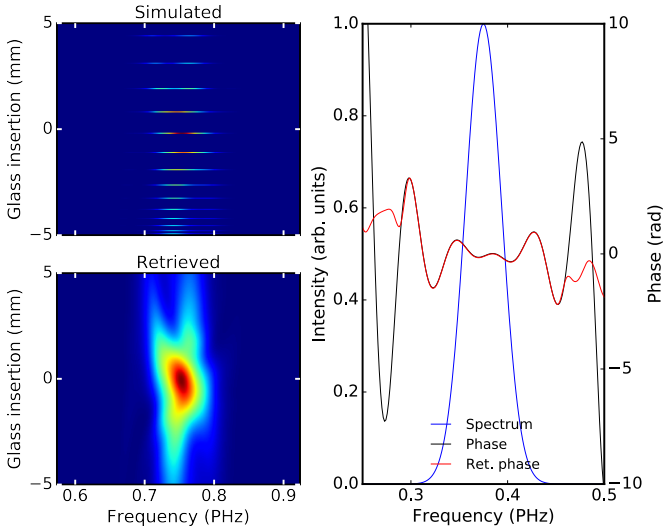

Figure 3.8: Phase retrieval when the trace is badly sampled in the insertion range; Uneven spaced slices.

Both these examples suggest that trace clipping along the glass insertion axis can be arbitrary. This kind of clipping operations need not be only effected along the insertion axis. It is possible to implement the same kind of treatment along the frequency/wavelength range, as shown in Figure 3.9.

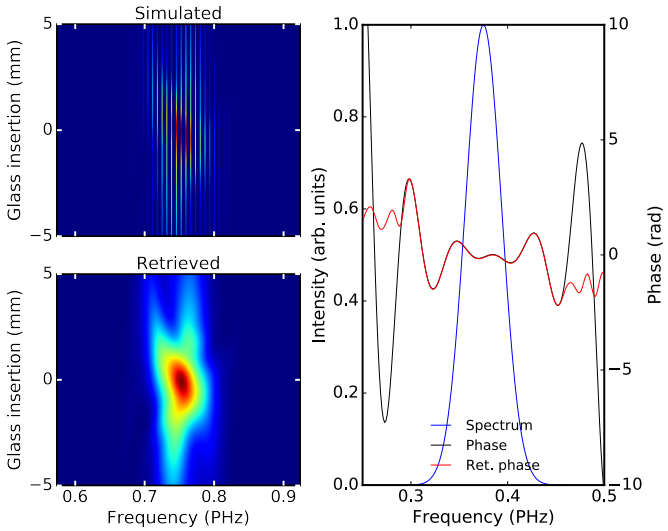

Figure 3.9: Phase retrieval when the trace is badly sampled in the frequency range.

Table 3 lists the E-field error of all the aforementioned pulse retrieval cases. Their

respective spectral phases are plotted in Figure 3.10.

Case	E-field error ϵ (%)
Figure 3.4 (case 1)	1.7
Figure 3.5(case 2)	1.9
Figure 3.6(case 3)	1.6
Figure 3.7(case 4)	1.9
Figure 3.8(case 5)	1.8
Figure 3.9(case 6)	1.7

Table 3: E-field error ϵ of all the mentioned cases of pulse retrieval described in this sub-section.

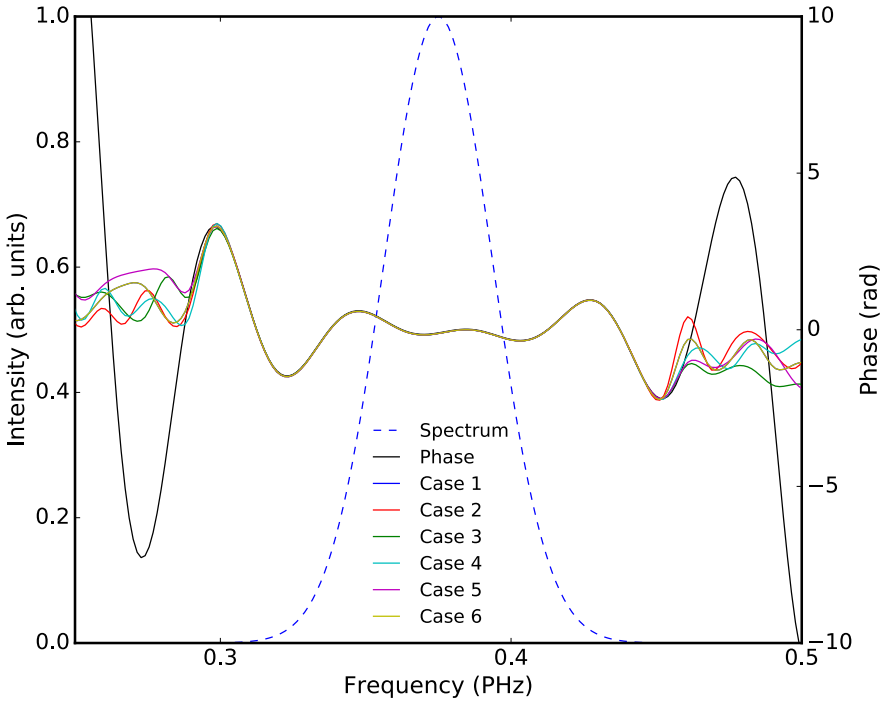

Figure 3.10: Spectrum, simulated phase and retrieved phases of the different retrieval cases.

Ultimately, the theoretical minimum number of nonlinear spectra required for pulse retrieval can be determined as follows. Since d-scan traces contain $N = N_z \times N_\nu$ points, N_z for the number of glass insertions and N_ν for the number of frequencies/wavelengths, while the number of points needed to characterize a pulse, is $N_\nu + N_\nu = 2N_\nu$, i.e., N_ν points for the amplitude and another N_ν points for the spectral phase. It follows that the

minimum number of insertions, N_z, to retrieve a pulse is, $N = 2N_\nu$, or in other words, $N_z = 2$, in agreement with the limit presented in [82]. However, it is advisable to avoid retrieving pulses with just the bare theoretical minimum number of insertions.

3.3 Advantage of using d-scan for the characterization of few-cycle pulses

One of the advantages of the d-scan technique is the fact that it does not involve any temporal delay between pulse (under test) replicas, which makes it an inline method. Additionally, the main elements to perform a d-scan are usually already present/necessary in a setup, namely the pulse compressor.

Every technique, apparatus or equipment built for the purpose of measurement of physical quantities has some limitations, be they by design and/or by physical principles. This statement naturally includes pulse characterization methods. In this section, we will estimate the limits of applicability of the d-scan method, with respect to the values of pulse duration one could expect to be able to measure. A numerical estimate of the upper bound can be obtained by some modeling. We will begin by considering several gaussian pulses centered around 800 nm (typical for Ti:sapphire lasers), and with different pulse durations, assumed to be transform-limited, which is as reasonable approximation for a pulse in the optimal compression position. Next, a certain amount of group-delay dispersion is applied to the pulses, to simulate wedge insertion (GDD is the first-order approximation of the wedge dispersion; GD only accounts for the pulse bulk shifts in time, and so, it is ignored). From the resulting pulses, we extract their pulse duration. The results are depicted in Figure 3.11.

From Figure 3.11, we can see that as we increase the duration of the pulse to be measured, the gradient of the plot becomes more and more orthogonal to the GDD axis, meaning that the sensitivity to the variation of dispersion is smaller. On the other hand, it is evident that pulse characterization of shorter pulses is favored by the physics that it is based on, as shorter pulses have an enhanced sensitivity to the variation of dispersion. The suitability of d-scan in the measurement of few-cycle pulses contrast with the difficulty other methods such as SPIDER and FROG face when scaling down for the measurement of these same pulses.

The maximum pulse duration that the scanning version of d-scan (i.e., comprised of DCMs and a pair of wedges) lies around ~35 fs (cf. Figure 3.12), an arbitrary choice admittedly, since longer pulses, say, 45 fs, may still be retrieved, though with less likelihood, as the nonlinear spectra in the traces become less and less dependent on the spectral

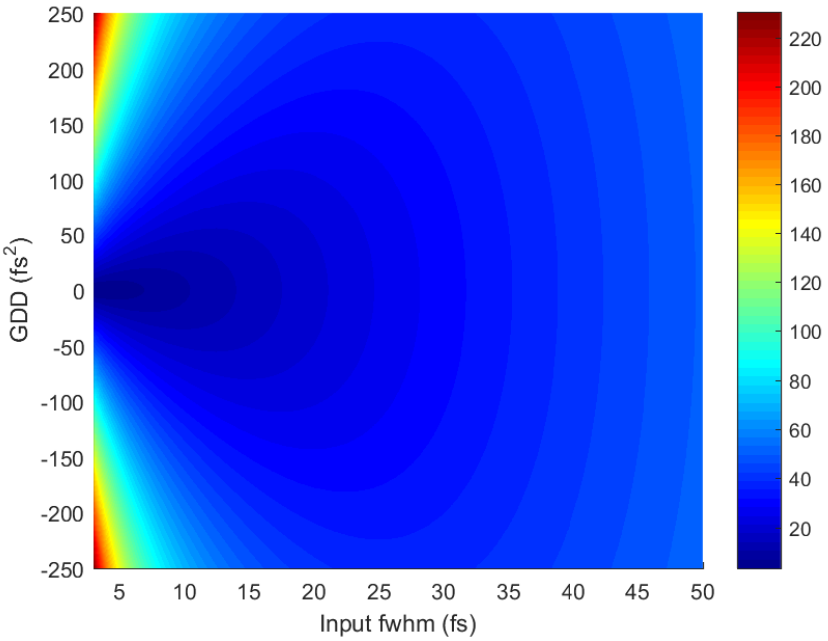

Figure 3.11: Initial pulse duration (3 to 50 fs) vs added GDD (-250 to 250 fs^2), with color-coded output duration (fs). Gaussian pulses centered around 800 nm.

phase variations $\Phi(\omega, z)$.

A lower bound for the pulse duration d-scan experimentally manages to retrieve, at the time of writing, is 2.2 fs [83], which amounts to a pulse with 1.04 optical cycles.

Figure 3.11 shows that for longer pulses, the amount of dispersion imparted by conventional compressors made of DCMs and a pair of wedges is small. However, the d-scan concept (c.f. Figure 3.1) is more general than the one presented so far. In fact, a pulse compressor can be made with other more dispersive elements such as prisms [84] or gratings [85]. An increase in the amount of variable dispersion is not the only advantage of such setup. One may initially assume the need of the explicit equation for the additional phase imparted by the prisms, $\rho(\omega)$, which are derived in [31, 86]. It turns out that the explicit knowledge of $\rho(\omega)$ is actually unnecessary, as $\rho_{prism}(\omega)$ (as well as most monotonous dispersion curves) can be expanded as a Taylor series (usually only up to 4-th order needed), and the Taylor coefficients are simultaneously retrieved alongside the spectral phase [87], i.e., the algorithm that retrieves the pulse spectral phase $\varphi(\omega)$ additionally retrieves the coefficients of the Taylor expansion of $\rho_{prism}(\omega)$ that are related to the prisms GDD, TOD and FOD, when necessary. This approach proved to be successful in the characterization of pulses from both a Ti:sapphire laser oscillator and amplifier.

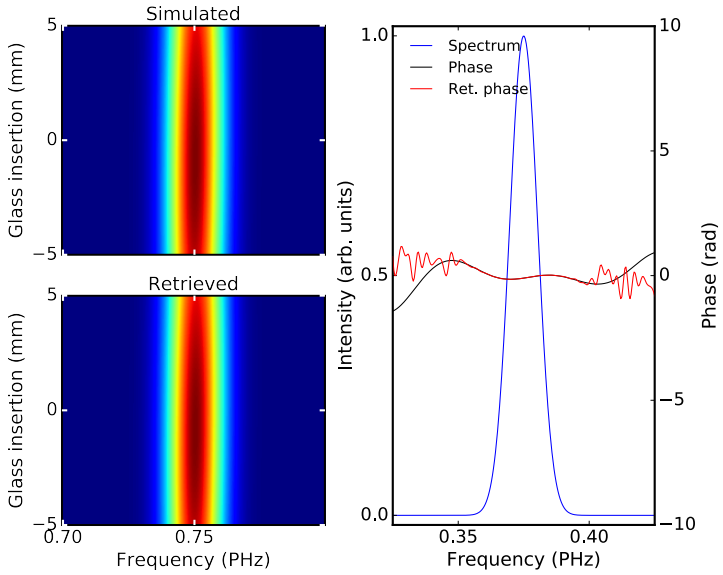

Figure 3.12: Phase retrieval of a longer gaussian pulse centered at 800 nm, with a duration of 35.3 fs and same spectral phase as the pulses in section 3.2.

This self-calibrating d-scan can be useful in the characterization of pulses from laser amplifiers which use pairs of prisms or gratings for the output pulse dispersion management, and so, these setups can be readily adapted into a self-calibrating d-scan setup, allowing us to leverage already existent optical elements from the laser itself and benefit from the advantages of the d-scan technique, i.e., find the insertion of optimal pulse compression and/or determine the pulse spectral phase (and consequently the temporal profile) for a given prism insertion, not to mention measuring the pulse TOD too.

3.4 Single-shot d-scan

Up to now, all the d-scan setups described were of the scanning variant, i.e., they require moving parts (to vary variable glass insertion) to acquire a d-scan trace. There are though situations where the pulse repetition rate is low, a situation which warrants a single-shot version of d-scan, where the scanning version of d-scan cannot address.

It is clear that unlike the scanning versions of d-scan, a single-shot implementation should avoid moving parts. Current single-shot d-scans systems rely on a beam propagation through a prism [88, 89], so that each part of the beam acquires a different amount of dispersion. Afterwards the beam is focused into a SHG crystal, generating a spatially dependent upconverted signal, $S(\lambda, x)$, where λ is the wavelength, and x is the beam

transverse direction. $S(\lambda, x)$ is then acquired by an imaging spectrometer, allowing us to obtain a d-scan trace, at which point we can apply the already developed d-scan retrieval algorithms to reconstruct the pulse. These two recent implementations ([88] and [89]) of single-shot d-scan were shown to be capable of characterizing few-cycle pulses.

A recent single-shot technique based on based on automatically phase-matched transverse SHG (TSHG) in a random nonlinear crystal was presented in [90].

3.5 Comparison with SPIDER

The d-scan and SPIDER techniques are very different in nature, hence, our comparison will be mostly focused on the obtained results, i.e., the spectral phase. In a study (cf. 3.13) made with a commercial Ti:sapphire laser oscillator [91], it was shown that there is a very good agreement between both methods.

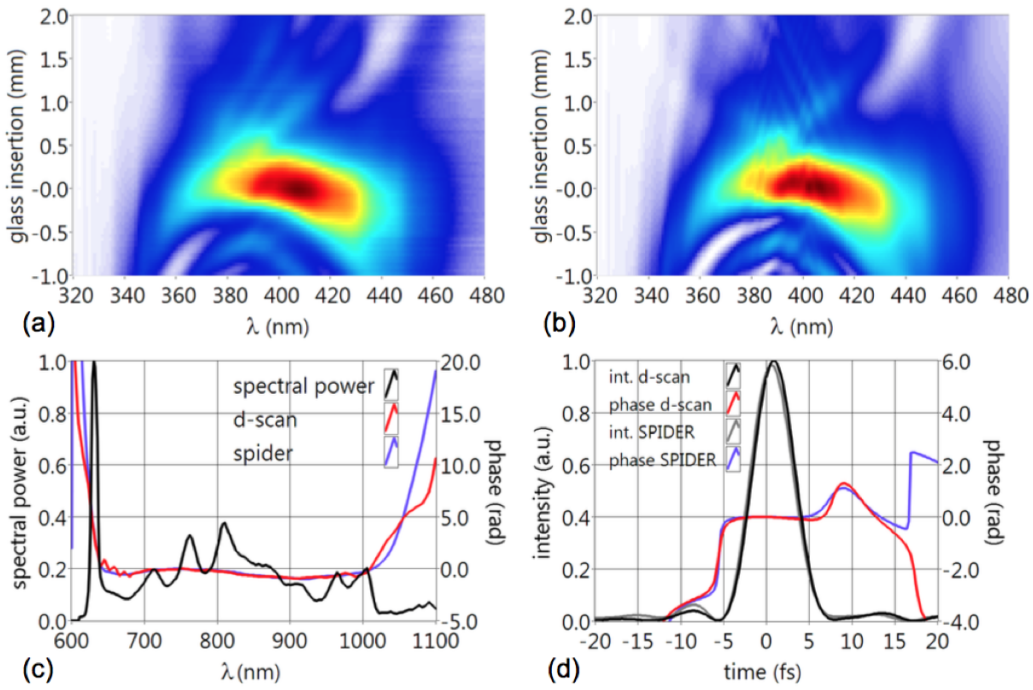

Figure 3.13: D-scan and SPIDER measurements. Top left) measured d-scan trace; top right) retrieved d-scan trace; bottom left) spectrum and spectral phases retrieved by SPIDER and d-scan; bottom right) pulse temporal intensity and temporal phase retrieved by SPIDER and d-scan. [91]

However, the characterization of pulses in the few-cycle regime poses some chal-

lenges for SPIDER as it requires a stringent calibration of the delay, τ, between pulses [59]. Measurements made with a bad delay calibration will lead to an additional quadratic contribution to the retrieved phase, hence, resulting in a wrong pulse phase. A wavelength calibration error from SPIDER interferograms can also induce errors in the estimation of the pulse duration [56].

3.6 Comparison with FROG

An initial comparison between d-scan and FROG was made in [92], with measurements from a Ti:sapphire oscillator. Figure 3.14 below (taken from [92]) shows a d-scan trace as well as a few FROG traces, where each FROG trace corresponds to a different glass insertion of a conventional DCMs and wedge compressor. A plot of pulse duration vs glass insertion is shown, made with values retrieved from d-scan and FROG measurements, showing good agreement. We can notice an advantage of d-scan over FROG, in the sense that, we have the possibility of pinpointing the position of optimal compression from a single measurement, a feature that FROG lacks and needs several measurements to approach. On the other hand, just one measurement and retrieval of a d-scan trace is enough to know the pulse electric field for any value of glass insertion, which is of great practical application.

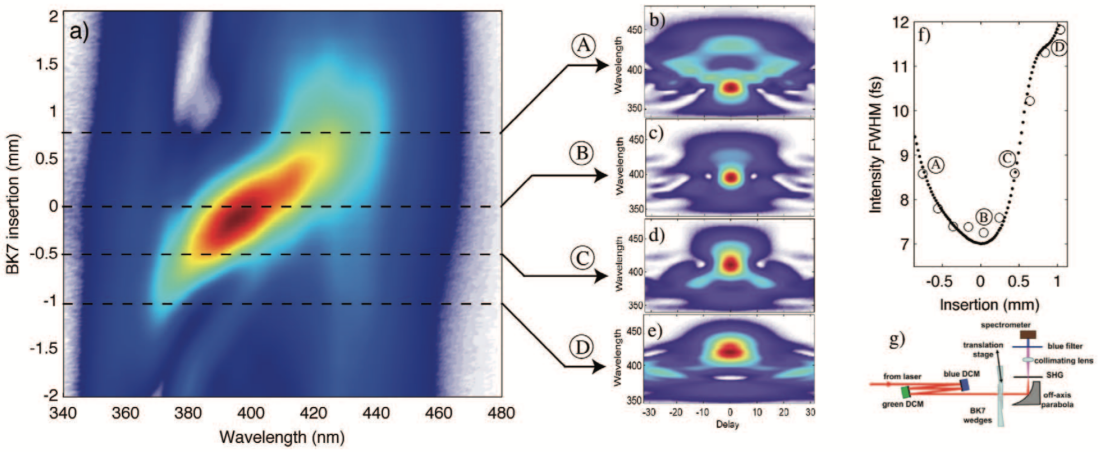

Figure 3.14: SHG d-scan and SHG FROG measurements [92].

3.6.1 Comments on FROG retrieval

Making a comparison between pulse characterization methods can become tricky, specially when there is a time gap (as well as the improvement on laser sources and tech-

nique implementation) between the introduction of said techniques. It would be inappropriate to compare the d-scan method with the FROG without mentioning the latter's recent improvements and achievements since its inception [47]. We will start by talking about the mature FROG retrieval algorithms, their characteristics and disadvantages, and move on to the very recent ptychographic reconstruction algorithm, a new and robust retrieval algorithm, finally detailing a d-scan inspired FROG retrieval algorithm, and showing that the d-scan retrieval algorithm is very general, able to be applied to both d-scan and FROG retrievals (with trivial modifications), thus allowing a pathway for d-scan users to quickly re-use/adapt the same code to retrieve FROG traces and/or vice-versa.

Besides the basic algorithm [48] and the generalized projections (GP) [50] for FROG, other method with widespread usage is the principal component generalized projections (PCGP) [51, 52] algorithm, which will be described here.

The PCGP algorithm starts with two guesses for the pulse $E(t)$ and the gate $G(t)$, which will be used to generate an intermediate matrix that incorporates the experimental data from the FROG trace, hence creating a new FROG trace. This new FROG trace is then factorized by a singular-value decomposition (SVD) method or by the power method (from linear algebra) resulting in the two new iterations for $E(t)$ and $G(t)$. The diagram for the PCGP method is presented in Figure (3.15).

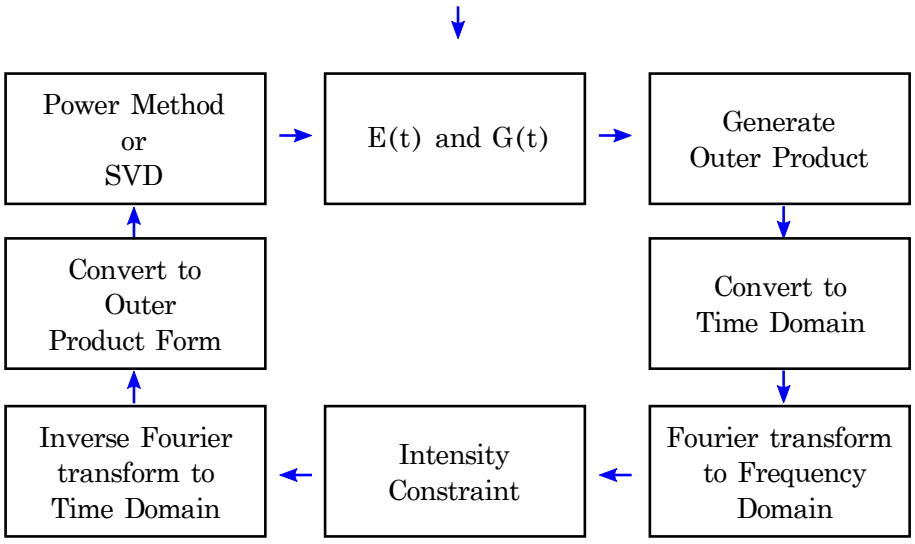

Figure 3.15: PCGP algorithm diagram.

This algorithm usually starts with gaussian pulses for the pulse itself, $E(t)$, and the gate pulse, $G(t)$, sampled in time, as initial guesses. The gate pulse is derived from $E(t)$, and depends on the type of nonlinear optical interaction, e.g., for PG-FROG, $G(t) =$

$|E(t)|^2$. From these initial guesses and by means of a tensor product we can construct a matrix, O, as follows,

$$O = E \otimes G = \begin{bmatrix} E(t_1)G(t_1) & E(t_1)G(t_2) & E(t_1)G(t_3) & \dots & E(t_1)G(t_N) \\ E(t_2)G(t_1) & E(t_2)G(t_2) & E(t_2)G(t_3) & \dots & E(t_2)G(t_N) \\ E(t_3)G(t_1) & E(t_3)G(t_2) & E(t_3)G(t_3) & \dots & E(t_3)G(t_N) \\ \vdots & \vdots & \vdots & \ddots & \vdots \\ E(t_N)G(t_1) & E(t_N)G(t_2) & E(t_N)G(t_3) & \dots & E(t_N)G(t_N) \end{bmatrix}. \tag{3.9}$$

The transformation from O to the FROG signal in the time domain is accomplished by shifting each row by an increasing amount, from 0 to N-1, where N is the number of samples. The resulting matrix is then,

$$O' = \begin{bmatrix} E(t_1)G(t_1) & E(t_1)G(t_2) & E(t_1)G(t_3) & \dots & E(t_1)G(t_{N-1}) & E(t_1)G(t_N) \\ E(t_2)G(t_2) & E(t_2)G(t_3) & E(t_2)G(t_4) & \dots & E(t_2)G(t_N) & E(t_2)G(t_1) \\ E(t_3)G(t_3) & E(t_3)G(t_4) & E(t_3)G(t_5) & \dots & E(t_3)G(t_1) & E(t_3)G(t_2) \\ \vdots & \vdots & \vdots & \ddots & \vdots & \vdots \\ E(t_N)G(t_N) & E(t_N)G(t_1) & E(t_N)G(t_2) & \dots & E(t_N)G(t_{N-2}) & E(t_N)G(t_{N-1}) \end{bmatrix}. \tag{3.10}$$

We can notice that the columns of O' comprise the multiplication of the sample pulse, $E(t)$, with the gate pulse, $G(t)$, at different values of the delay τ, namely, $\tau = 0, -\Delta t, -2\Delta t, \dots, 2\Delta t, \Delta t$. Lastly, we must perform column permutation to ensure that the columns of the new matrix are associated with strictly increasing values of τ. Applying the Fourier transform to the columns of the resulting matrix, we get

$$E_{calc}(\tau, \omega) = |E_{calc}(\tau, \omega)|\, e^{i\phi(\tau,\omega)}, \tag{3.11}$$

which is the FROG signal in the frequency domain. Next, we apply an intensity constraint, i.e., the input of the measured trace will be introduced in this step, by replacing the magnitude of E_{calc} with the square root of the magnitude of the FROG trace, $\sqrt{I_{FROG}(\tau, \omega)}$. The new FROG signal $E_{sig}(\tau, \omega)$is given by

$$E_{sig}(\tau, \omega) = \frac{E_{calc}(\tau, \omega)}{|E_{calc}(\tau, \omega)|} \sqrt{I_{FROG}(\tau, \omega)}. \tag{3.12}$$

Figure 3.16 illustrates the FROG trace generation process with the PCGP method, for

a gaussian pulse with TOD.

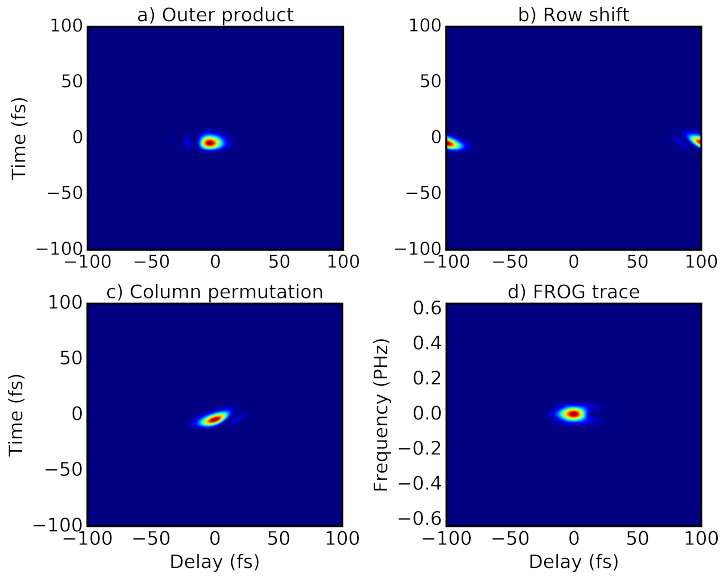

Figure 3.16: FROG trace generation (256×256 points) in PCGP; a) outer product calculated in time domain of a TL 10 fs pulse upon which was added TOD. b) after performing row shift. c) after column permutation. d) FROG trace (central frequency offset).

To obtain the new guesses for the pulse and gate, the new FROG trace undergoes another column permutation and row shifting which are the inverse operations of the two initial ones, this is done so, so that we can revert back to an outer product form. The capability of reverting back to an outer product form, i.e., reversibility, is very useful in PCGP since the outer product can be written as a product of matrices,

$$O = U \times W \times V^t, \tag{3.13}$$

such that U and V^t are orthogonal square matrices, while W is a square diagonal matrix. This factorization can be accomplished by using a singular-vale decomposition (SVD) routine or by using the power method [52].

3.6.2 Ptychographic reconstruction

Ptychography is a method that was initially conceived for phase retrieval in X-ray crystallography [93], having also found applications in diffractive imaging [94, 95]. Ptychography involves the imaging of a sample by recording several diffraction patterns that are generated by the interaction between an object wavefront, $O(\vec{r})$ and a probe wavefront, $P(\vec{r})$,

and where each diffraction pattern corresponds to a different spatial separation between $O(\vec{r})$ and $P(\vec{r})$. The intensity of the resulting wavefront at the detector can be expressed [96] as

$$I_j(\vec{u}) = \left|\mathcal{F}\left[O(\vec{r})P(\vec{r}-\vec{R})\right]\right|^2. \tag{3.14}$$

The ptychographic algorithm retrieval starts with two guesses, one for the object wavefront, $O_j(\vec{r})$ and another for the probe wavefront, $P_j(\vec{r})$, where j is an iteration counter. From these guesses, we form the product $\psi_j(\vec{r}) = O_j(\vec{r})P_j(\vec{r}-\vec{R}_{s(j)})$, where $s(j)$ is an element of a random sequence. The resulting wavefront is

$$\psi'_j(\vec{r}) = \mathcal{F}^{-1}\left[\Psi_j(\vec{r})\right], \tag{3.15}$$

where

$$\Psi_j(\vec{r}) = \sqrt{I_{s(j)}(\vec{r})}\frac{\mathcal{F}\left[\psi_j(\vec{r})\right]}{\left|\mathcal{F}\left[\psi_j(\vec{r})\right]\right|}. \tag{3.16}$$

In this last equation was introduced the square-root of the $s(j)$ diffraction pattern, $\sqrt{I_{s(j)}(\vec{r})}$. The next iterations for the object and probe wavefronts are calculated [96] via

$$O_{j+1}(t) = O_j(t) + \alpha\frac{P_j^*(t-s(j)\Delta t)}{\left|P_j^*(t-s(j)\Delta t)\right|^2_{max}}\left(\psi'_j(t)-\psi_j(t)\right) \tag{3.17}$$

$$P_{j+1}(t) = P_j(t) + \beta\frac{O_j^*(t+s(j)\Delta t)}{\left|O_j^*(t+s(j)\Delta t)\right|^2_{max}}\left(\psi'_j(t)-\psi_j(t)\right) \tag{3.18}$$

where α and β are constants. Recently, an adaptation of a ptychographic algorithm was modified to be applicable to the retrieval of FROG traces [97]. Since the equation for a SHG FROG is given by

$$I_{FROG}(\omega,\tau) = \left|\mathcal{F}\left[E(t)E(t-\tau)\right]\right|^2, \tag{3.19}$$

hence, in this adaptation, the electric field, $E(t)$, plays the part of the object and probe wavefronts and the time delay, τ, plays the role of the spatial offset, $\vec{R}$. We can see that the aforementioned FROG trace has the same mathematical form as Eq. 3.14, thus enabling the use of ptychographic retrieval algorithms (with suitable modifications) to reconstruct the electric field of an ultrashort pulse [97].

3.6.3 Retrieval *à la* d-scan

The ptychographic method is not the only method that enables pulse reconstruction from partial traces. It will be shown here that the simpler conventional d-scan algorithm is sufficiently general to allow us to reconstruct not just d-scan traces but FROG traces as well. For that, let us recall the PCGP algorithm.

Although the PCGP approach has been the preferred approach for phase retrieval in FROG, it is an algorithm that has its shortcomings, and does not reveal one relevant characteristic of the FROG method, namely its redundancy.

While the reversibility factor is beneficial to the retrieval speed in PCGP, it can, on the other hand, present a hindrance to the sampling of the FROG trace [5].

Starting from the d-scan retrieval method, we now investigate the feasibility of applying it of FROG traces. In the author's view, the generation of the FROG trace through the outer product and subsequent row and column manipulation imposes stringent requirements on the sampling of the FROG trace. Observe that $\Delta t = t_{k+1} - t_k$ is intimately connected to $\Delta\tau$, i.e., the sampling in time will also determine the sampling in the delay, $\Delta t = \Delta\tau$. This situation imposes constraints in the sampling of a FROG trace, as illustrated in Figure 3.17.

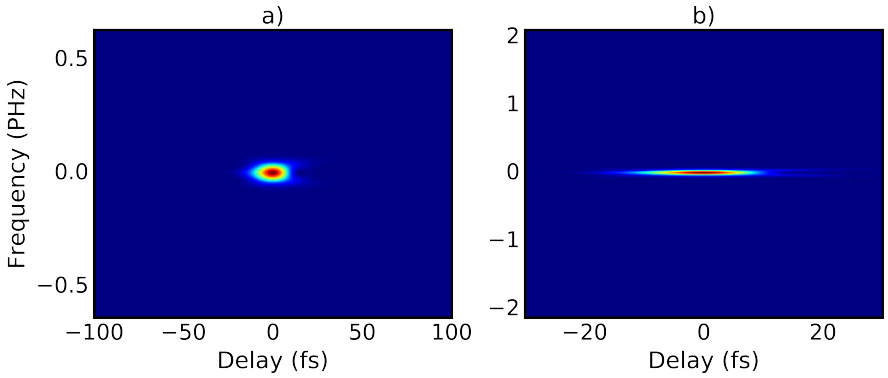

Figure 3.17: FROG sampling. Changes in $\Delta\tau$ leads to changes in the frequency sampling $\Delta\nu$. The central frequency of the traces was subtracted.

We will now consider the pulse in the frequency domain (as is done in d-scan), and apply it to the generation of the FROG trace. The initial guesses, $\tilde{E}(\omega)$, can be given a random spectral phase, while its amplitude can be extracted from the square root of the

[5] In principle, the GP method does not need a coupling between the sampling in the delay with the sampling in time, but it is recommend by the authors to impose such coupling, cf. [48], chapter 10.

fundamental spectrum. The pulse to be measured, $E(t)$, is given by the inverse Fourier transform of $\tilde{E}(\omega)$,

$$E(t) = \int_{-\infty}^{+\infty} \tilde{E}(\omega) e^{i\omega t} d\omega. \tag{3.20}$$

The shifted pulse can also be represented by

$$E(t-\tau) = \int_{-\infty}^{+\infty} e^{-i\omega\tau} \tilde{E}(\omega) e^{i\omega t} d\omega, \tag{3.21}$$

where the factor $\exp(-i\omega\tau)$ represents the translation in time by an amount τ . Eq. (3.21) is what enables us to decouple the sampling requirements, as $\Delta\tau$ is not related to neither Δt nor $\Delta\omega$. The gate function, $G(t)$, is a function of E, and depends on the type of FROG being considered,

$$G(t) = G\left[E(t)\right]. \tag{3.22}$$

The FROG signal, D, can be constructed by using the outer product,

$$D(\tau, t) = G(t-\tau) \otimes E(t). \tag{3.23}$$

This last expression already represents the FROG signal in time domain, and does not need any row shift nor column permutation. The FROG trace, I_{FROG}, naturally follows by performing a Fourier transform and taking its absolute squared value

$$I_{FROG}(\tau, \omega) = \left|\mathcal{F}\left\{D(\tau, t)\right\}\right|^2. \tag{3.24}$$

The outcome of this approach can be seen in Figure 3.18.

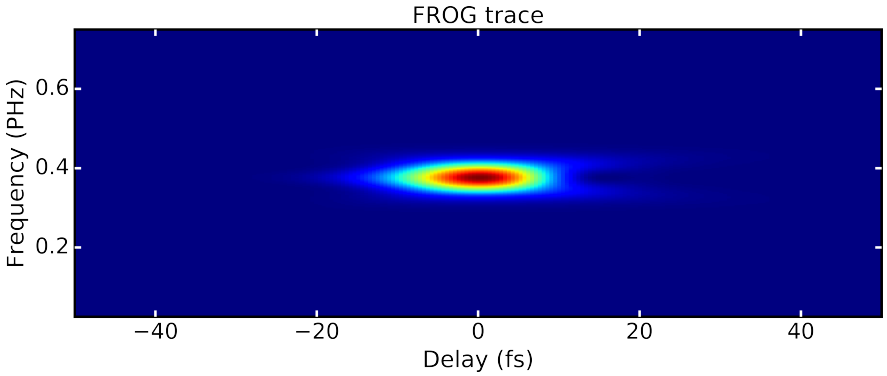

Figure 3.18: Simulated PG-FROG trace (210×256 points) by d-scan method, using the same pulse in Figure 3.16.

This kind of representation has its advantages, as the trace can be better sampled than in the case in Figure 3.16d, i.e., for similarly sized windows, the trace makes a better use of the number of points available. The phase of the pulse can now be retrieved, just like in d-scan, i.e., obtaining the amplitude of the electric field, $\left|\tilde{E}(\omega)\right|$, from the fundamental spectrum, and guessing the spectral phase that minimizes the rms error between measured and simulated trace. This d-scan-inspired method for FROG retrieval gives us, for instance, the ability to reconstruct a pulse with incomplete traces, which is not possible using any standard FROG approaches.

3.6.4 FROG ambiguities

The most common FROG method is the SHG-based one, as it is the simplest in terms of setup. However, because of the symmetry of the FROG trace with respect to delay, one encounters a phase ambiguity while doing the retrievals, i.e., the retrieved phase, $\varphi_{ret}(\omega)$, can have either of two outcomes:

$$\varphi_{ret}(\omega) \rightarrow \begin{cases} \varphi(\omega) \\ -\varphi(\omega) \end{cases} \tag{3.25}$$

In case the sign of the retrieved phase is reversed, $-\varphi(\omega)$, then the retrieved electric field becomes $\tilde{E}(\omega) = \left|\tilde{E}(\omega)\right| exp(i\varphi) = \left|\tilde{E}(\omega)\right| exp(-i\varphi_{ret}) = \tilde{E}^*(\omega)$. Fourier transforming this last expression, we get, $E^*(-t)$, which means that the same SHG-FROG trace can be generated by either $E(t)$ or $E^*(-t)$. This presents a problem to the determination of the electric field of a pulse, since no additional information can be extracted just from

the pulse spectrum and trace.

There are, though, methods to lift this ambiguity [98, 99], but these approaches add to the complexity of the FROG setup and/or require additional measurements, or expensive components such as an acousto-optic programmable dispersive filter (AOPDF). In contrast, d-scan doesn't have any known ambiguity, even in its SHG variant.

3.7 Recent developments

The d-scan technique does not limit itself to the SHG effect, as new d-scan types based on higher-order nonlinearities were recently reported such as the ones based on third-harmonic generation (THG) [100, 101], on cross-polarized-wave generation (XPW) [102, 103], as well as on self-diffraction (SD) [104] that is reported in chapter 4 of this thesis. Besides the conventional retrieval algorithm, new algorithms were devised to improve the retrieval speed [80] and resilience to noise [105] . More recently, d-scan measurements of near single-cycle [106] and single-cycle pulses [83] were reported.

3.8 Conclusions

The dispersion scan technique has several desirable features for ultrashort pulse characterization, namely, a simple and robust setup devoid of beamsplitting and delays, a superior sensitivity to few-cycle regime, no known ambiguities and redundancy, out of the box, since its inception. In the next chapters these characteristics will allow for extending the d-scan technique to other spectral ranges, such as the UV, and apply it to the temporal characterization of novel sources of ultrashort pulses.

4 Self-diffraction (SD) d-scan

In chapter 3 we briefly described the dispersion scan technique based on second-harmonic generation (SHG), and mentioned other works based on third-harmonic generation (THG) and cross-polarized wave generation (XPW). A remarkable feat of generation and characterization of a near single-cycle (1.04 cycles) pulse using SHG d-scan was recently achieved [83]. However, the SHG d-scan may not be a suitable technique for the characterization of ultrashort UV pulses, not because of the concept itself but due to the actual implementation requirements, i.e., the lack of a frequency-doubling crystal that works in the UV coupled with a good transparency range. Even assuming the existence of such a frequency-doubling crystal, for a UV range of, e.g., 200 to 400 nm, the generated radiation from the upshifted frequencies would be absorbed in air, hence any pulse measurement setup would have to be implemented inside vacuum chambers.

It is thus necessary, for the characterization of UV pulses, that we manage to generate a nonlinear optical signal from the UV that remains in the same wavelength region, allowing us to keep the d-scan setup simple. One such effect is the third-order nonlinear optical effect of self-diffraction (SD).

In this chapter we will explore a d-scan method based on the self-diffraction. A comparative study between the SHG and SD d-scan is done, for the experimental validation of this new d-scan implementation, using pulses from our homemade hollow-core fiber compressor. This new variant of the d-scan technique also enables us to measure ultrashort UV pulses, as described in chapter 6.

The author would like to acknowledge the help of Francisco Silva, PhD., for providing the barebones Fourier-based SHG d-scan pulse retrieval code, on which the rest of the work was based. Part of this work was published in [104].

4.1 Limitations for ultrabroadband SHG generation

The Beta Barium Borate (BBO, β-BaB2O4) crystal is commonly used for the frequency-doubling of laser pulses, most commonly generated by Ti:Sapphire lasers. This negative uniaxial crystal is characterized by two parameters, namely, its thickness, L, and az-

imuthal angle, θ, i.e., the angle between the crystal surface and the optical axis. Its Sellmeier equations are [25],

$$\begin{cases} n_e^2 = & 2.3753 + \frac{0.01224}{\lambda^2 - 0.01667} - 0.01516\lambda^2 \\ n_o^2 = & 2.7359 + \frac{0.01878}{\lambda^2 - 0.01822} - 0.01354\lambda^2 \end{cases}, \tag{4.1}$$

where λ is expressed in μm, n_o and n_e are the ordinary and extraordinary refractive indices respectively. With these equations, one can calculate the phase-mismatch, $\Delta k(\omega, \theta)$ (where θ is the angle between the propagation direction and the crystal optical axis), as well as the SHG process efficiency, which is proportional to $\propto L^2 sinc^2\left(\frac{\Delta k}{2}L\right)$. Figure 4.1 (where the curves are calculated according to $sinc^2\left(\frac{\Delta k}{2}L\right)$ and $\Delta k(\omega, \theta) = k(\theta, 2\omega) - 2k(\omega)$) shows the efficiency of BBO type-I SHG phase-matching curves for two different crystal thicknesses, namely $50\,\mu m$ and $5\,\mu m$, with an angle of $\theta = 29.2°$ (optimized for the SHG around 800 nm). It is clear from Fig. 4.1 that the reduction of crystal thickness increases the frequency-doubling bandwidth, which is ideal for very broadband pulses encompassing wavelengths starting from the mid-visible range to the near-infrared region. However, this invariably reduces the efficiency of the process, due to the dependence on L^2. The normalized efficiencies are calculated according to $sinc^2\left(\frac{\Delta k}{2}L\right)$.

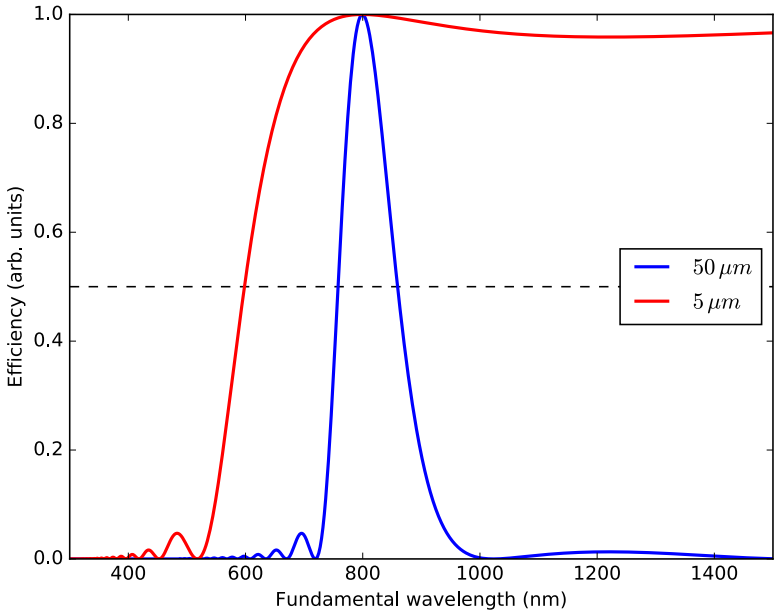

Figure 4.1: BBO type-I SHG normalized efficiency at different crystal thickness, $\theta = 29.2°$.

Taking into account that the transparency range of the BBO crystal ranges from 190 nm - 3500 nm, one would expect to be able to measure second-harmonic signals from ultrashort pulses with wavelengths down to ~380 nm, in the ultraviolet range.

Unfortunately, the measurement of pulses centered in the region from 400 nm - 600 nm suffer from a narrower frequency-doubling bandwidth compared to mid-IR pulses, even when using very thin (5 μm) BBO crystals) as shown in Fig. 4.2

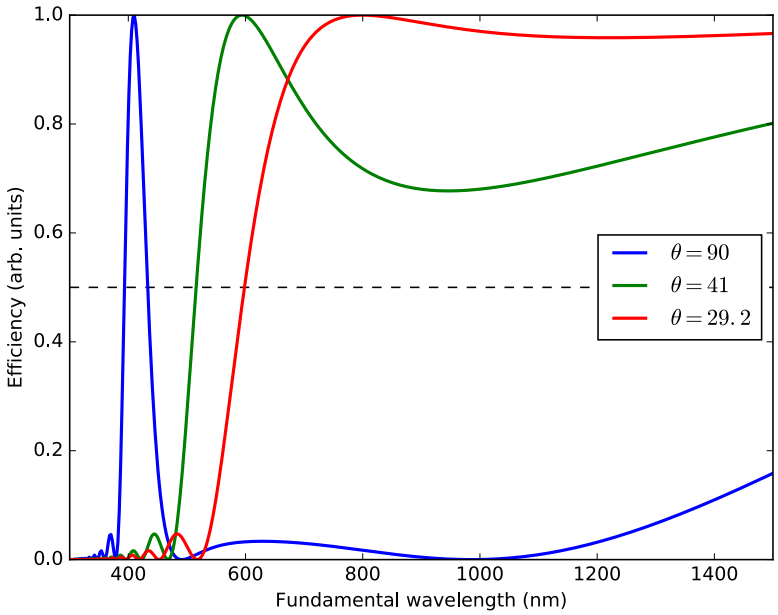

Figure 4.2: BBO type-I SHG efficiency at $L = 5\,\mu m$, at different values of the azimuthal angle, θ. The maximum efficiency wavelength are 800 nm @ $\theta = 29.2°$, 600 nm @ $\theta = 41°$ and 410 nm @ $\theta = 90°$.

This observation can be better understood by looking at Fig. 4.3, which is the plot of the values of θ that minimize the phase-mismatch for a given wavelength. We see that in the regions where the slope is smaller, it enables a reasonable phase-matching along a wide range of wavelengths, thus increasing the frequency-doubling bandwidth. On the other hand, regions with a high slope steepness will hinder phase-matching over a broad range of wavelengths and lead to a narrowing of the frequency-doubling bandwidth.

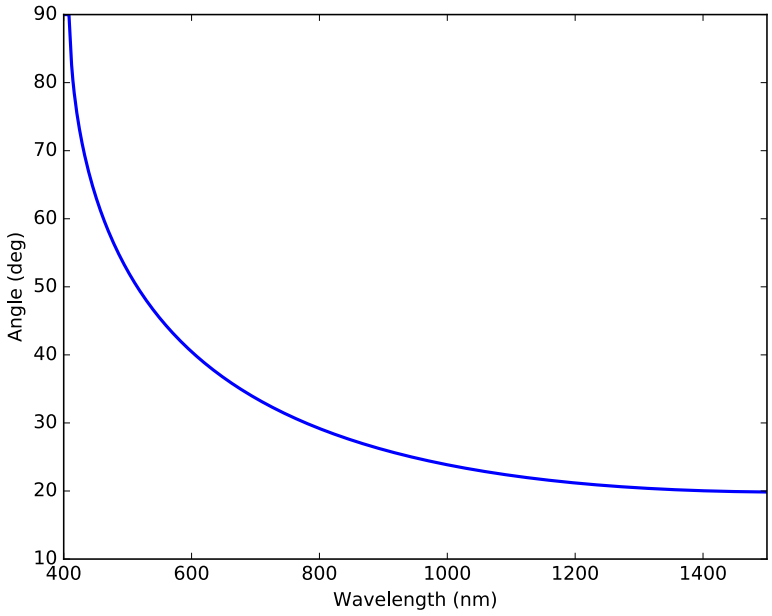

Figure 4.3: BBO type-I SHG phase-matching curve.

Conceptually, a narrower phase-matching bandwidth is not so restrictive in the case of the dispersion-scan technique since it will only influence the response function, and the spectral phase would still be able to be retrieved as seen in [79], though in less favorable conditions. Nevertheless, when faced with broadband pulses centered around 400 nm (at the threshold of visible light) or even other central wavelengths in the ultraviolet and/or deep ultraviolet (DUV), the need for other type of pulse measurement is evident.

4.2 Higher-order nonlinear optical effects

The SHG-based dispersion scan was shown to be not only simple in its experimental implementation but robust as well, enabling the measurement of ultrashort pulses down to near single-cycle and single-cycle [83, 107], using off-the-shelf components. Despite this success, SHG d-scan is still limited, like all other SHG based methods, to the measurement of pulses in the visible to mid-infrared (VIS-MIR) region, as the commonly used SHG crystals (e.g., BBO) are not able to convert wavelengths in the UV region adequately. In order to circumvent this limitation higher-order optical nonlinearities are used. As seen in the introduction, nonlinear optical effects can be described by the Taylor expansion of the material polarization [24] P,

$$P_i = \epsilon_0 \left(\sum_j \chi_{ij}^{(1)} E_j + \sum_{jk} \chi_{ij}^{(2)} E_j E_k + \sum_{jkl} \chi_{ijkl}^{(3)} E_j E_k E_l + c.c + \dots \right), \qquad (i,j,k,l = x,y,z). \tag{4.2}$$

The expression responsible for third-order nonlinearities is

$$P_i^{(3)} = \epsilon_0 \sum_{jkl} \chi_{ijkl}^{(3)} E_j E_k E_l, \qquad (i,j,k,l = x,y,z). \tag{4.3}$$

Equation 4.3 models the interaction of up to three, not necessarily distinct, electric fields, producing a fourth wave. Effects such as third-harmonic generation (THG) [101], and cross-polarized wave generation (XPW) [102] have recently been used in the implementation of new dispersion scan variants. We will move on to the exploration of other higher-order nonlinear effects, as THG is unsuitable for the measurement of UV pulses and XPW is limited to the choice and availability of polarization optical components, as the XPW effect generates a signal in the same wavelength region of the fundamental beam and requires a careful separation of the polarization components (fundamental and nonlinear signal have orthogonal polarization). Taking inspiration from SD-FROG, we started envisioning a SD implementation of the dispersion scan technique.

In the self-diffraction geometry, two beams are made to interact at a given angle (see Fig. 4.4), inside a transparent medium, e.g., a fused silica slide. The electric field of the beam emerging from the slide due to self-diffraction, E_{SD}, is described by an interaction involving $\chi^{(3)}(\omega;\omega,\omega,-\omega)$ and can be written as follows,

$$E_{SD}(t) \propto |E(t)|^2 E(t) = E(t)E(t)^* E(t). \tag{4.4}$$

One can see from Eq. 4.4, that the resulting electric field, E_{SD}, apart from the modulation imposed by the pulse intensity, $I \propto |E(t)|^2$, is proportional to the original electric field $E(t)$. This means that the wavelength range of the resulting beam should be within the same range of wavelengths as the original beam. As a drawback, the measured nonlinear signal may be contaminated with the fundamental spectrum, since the generated nonlinear spectrum and the fundamental spectrum share the same range of wavelengths. Fortunately, since the d-scan property of redundancy is valid regardless of the type of optical nonlinearity, if we implement a SD-based dispersion scan technique, we can, if need be, crop the regions of a d-scan trace, while still being able to retrieve the pulse under test.

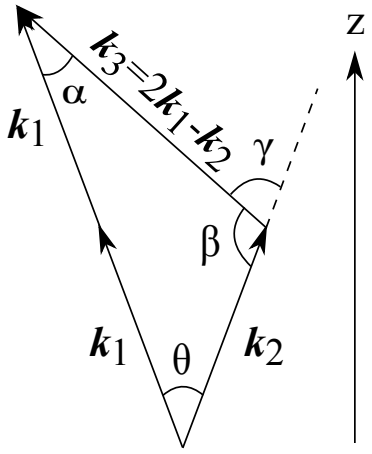

Figure 4.4: SD interaction geometry.

4.3 SD d-scan simulations

Knowing the expression for the SD effect (Eq. 4.4), we are able to generate SD d-scan traces and study how they are affected by different spectral phases. We will consider $E(t,z)$ as the expression for the electric field of the pulse under test, after traversing an amount of glass insertion represented by z

$$E(t,z) = \int_{-\infty}^{+\infty} \tilde{E}(\Omega) e^{-izk(\Omega)} e^{i\Omega t} d\Omega. \tag{4.5}$$

Using Eq. 4.4, we arrive at the expression of the electric field generated by the self-diffraction effect,

$$E_{SD}(t,z) \propto |E(t,z)|^2 E(t,z). \tag{4.6}$$

The expression for the simulated trace is similar to Eq. 3.5 ,

$$S_{simul}(\omega,z) = \left| \int_{-\infty}^{+\infty} E_{SD}(t,z) e^{-i\omega t} dt \right|^2. \tag{4.7}$$

Fig. 4.5 shows the effect of different spectral phases applied to a gaussian pulse. The simulations are made using a sech-squared pulse centered at 800 nm, capable of supporting a TL 4 fs pulse. Each trace has a different phase $\varphi(\omega)$, namely, a flat phase, a phase with GDD of 30 fs^2, a TOD of 60 fs^3, and a FOD of 350 fs^4.

In the first case (Figure 4.5a), the SD d-scan trace for a transform-limited pulse ($\varphi(\omega) = 0$) is symmetrical along the zero insertion axis, in this case the only dispersion

being varied is the one contributed by the wedge pair, $\varphi_{wedges}(\omega) = zk(\omega)$, i.e., in this case, φ_{wedges} is the only term that contributes to the total phase $\Phi(\omega, z) = \varphi(\omega) + zk(\omega)$.

Pulses affected by pure GDD (4.5b) show a bulk shift along the insertion axis, as it is expected that pulses with positive chirp need less glass insertion to arrive at the optimum compression position. The slight tilt of the trace is due to higher-order dispersion of the glass wedge pair.

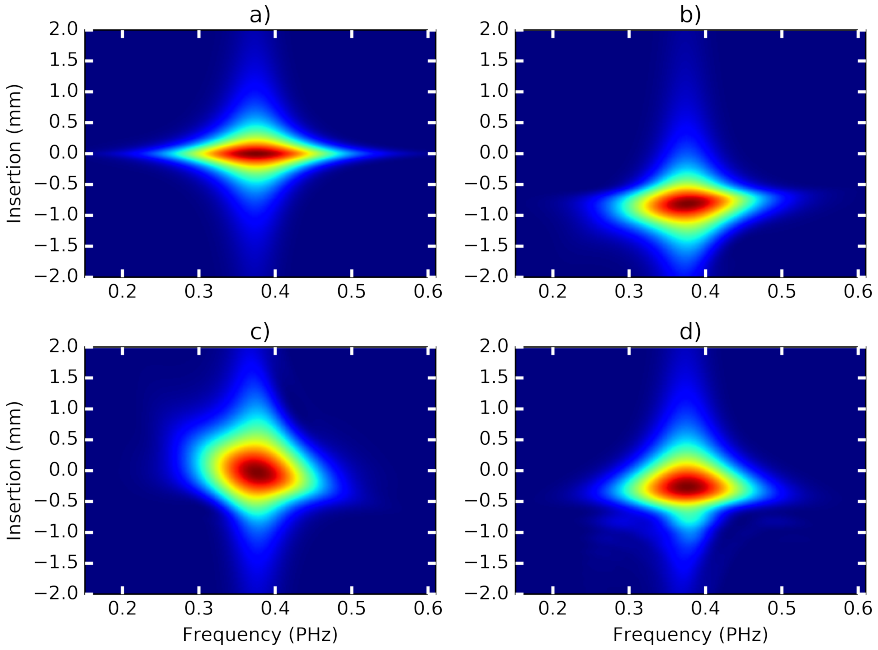

Figure 4.5: Examples of simulated SD-scan traces. a) Transform-limited; b) with group-delay dispersion (30 fs^2); c) with third-order dispersion (100 fs^3); d) with fourth-order dispersion (350 fs^4).

When a pulse is affected by TOD (i.e., cubic phase) (4.5c), the second derivative of the phase is a linear function of frequency, which translates into a trace where different, adjacent frequencies get compensated at different values of glass insertion. Overall, the behavior of the SD d-scan traces resembles the behavior of the SHG traces shown previously in Figure. 3.3, chapter 3.

Simulations are very helpful for conceptual and illustrative purposes, but given that spectra are easy to measure in the lab, we can improve upon the simulations by using a real, measured spectrum from the light source we wish to characterize, i.e., our home-made hollow-core fiber (Fig. 4.6).

The simulated SD dscan traces calculated from the spectrum of our hollow-core fiber

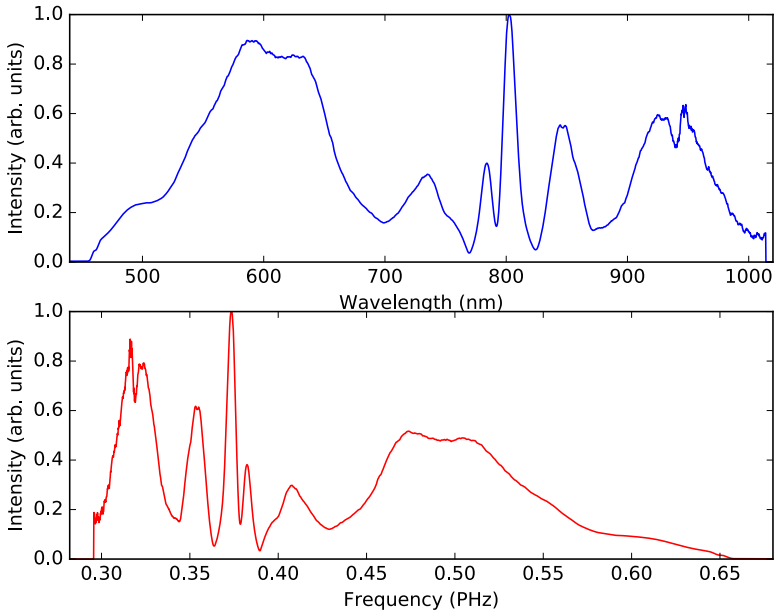

Figure 4.6: HCF spectrum, in the wavelength (top) and frequency (bottom) domains.

assuming different phases are shown in Figure 4.7.

4.4 SD setup and measurements

The SD d-scan setup scheme is very similar to the SHG d-scan setup, as shown in Figure 4.8. The beam from the HCF passes through the pair of wedges and onto a set of chirped mirrors (Ultrafast Innovations, PC70) where it undergoes 16 bounces. After the compressor, the beam is expanded by a factor of 4 with a beam expander (Thorlabs, BE04R/M; not shown in the scheme). The beam expansion is required to ensure that in a subsequent spatial selection done with a mask with two slits (width: 2 mm, separated by 2 mm), cf. Figure 4.8), the emerging beams are spectrally homogeneous. As the beam passes through the mask it creates the two beam replicas necessary for the self-diffraction effect. A spherical mirror ($f = 250$ mm) focuses both beams (external interaction angle, $\theta_{ext} = 1.4º$) into a fused silica slide (30 μm thick) where the SD interaction takes place, generating two additional beams (the SD beams/fields) that are spatially separated from the two input beams. Unlike BBO crystals which are non-centrosymmetric [108], hence capable of nonlinear optical effects of second-order, ($\chi^{(2)}$), fused silica is non-centrosymmetric and so, no second-order nonlinear optical interaction will occur in

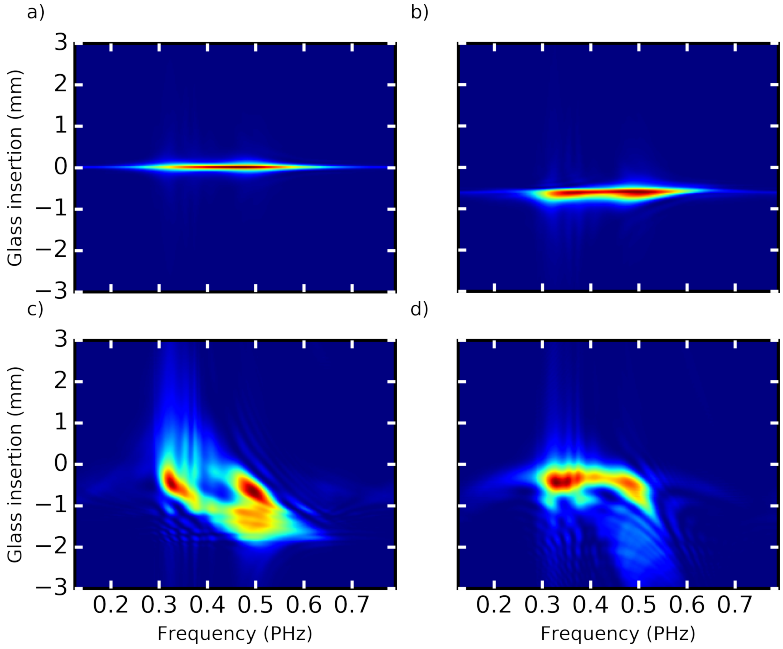

Figure 4.7: Examples of simulated SD-scan traces using the spectrum from the HCF. a) Transform-limited; b) with group-delay dispersion (30 fs^2); c) with third-order dispersion (100 fs^3); d) with fourth-order dispersion (350 fs^4).

fused silica, which means that the lowest nonlinear optical effect will be of third-order, $\chi^{(3)}$. The resulting generated beam is then coupled into a fiber by a lens. A fixed number of spectra from the one of the SD generated fields are recorded as a function of the glass insertion and with these recorded data, we are able to plot the measured trace.

A SHG d-scan setup is implemented as well by changing the slide in the setup by a BBO crystal, enabling us to make comparisons on the pulse retrieval for both variants of d-scan. The spectra in all the SD traces were measured by an intensity calibrated spectrometer. Both measured SD d-scan and SHG d-scan traces are shown in Figure 4.9. As we are dealing with a degenerate self-diffraction process, where the generated nonlinear frequencies lie in the same range of frequencies of the input beams ($\omega_{NL} = \omega + \omega - \omega$), one could at first expect the SD signal to cover the whole spectral range of the input pulse. Instead, the SD d-scan trace only extends from 450 to 800 nm (Figure 4.9), since the efficiency of this process is wavelength-dependent (i.e., it is proportional to $\omega^2 \propto \lambda^{-2}$), as shown at the end of the chapter in section 4.4.5.

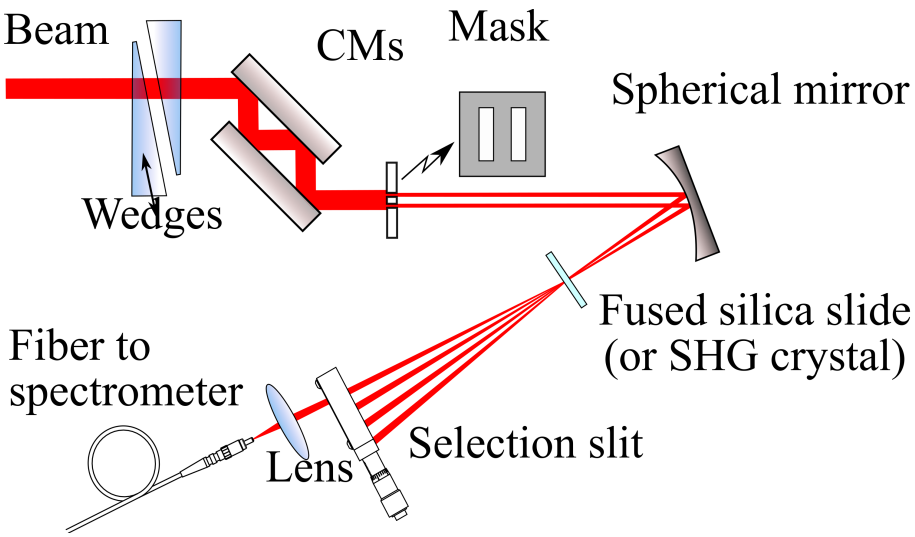

Figure 4.8: SD dscan setup. See text for details.

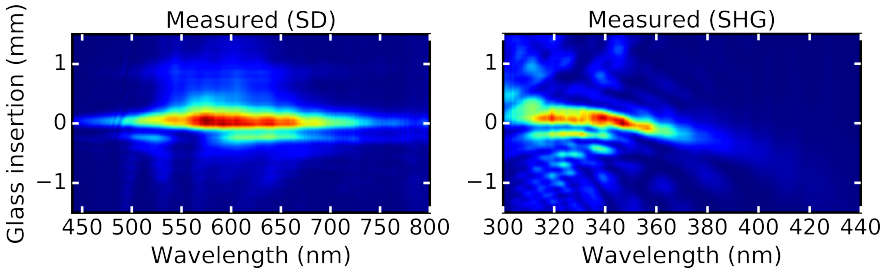

Figure 4.9: Traces obtained from a) the SD d-scan setup and b) the SHG d-scan setup.

4.4.1 Phase retrieval strategies

In the following we will consider some phase retrieval strategies, using SHG d-scan as an example, but the same reasoning carries over to the SD d-scan. The data is associated with measurements of pulses from our homemade hollow-core fiber (HCF).

We begin with the expression for the ideal d-scan trace as seen in chapter 3, subsection 3.1,

$$S(\omega, z) = \left| \int_{-\infty}^{+\infty} \left(\int_{-\infty}^{+\infty} \tilde{E}(\Omega) e^{-izk(\Omega)} e^{i\Omega t} d\Omega \right)^2 e^{-i\omega t} dt \right|^2, \tag{4.8}$$

where $\tilde{E}(\omega) = \left|\tilde{E}(\omega)\right| e^{-i\varphi(\omega)}$, is the expression of the field in the frequency domain and $\varphi(\omega)$ is its spectral phase. This equation can also be transformed into a spectral

convolution,

$$S(\omega, z) = \left| \int_{-\infty}^{+\infty} \tilde{E}(\Omega') e^{-izk(\Omega')} \tilde{E}(\omega - \Omega') e^{-izk(\omega - \Omega')} d\Omega' \right|^2 . \tag{4.9}$$

Since we have the acquired trace and the spectrum of the pulse we want to characterize, and know the equation to simulate a trace (Eq. 4.8), we can implement a mathematical optimization algorithm to reconstruct the spectral phase $\varphi(\omega)$. This spectral phase can be represented as Fourier or a Taylor polynomial, whose coefficients are obtained by the minimization algorithm (e.g., Nelder-Mead or the Broyden–Fletcher–Goldfarb–Shanno (BFGS) algorithm) that minimizes the rms error between the acquired trace and the generated trace (which is simulated trace multiplied by the response function, $R(\omega)$, as discussed in chapter 3). Alternatively, instead of guessing the coefficients of a Taylor/Fourier expansion, we can guess directly the values of the spectral phase in a point-by-point fashion (PBP) which will be described further in the text. Other more recent phase retrieval algorithms were already mentioned in chapter 3.

The first approach to retrieve the spectral phase was to use a finite Fourier polynomial as a fit [78], or simple polynomials. For not so strongly modulated phases, this approach usually is computationally fast since it will not require many polynomial/Fourier coefficients. Figure 4.10 shows the SD and SHG d-scan measured traces and retrieved traces, of our homemade hollow-core fiber, using a Fourier polynomial (64 Fourier coefficients) for the retrieval. It shows that, although the main patterns of the measured traces are reproduced in the retrieved traces, there is still room for improvement, i.e., even though there is a good visual agreement, we will see further in the text, that it is possible to obtain an even better visual agreement and lower d-scan error. This state of affairs does not improve by increasing the number of Fourier coefficients, which suggests that an alternative retrieval method should be sought.

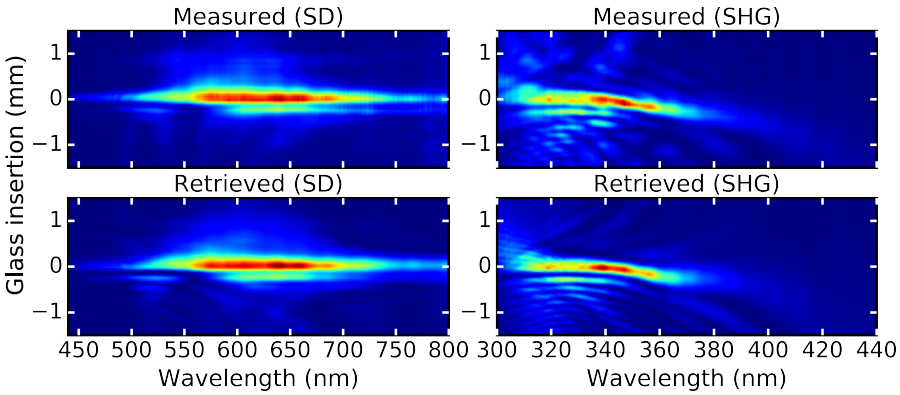

Figure 4.10: SD and SHG measured traces. Retrieved traces obtained by Fourier polynomial expansion of the spectral phase.

To further reenforce this point, Figure 4.11 shows the phases retrieved by SD and SHG d-scan using the Fourier polynomial with 64 coefficients. Both phases diverge around 500 nm, as this is expected from the PC70 mirrors, but the orientation of these divergences are symmetrical. One would expect the signal of the divergences to be the same for both retrieved phases, for consistency. The SD d-scan trace has an error of 0.013 for a grid size of 256x210, as for the SHG d-scan case, the error is 0.027 for a grid with the same size.

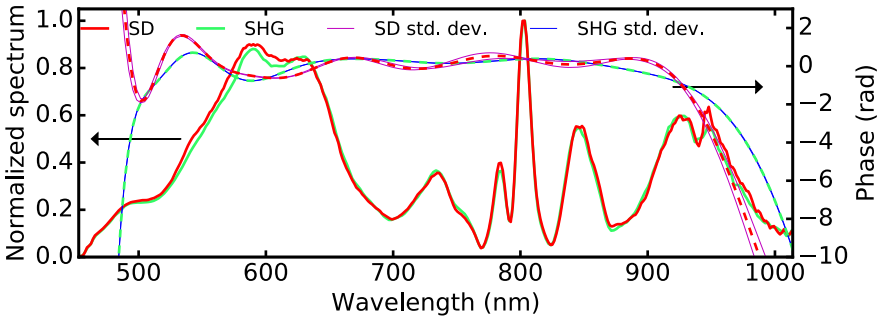

Figure 4.11: SD and SHG retrieved spectral phases using a Fourier polynomial expansion for the spectral phase.

Another approach for the representation of the spectral phase that yields better retrieved traces (but a more time consuming process, computationally wise) is the point-by-point method (PBP) whereas instead of trying to fit the spectral phase with a Fourier polynomial we let the minimization algorithm “choose” each individual value of ϕ for each value of frequency. The resulting retrieved phases of the PBP approach are shown in

Figure 4.12. The retrieved phases structure is more complex, compared to Figure 4.11, but the retrieved traces have a higher degree of resemblance to the measured traces (see Fig. 4.13). The retrieval strategy employed was the PBP, which yields retrieved traces in better agreement with the measured traces. SD d-scan trace has an error of 0.010 for a grid size of 256x210, as for the SHG d-scan case, the error is 0.013 for a grid with the same size. One striking difference between the phases retrieved by PBP and the phases retrieved using a Fourier polynomial representation is that in the case of PBP, the phases don't seem to diverge around 500 nm as should be expected, suggesting that a further processing of the retrieved phases is necessary.

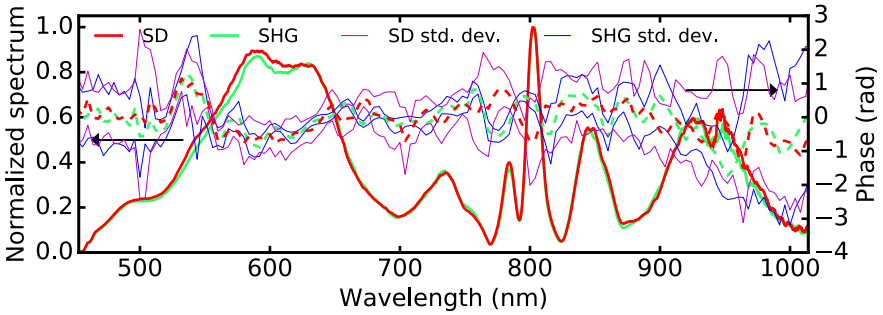

Figure 4.12: Phase retrieval by PBP.

4.4.2 Improving the retrieval process

The measured and retrieved traces using the PBP approach are depicted in Fig. 4.13.

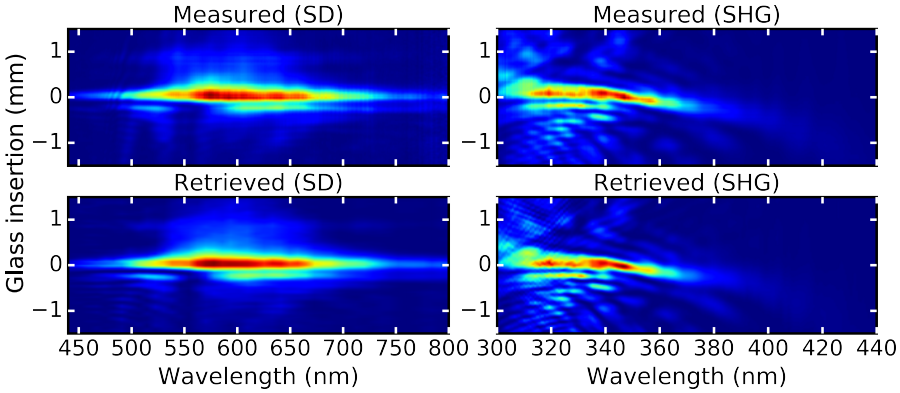

Figure 4.13: Left: SD d-scan measured and retrieved traces; right: SHG d-scan measured and retrieved traces.

This approach (PBP) improves upon the previously retrieved results shown in Figure 4.10 and Figure 4.11. There are though, some common pitfalls using the point by point (PBP) method. The minimization algorithm seems to retrieve a wrapped phase, as no retrieved spectral phases diverge around 500nm in Figure 4.12. We must keep in mind that the spectral phase is defined up to a phase that is a multiple of 2π, i.e., $\varphi(\omega) = \varphi_{ret}(\omega) + m \times 2\pi$, where m is an integer.

It turns out that, while allowing more flexibility to the algorithm, i.e., enabling it to choose the spectral phase for each point, the algorithm may tend to choose different values of m for each frequency. For the spectral phase to be consistent, it was found that an additional phase unwrapping was necessary. After the phase unwrapping is done, the retrieved phases look as in Fig. 4.14. We can now see that both spectral phases (SD and SHG) diverge around 500 nm and in the same downwards direction. This situation is more physically meaningful since this divergence was expected from the beginning.

The average phases and their standard deviations are shown in Figure 4.14. From this figure, we observe that the SD average phase follows the same trend as the SHG phase, including the already mentioned sharp divergence below 500 nm and the slow roll-off around 940 nm, and this is a good indicator of the viability of the SD d-scan for the measurement of ultrashort pulses.

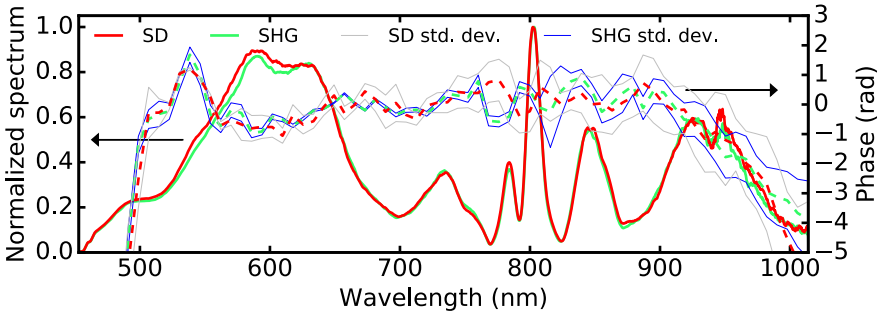

Figure 4.14: Spectra and retrieved spectral phases from SD and SHG dscan.

The temporal intensities obtained with the average spectral phases are shown in Fig. 4.15. Pulse durations were 3.7 ± 0.3 fs for SD and 3.8 ± 0.1 fs for SHG d-scan. The higher duration uncertainty in the SD d-scan trace is attributed to the lower sensitivity in a higher nonlinearity, i.e., the fact that the field generated by a third-order nonlinearity involves a double convolution, a mathematical operation that has an effect of “smoothing” out the spectra in a SD d-scan trace, hence resulting in a reduced sensitivity compared to SHG d-scan.

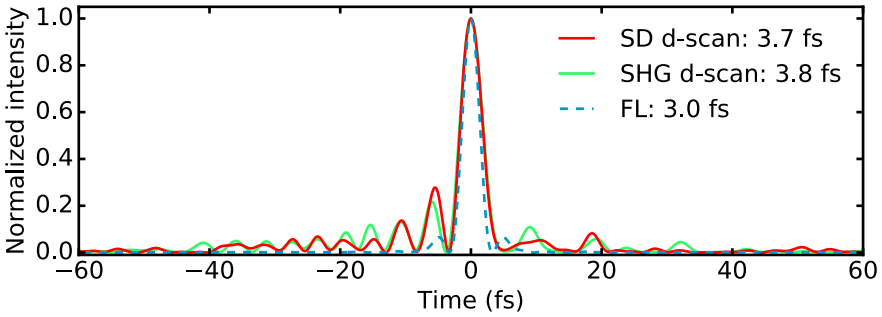

Figure 4.15: Intensities retrieved by SD- and SHG d-scan.

The good agreement of the SD and SHG retrieved spectral phases, leads to a similar good agreement in the (time domain) pulse shape. This is evident in the structure of pre-pulses preceding the main pulse, and to a lesser degree in the structure of post-pulses. A quantitative argument (besides the qualitative one, i.e., the visual agreement) for the good agreement between the retrieved phases can be put forward by using the comparison criteria stated in [81]. The knowledge of the electric fields of the pulses (via their spectra and phases), and given the fact that we are using the SHG pulse as reference, a root-mean-squared (rms) error, ϵ, can be defined,

$$\epsilon = \|E_1 - E_2\| = \left[\int_{-\infty}^{+\infty} |E_1(t) - E_2(t)|^2 \, dt\right]^{\frac{1}{2}} \tag{4.10}$$

$$= \left[\frac{1}{2\pi}\int_{-\infty}^{+\infty} \left|\tilde{E}_1(\omega) - \tilde{E}_2(\omega)\right|^2 d\omega\right]^{\frac{1}{2}}, \tag{4.11}$$

where $E_1 = E_{SHG}$, $E_2 = E_{SD}$ are the electric fields retrieved by SD and SHG d-scan, respectively, and the equality expressed by Eq. 4.11 is guaranteed by Parseval's theorem,

$$\|E\|^2 = \int_{-\infty}^{+\infty} |E(t)|^2 \, dt = \frac{1}{2\pi}\int_{-\infty}^{+\infty} \left|\tilde{E}(\omega)\right|^2 d\omega. \tag{4.12}$$

This error was computed both in time domain (Eq. 4.10) and in the frequency domain (Eq. 4.11), arriving at the value of 3.2486. By dividing this last value by the euclidean norm of the electric field, $\|E\|$, we get 0.047, accounting for $< 5\%$ of error between both electric fields. A similar reasoning can be used to assess, quantitatively, the divergence of the standard deviations with respect to the average SD retrieved phase. Let us assume for a moment, a worst case scenario, where the SD retrieved phase was either one of the

standard deviation phases instead of the actual average phase. Then, computing the rms error, we arrive at values $< 8\%$. Even though the std deviations can diverge by as much as $\sim 1.5\,rad$ from the average phase, comparing the $< 8\%$ with the <5% obtained using the average SD phase, we see that the error is slightly higher, but it is still single digit, which is acceptable in our view.

4.4.3 Response function

As previously discussed in chapter 3, pulse retrieval with the d-scan technique does not require the traces to be calibrated (intensity calibration).

For the sole purpose of pulse retrieval, the knowledge of the response function is unnecessary, as it is a byproduct of the retrieval algorithm. Nevertheless, the spectra in the measured SD traces were recorded with an intensity calibrated spectrometer, so that we can compare the obtained response function with the one that was derived using a simple theoretical model (see subsection 4.4.5). The measurements taken with an intensity calibrated spectrometer allow us to exclude the spectrometer's spectral response.

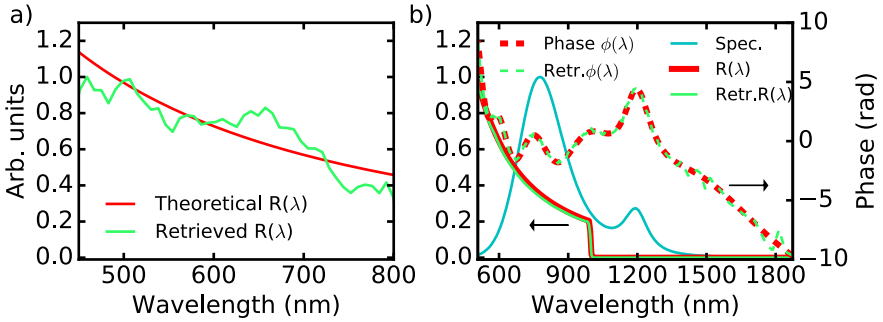

Figure 4.16: a) Theoretical and retrieved SD response function. b) Simulation of multi-octave pulse retrieval.

The simple theoretical model for the response function (cf. 4.4.5), $R(\omega)$, is given by

$$R(\Omega) = \frac{\Omega^2}{n(\Omega)} \left[n^2(\Omega) - 1\right]^8 sinc^2 \left\{\Delta k_z(\Omega)\frac{L}{2}\right\}, \tag{4.13}$$

and it is shown in Figure 4.16a, along with the retrieved response function.

As the response function is defined up to a constant factor, it was decided to multiply the theoretical response by a constant such that it reduces the root-mean-square distance between the retrieved and the theoretical response. The difference between theoretical and retrieved response can be attributed to the simplicity of the model (which is based

in several approximations) and the existence of spatial chirp in the generated nonlinear signal, leading to coupling effects in the spectrometer fiber, which translates into a altered response function. In the presence of the spatial chirp, it was opted to make the coupling to the spectrometer fiber with the criteria of achieving the highest and broadest nonlinear spectrum.

4.4.4 Multi-octave simulation

To show the capabilities of the technique, the retrieval of pulses with multi-octave spanning spectra was investigated numerically. A spectrum centered at 800 nm, able to support a TL pulse of 2.7 fs is shown in Figure 4.16b. Along with it, a spectral phase comprised of TOD with added ringing and a peak at 1200 nm. A (theoretical) response function was imposed in the trace, with an external interaction angle of $\theta_{ext} = 1.4º$ and slide thickness of $L = 30\,\mu m$, and an additional cutoff at 1000 nm to model the detection range sensitivity of common silicon detectors in spectrometers. Furthermore, an additional -30 dB of gaussian noise baseline was added to the trace to simulate analogous conditions when measuring experimental traces.

It was shown that the retrieval process was successful, where the retrieved phase agrees fairly well with the simulated one, over the 500 nm to 1900 nm (which is nearly 3 octaves), and the retrieved response function follows faithfully the imposed response function.

4.4.5 Derivation of the SD response function

In this section we will derive a simple model of the SD response function, similar to the derivations done in [48]. We will a non-depletion regime of the input electric field, i.e., the input electric fields remain undisturbed along the propagation.

Self-diffraction can be viewed as an interaction between two photons at ω_1 and one at ω_2, resulting in a frequency, Ω, given by

$$\Omega = 2\omega_1 - \omega_2. \tag{4.14}$$

Normally, $\omega_1$and ω_2 are independent frequencies that characterize the process, but since the quantity of interest is Ω, we will adopt another pair of independent variables, Ω, and ω_1, naturally, ω_2 will be given by $\omega_2 = 2\omega_1 - \Omega$.

The main objective is to obtain expressions of $\chi^{(3)}$ and Δk_z (the phase-mismatch component along the propagation axis, i.e., the z-axis) as functions of the sole variable

Ω, under reasonable approximations. After obtaining the expressions we'll see how they will be combined.

From [23], we see that it is possible to express the third-order susceptibility, $\chi^{(3)}$, as a quantity that is proportional to the product of several linear susceptibilities, $\chi^{(1)}$

$$\chi^{(3)}(\Omega,\omega_1,\omega_1,-\omega_2) \propto \chi^{(1)}(\Omega)\left[\chi^{(1)}(\omega_1)\right]^2\chi^{(1)}(\Omega-2\omega_1), \tag{4.15}$$

where $\chi^{(1)}(\Omega) = n^2(\Omega) - 1$, $\chi^{(1)}(\Omega - 2\omega_1) = \chi^{*(1)}(2\omega_1 - \Omega)$ and for lossless materials, $\chi^{*(1)}(\omega_2) = \chi^{(1)}(\omega_2)$. For frequencies ω_1 and ω_2 near Ω, we get,

$$\chi^{(3)}(\Omega,\omega_1,\omega_{1,}-\omega_2) \approx \chi^{(3)}(\Omega,\Omega,\Omega,\Omega) = \left[\chi^{(1)}(\Omega)\right]^4 = \left[n^2(\Omega)-1\right]^4. \tag{4.16}$$

Now, for the calculation of the phase-mismatch along the z-axis, Δk_z,

$$\Delta k_z(\Omega,\omega_1) = 2k_{1z}(\omega_1) - k_{2z}(2\omega_1-\Omega) - k_{3z}(\Omega), \tag{4.17}$$

where k_{1z}, k_{2z} and k_{3z} are the projections of the incident and SD generated wavevectors, respectively, along the propagation axis (cf. Figure. 4.4).

The expansion of the k vectors in Taylor series around Ω yields

$$k_{1z}(\omega_1) \approx k_{1z}(\Omega) + \frac{dk_{1z}}{d\omega_1}(\omega_1-\Omega), \tag{4.18}$$

$$k_{2z}(2\omega_1-\Omega) \approx k_{2z}(\Omega) + 2\frac{dk_{2z}}{d\omega_1}(\omega_1-\Omega). \tag{4.19}$$

Substituting these two last equations in Eq. (4.17), we see that the terms containing derivatives cancel each other, so this approximation is valid up to corrections of 2nd order.

We will now derive the projection angle of $\mathbf{k_3} = 2\mathbf{k_1} - \mathbf{k_2}$ (bold letters represent vectors) onto the z-axis.

First, we want to calculate the angle γ. We assume $k_1 = k_2 = k$. By the law of sines

$$\frac{sin(\alpha)}{k} = \frac{sin(\beta)}{2k}, \tag{4.20}$$

since $\gamma = \pi - \beta$,

$$\frac{sin(\alpha)}{k} = \frac{sin(\pi-\gamma)}{2k} = \frac{sin(\gamma)}{2k}. \tag{4.21}$$

Applying the law of sines again to relate γ and θ, we get,

$$\frac{sin(\gamma)}{2k} = \frac{sin(\theta)}{k\sqrt{5-4cos(\theta)}}, \tag{4.22}$$

where $k\sqrt{5-4cos(\theta)}$ is the magnitude of $\mathbf{k_3} = 2\mathbf{k_1} - \mathbf{k_2}$, given by the law of cosines. Knowing that $\theta \ll 1$, $cos(\theta) \approx 1$, the last equation can be further simplified,

$$sin(\gamma) = 2sin(\theta), \tag{4.23}$$

and thus, remembering that $\theta \ll 1$ and the Taylor expansion (up to first order) of the sine, we get,

$$\gamma \approx 2\theta, \tag{4.24}$$

Hence, the projection angle of $\vec{k}_3$ along z, is $\frac{3}{2}\theta$. The phase-mismatch can then be written as,

$$\Delta k_z(\Omega) = k(\Omega) \times cos(\theta/2) - k \times cos(3\theta/2) \approx \theta^2 k(\Omega). \tag{4.25}$$

The electric field of a generic third-order process after propagating along a distance L, is given by [48],

$$\tilde{E}(L,\Omega) = i\frac{c\mu_0\Omega}{2n(\Omega)}\int_0^L \tilde{P^{(3)}}(z,\Omega)e^{-ik_{3z}(\Omega)z}dz, \tag{4.26}$$

where μ_0 is the vacuum permeability, $\tilde{\mathcal{P}}^{(3)}$, third-order nonlinear polarization, $n(\Omega)$ is the refractive index calculated at the generated frequency. In our case, $\tilde{\mathcal{P}}^{(3)}$, is given by

$$\begin{aligned}\tilde{P}^{(3)}(z,\Omega) = \iint \chi^{(3)}\tilde{E}_1(z,\omega_1)\tilde{E}_1(z,\Omega-\omega_1+\omega_2)\tilde{E}_2^* \\ \times\tilde{E}_2^*(z,\omega_2)e^{-i[k_{1z}(\omega_1)+k_{1z}(\Omega-\omega_1+\omega_2)-k_{2z}(\omega_2)]z}d\omega_1 d\omega_2\end{aligned} \tag{4.27}$$

where $\tilde{E}_1$ and $\tilde{E}_2$ are the fields associated with $\vec{k}_1$ and $\vec{k}_2$. Substituting Eq. (4.27) into Eq. (4.26) and integrating along z, we get,

$$\begin{aligned}\tilde{E}(L,\Omega) = i\frac{c\mu_0\Omega}{2n(\Omega)}\iint \chi^{(3)}\tilde{E}_1(\omega_1)\tilde{E}_1(\Omega-\omega_1+\omega_2)\tilde{E}_2^*(\omega_2)sinc\left(\Delta k_z\frac{L}{2}\right) \\ \times exp\left(i\Delta k_z\frac{L}{2}\right)d\omega_1 d\omega_2.\end{aligned} \tag{4.28}$$

Since we know that Δk_z and $\chi^{(3)}$ can be approximated by functions of one variable Ω which plays no role in the integral of eq. (4.28), the terms containing these quantities can be removed from the integral. Knowing that the spectral intensity is $S_{meas} \propto n\,|E|^2$, Eq. 4.28, can be recast as,

$$S_{meas} \propto \frac{\Omega^2}{n(\Omega)}\left[n^2(\Omega)-1\right]^8 sinc^2\left\{\Delta k_z(\Omega)\frac{L}{2}\right\} \times S_{ideal}, \tag{4.29}$$

where the ideal nonlinear SD spectral intensity, S_{ideal}, is defined as,

$$S_{ideal} \propto \left|\iint \tilde{E}_1(\omega_1)\tilde{E}_1(\Omega-\omega_1+\omega_2)\tilde{E}_2^*(\omega_2)d\omega_1 d\omega_2\right|^2. \tag{4.30}$$

Thus, the spectral filter/response function can be written as

$$R(\Omega) = \frac{\Omega^2}{n(\Omega)}\left[n^2(\Omega)-1\right]^8 sinc^2\left\{\Delta k_z(\Omega)\frac{L}{2}\right\}.$$

4.5 Conclusions

We developed a new variant of the dispersion scan technique, based on the self-diffraction effect and used it to characterize ultrashort pulses from our homemade HCF. The results obtained are in good agreement with a similar characterization of the same light source using the SHG d-scan. A simple model for the response function was derived, and the ability to use this technique in the case of multi-octave pulses was explored numerically. This new variant extends the d-scan technique to the UV range of wavelengths. Ultrashort pulses in the UV are characterized by SD d-scan in chapter 6.

5 Multiplate Continuum

This chapter describes the temporal and spatial characterization of high-energy ultra-broad laser pulses produced by a multiplate continuum (MPC) process, solid media based supercontinuum generation process. Before discussing the MPC concept we will begin with a brief review of high-energy supercontinuum generation in the most closely-related system, the hollow-core fibers (HCF).

For a complete comprehension of the supercontinuum light source see [109].

5.1 Supercontinuum generation (SCG)

The introduction of the titanium-sapphire laser in the 80s [110], ushered a new era in the field of nonlinear and ultrafast optics due to its solid state nature (in contrast with dye lasers) and its broadband fluorescence. As the technology around it matured, it proved to be an ideal source of ultrashort pulses, becoming a 'workhorse' in many labs around the world. Nowadays, sub-6 fs (250~300 nm bandwidth) are routinely achieved by some commercially available Ti:sapphire laser oscillators, enabled by the Kerr-lens modelocking.

Pulses from these laser oscillators, with energy in the order of a few nJ, can be further amplified by several orders of magnitude (e.g. ~10^6) when passing through a Ti:sapphire laser amplifier, commonly reaching mJ levels. However, pulse amplification has its own shortcomings, namely, the effect of gain narrowing which shortens the bandwidth of the amplified pulse. Thus, even though intracavity pulse amplification is able to increase the energy of the pulse, it has a negative effect on pulse bandwidth (typical amplifier duration is ~30 fs) due to gain narrowing. In order to reach shorter pulse durations and avoid the gain narrowing, external pulse compression methods were sought out.

Extracavity pulse compression was first implemented using a hollow fused silica waveguide or hollow-core fiber (HCF) [111], reaching pulse durations of 10 fs at 240 μJ from an input pulse of 140 fs at 660 μJ. In this scheme, pulses from an amplifier are coupled into a HCF, using a suitable focusing lens to obtain a waist comparable in size to the fiber diameter. The pulse will undergo a process of self-phase modulation (SPM) which will broaden its spectrum. The hollow-core fiber has the role of waveguiding the injected

beam as it propagates and undergoes self-phase modulation (SPM) due to the nonlinear index of the gas inside the fiber, producing a Bessel mode at the output of the HCF with high beam quality. The hollow-core fiber technique has matured over the years, with shorter pulse durations being reported, and single-cycle (1.04 cycles) 2.2 fs pulses have been demonstrated (the shortest ever, from a single-channel pulse compressor), thanks to the use of the d-scan technique for the measurement and compression [107, 83]. The kind of supercontinuum generation by HCF can find applications in the stabilization of the carrier-envelope phase (CEP) as well as in high-harmonic generation (HHG). HCF supercontinuum generation has some shortcomings, namely, it requires long fiber lengths (~1 m or more are commonly used), the need to operate a vacuum chamber (filled with a noble gas; where the fiber is housed), and sensitivity to beam pointing, which is often compensated by one ore more motorized mirrors controlled by a feedback loop.

Very recently, it was shown that the MPC process could be scalable to higher input energies, yielding pulses down to 5.4 fs [112]. In the next section we will study an alternative SCG process based on thin solid glass plates.

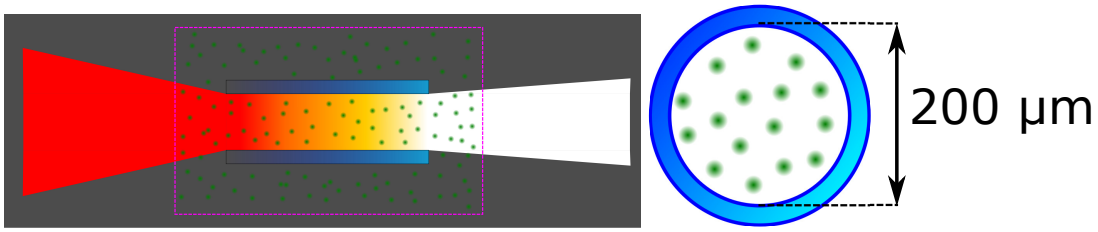

(a) HCF illustration (b) HCF cross-section

Figure 5.1: Simplified scheme of beam coupling and propagation in a hollow-core fiber.

5.2 MPC

The multi-plate continuum is a novel process for supercontinuum generation in solid media [113]. Unlike traditional SCG in bulk media or noble gases, the spectral broadening takes place in a series of thin plates (e.g. fused silica, 100 μm thick) instead of a single medium. It was shown that choosing plates with a small thickness distributed along the Rayleigh range of a focusing element can have a cumulative spectral broadening effect while reducing the length of propagation of a pulse inside the media and thus avoiding optical breakdown of the solid due to self-focusing effects.

In [113], MPC supercontinuum generated pulse was characterized by PG-XFROG, albeit without any dispersion compensation, which means that the measured pulses are

not temporally compressed to the maximum extent.

5.2.1 Experimental setup

The experimental setup (Figure 5.2) comprises two main parts: one for the spectral broadening process, i.e., the MPC, and the ultrafast pulse measurement part, i.e. a SHG d-scan in our case. The MPC part begins with a 1 m focal length lens that focuses our input beam onto a stack of six unevenly spaced, thin (100 μm) slides of fused silica placed at Brewster's angle. The uneven spacing is motivated by simulations [114], as well as by the criterion of obtaining the broadest spectrum as we place each individual slide in the setup while minimizing spatial wavefront distortions due to self-focusing. Both factors show that the spacing between successive slides gets shorter [114]. The long focal length of the lens gives us a large Rayleigh range that fully envelopes the slide stack, ensuring that the electric field strength is high enough along the whole stack to induce spectral broadening. The input beam has typically a diameter of ~10 mm, 140 μJ energy per pulse with a 25 fs pulse duration. The emerging beam (the spatial profile can be seen in Figure 5.3), has 80 μJ per pulse and its final broadened spectrum can be seen in Figure 5.5, along with the spectrum of the input laser pulse. This beam is then collimated by a concave mirror and directed to a pair of dispersion compensation mirrors (DCMs) which impart negative dispersion to the pulse (8 bounces). The rest of the apparatus follows the conventional SHG d-scan setup previously discussed in chapter 3.1.

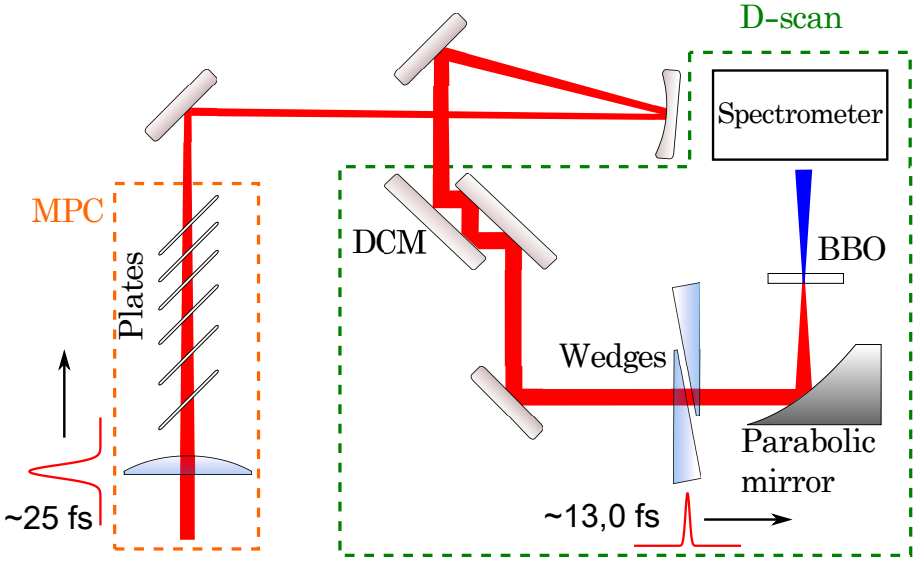

Figure 5.2: Schematics of the MPC generation and measurement setup.

The output spatial profile of the MPC process is shown in Figure 5.3, revealing a uniform and homogeneous mode with an additional ring structure. Only the central part of this beam (~50 μJ) is used while the ring structure is blocked with a iris.

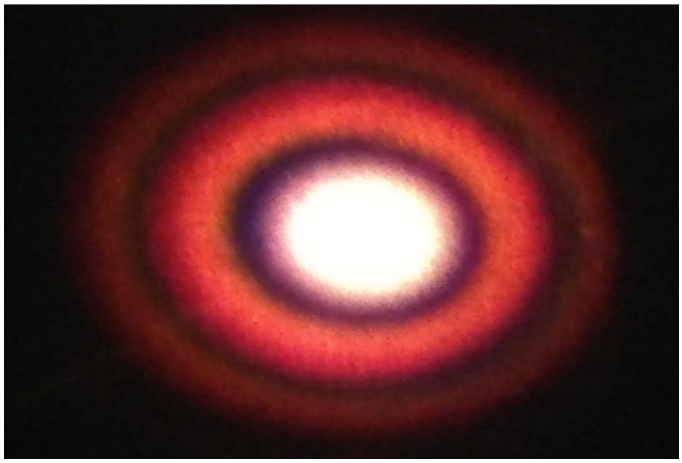

Figure 5.3: Spatial profile of the MPC beam showing a round central part along with a concentric rings structure. The photo was taken at an angle.

As was previously described in chapter 3.1, the SHG spectrum is recorded as a function of glass insertion, yielding the MPC d-scan trace, shown in Figure 5.4 (top).

The acquired trace has a relatively complex structure compared to previously SHG traces considered in [78, 79, 107] as well as the SHG d-scan traces in chapter 4. This situation can be attributed to the strong modulation of the output spectrum from the MPC process depicted in Figure 5.5. Nevertheless, the retrieved trace in Figure 5.4 is able to reproduce the main features of the acquired trace (d-scan error of 0.015 for a trace of size 210x320, over the insertion range and frequency range, respectively).

Figure 5.5 shows the initial spectrum from the amplifier, as well as the spectrum after broadening by the MPC process, along with the spectral phase of the output pulse retrieved by SHG d-scan.

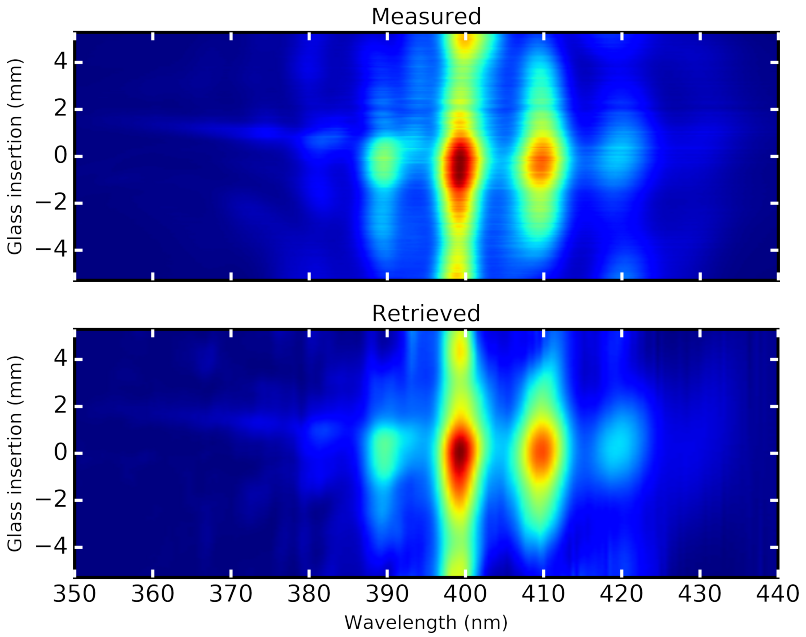

Figure 5.4: Top) measured MPC supercontinuum d-scan trace; bottom) retrieved d-scan trace.

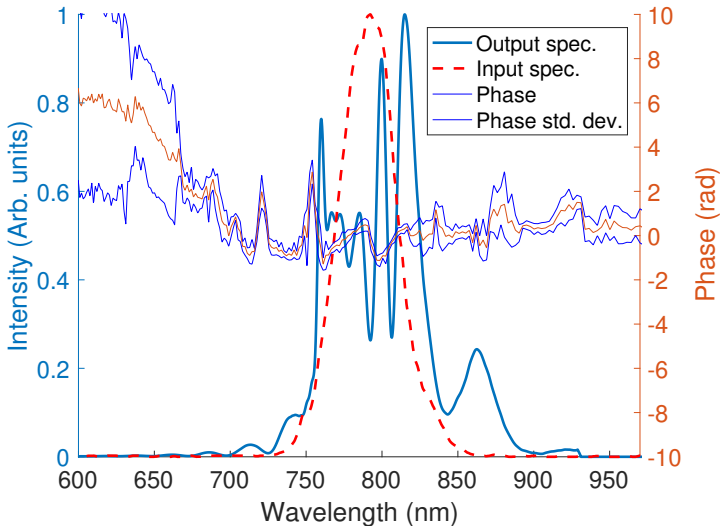

Figure 5.5: Input and output spectrum for the MPC process and the respective spectral phase of the emerging pulse along with the spectral phase standard deviation.

In the time domain, the retrieved phase along with the MPC broadened spectrum,

capable of supporting a 9.8 fs TL pulse, yields a 13.0 $\pm$ 0.3 fs retrieved pulse (Figure 5.6), which represents a $\gtrsim 2$ factor in pulse compression.

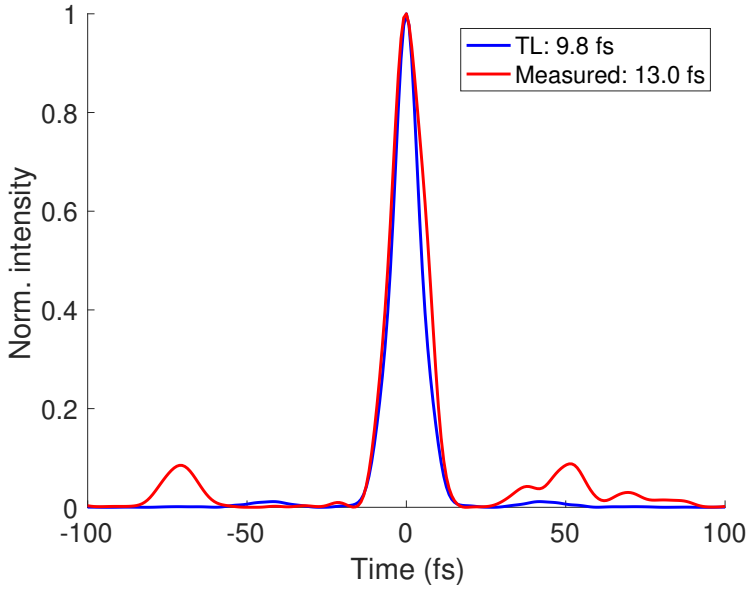

Figure 5.6: MPC TL and retrieved pulse intensities.

Figure 5.6 shows that although the retrieved pulse has some temporal satellites, the pulse energy is largely contained in the main pulse (~77%).

5.3 MPC spatiotemporal characterization

While so far the supercontinuum generation by MPC was made with amplifier pulses of ~25 fs to ~30 fs as input, not all Ti:sapphire lasers output pulses with such durations. Ti:sapphire laser amplifiers with longer pulse durations (e.g., <120 fs) are very common and widespread and could greatly benefit from pulse compression techniques. In this section we will do a spatiotemporal characterization of a pulse generated by a ~120 fs Ti:sapphire amplifier (at 1 kHz repetition rate) from the ALF[6] group at the University of Salamanca, by using the STARFISH technique described in chapter 2.6.1 together with SHG d-scan for the STARFISH reference phase determination. The author is grateful for the possibility of using a single-shot SHG-dscan system (cf. chapter 3.4) from Sphere Ultrafast Photonics for the temporal characterization. An initial pulse from the laser amplifier, with 580 μJ is focused via a 2 m focal length lens into a sequence of five 100 μm thick fused silica plates (Figure 5.7) placed at Brewster's angle.

[6]https://laser.usal.es/alf/en/home/

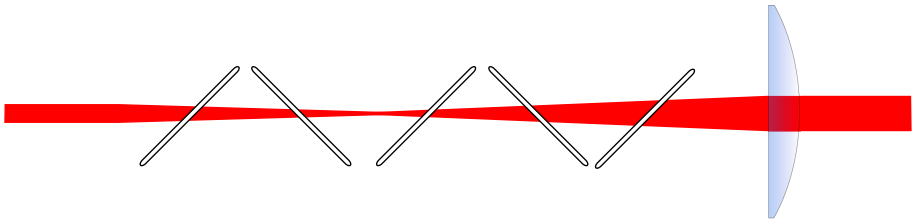

Figure 5.7: MPC setup. This geometry should favor a spatially more homogeneous spectral broadening along the beam.

The output beam (containing a ring structure) has an energy of 500 μJ, in other words, a 86% of supercontinuum generation efficiency was obtained. The central part of the beam is filtered through an iris. It has 400 μJ, and exhibits a high degree of circular symmetry, as show in Figure 5.8.

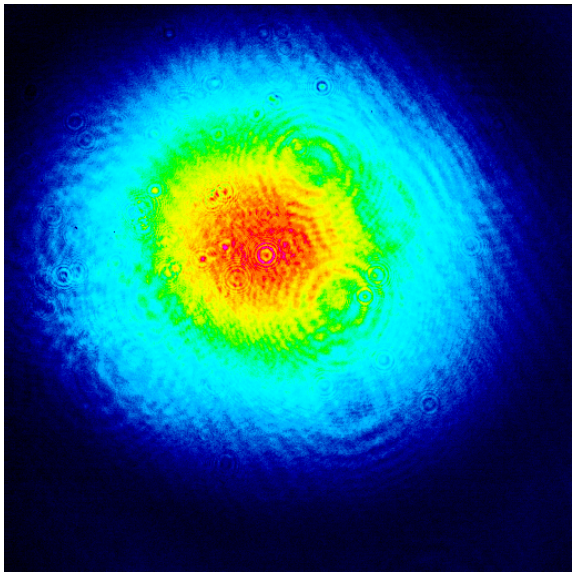

Figure 5.8: Spatial profile obtained from camera (DataRay). Diffraction rings are due to few particles of dust in the camera.

The spatiotemporal characterization setup schematic is depicted in Figure 5.9. A 50/50 beamsplitter is used to create a beam replica that goes to the STARFISH setup, while the remaining replica goes to a DCM mirror (Layertec GmbH) compressor, undergoing 32 bounces each with a nominal GDD of -40 fs^2. The beam emerges from the DCMs compressor with a energy of ~50 μJ, which is then attenuated by a neutral density filter (not shown) and steered into the single-shot d-scan apparatus.

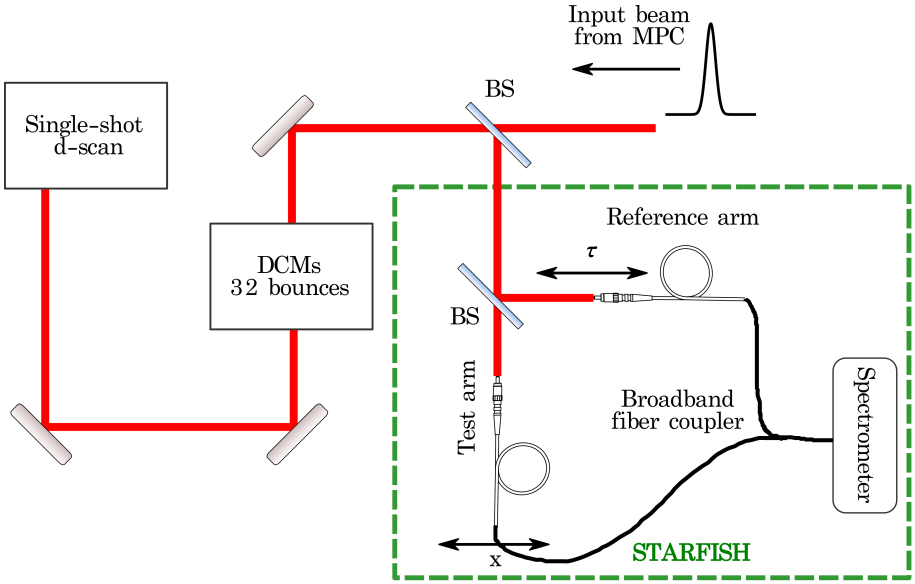

Figure 5.9: Spatiotemporal characterization setup.

The measured and retrieved d-scan traces are depicted in Figure 5.10.

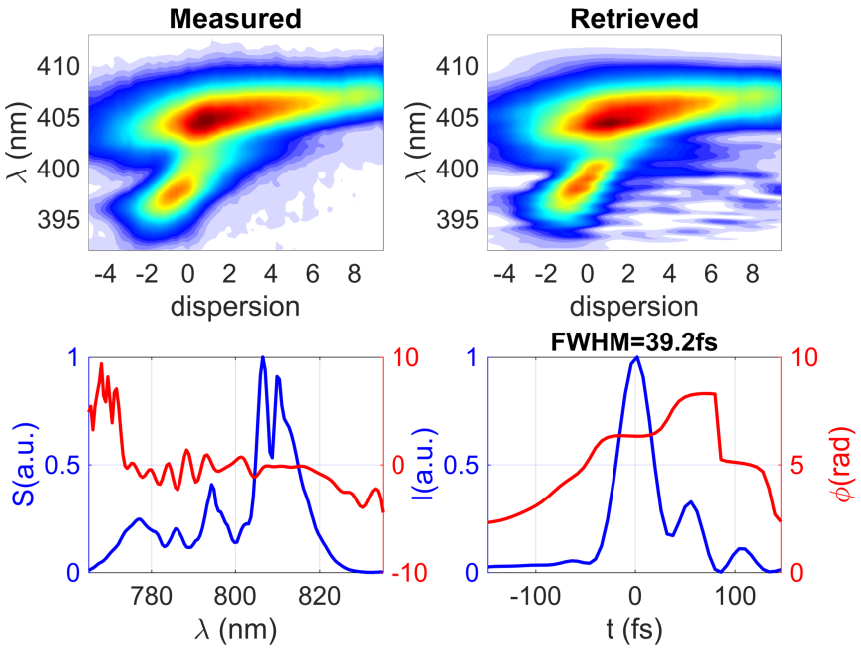

Figure 5.10: Measured and retrieved traces from single-shot d-scan, along with the spectrum, spectral phase, pulse intensity and temporal phase.

The results obtained with the STARFISH diagnostic are shown in Figure 5.11.

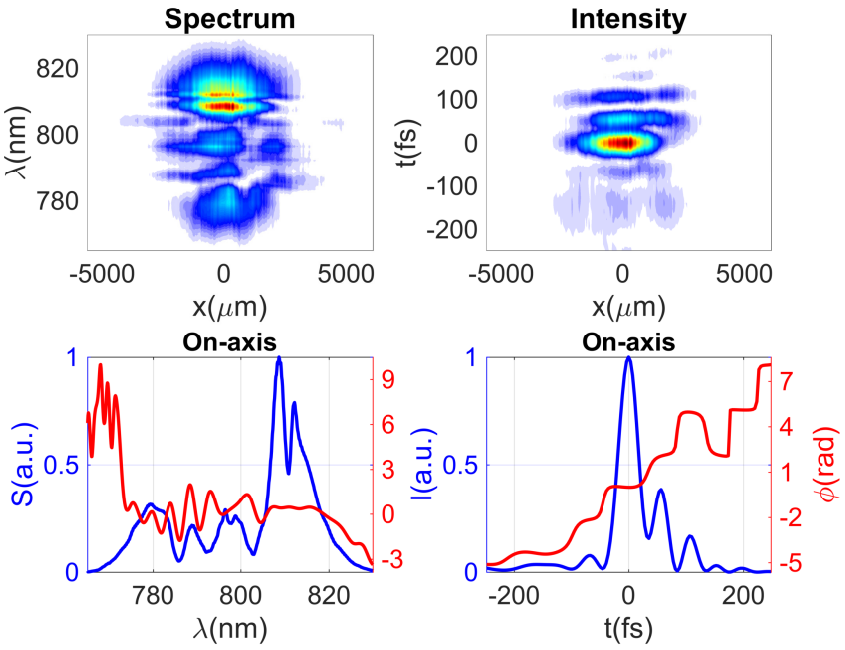

Figure 5.11: STARFISH results: top left) spectrum as a function of position; top right) pulse intensity as a function of position; bottom left) spectrum and spectral phase at the center of the beam (i.e., $x = 0$); bottom right) pulse intensity and temporal phase at the center of the beam.

The STARFISH trace has a high degree of symmetry with respect to the on-axis position $x = 0$. This is further evidenced in the plot of temporal profile as a function of position, in the sense that it shows only small variations within the central zone centered at $x = 0$, while deviations are only observed in the edges of the beam. The on-axis pulse duration, was 39.2 fs, which is much shorter than the initial ~120 fs. For other positions ($x \neq 0$), we plot their FWHM in Figure 5.12.

The pulse duration along the x axis, seems to hold mostly constant within a flat region of ~4000 μm of diameter. Beyond this region the plot is not as meaningful as the SNR is much smaller.

5.4 Conclusions

To the best of our knowledge, we have performed the very first d-scan measurements of the MPC, showing a ~2 pulse shortening factor, though, with recent findings [112], it was

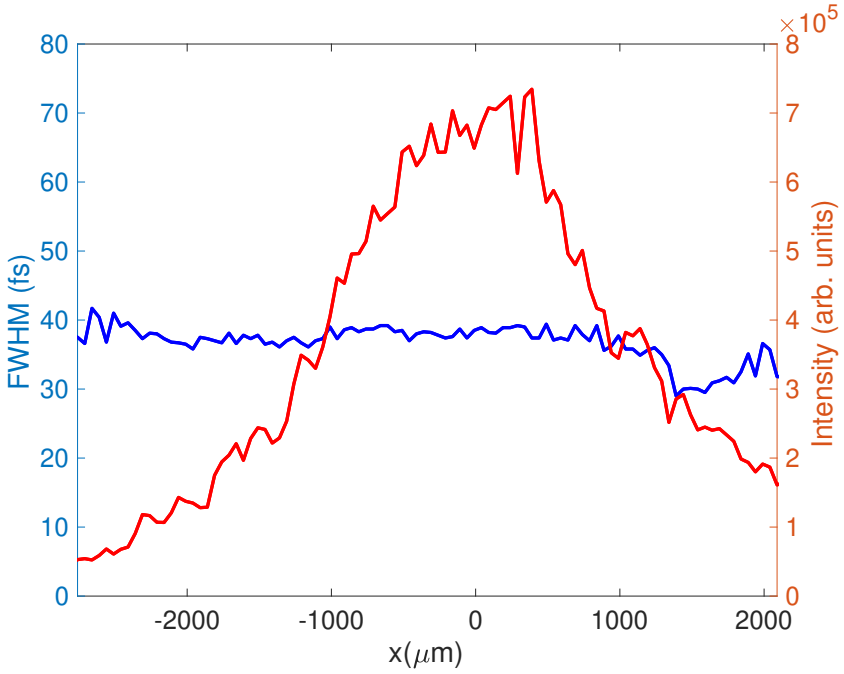

Figure 5.12: FWHM of the MPC beam as a function of position (blue); Spatial intensity of the beam as a function of position (red).

shown that the process has room for improvement. Nevertheless, it is clear that a MPC process can be a good alternative to HCF supercontinuum generation, as it is relatively inexpensive (requires thin plates and regular optical components), it is not as sensitive to beam pointing, and has a high efficiency ratio while maintaining a relatively high beam quality.

A spatiotemporal characterization study of pulses with longer duration was done, yielding a pulse shortening factor of ~3 (from 120 fs to 39 fs), as well as a good beam spatial profile. A higher energy throughput can be obtained by substituting the DCMs mirrors by other mirrors with a higher negative dispersion, allowing us to significantly reduce the number of bounces, and thus also reducing the losses in the DCMs compressor. This study shows that a MPC based supercontinuum process is an easy and cost effective way to reach shorter pulse durations with good beam spatial quality, when such pulses are not directly available from the laser systems, say, laser amplifiers with longer pulse durations.

6 UV supercontinuum and dual SD d-scan

In this chapter, we will describe a recent MPC-based supercontinuum process in the UV, centered at 400 nm. The pulses generated from this process are characterized by SD d-scan. The possibility of simultaneously retrieving two ultrashort pulses from one SD d-scan trace is also demonstrated, constituting a powerful approach for the temporal characterization of pulses with non-homogeneous spatiotemporal structure. While the work is done using UV sources centered at 400 nm, the pulse characterization method itself can be used to measure ultrashort pulses with shorter wavelengths, i.e., in the deep-ultraviolet (DUV; 200 ~ 300 nm) range (this topic will be further commented in the conclusions of this chapter).

6.1 Sources of coherent UV light @ 400 nm

Ultrashort pulses in the UV have important applications in spectroscopy [15, 115]. Sources of ultrashort pulses in the UV can be obtained by using SHG process [116], SFG process [117, 118]. as well as propagation of frequency-doubled Ti:sapphire laser pulses in HCF fibers [119].

Another way of obtaining broadband ultrashort UV pulses centered at 400 nm is by coupling frequency-doubled Ti:sapphire laser pulses into hollow-core fibers [120, 121, 119]. All methods mentioned previously require some careful use of dispersion compensation devices (prism pairs) and deformable mirrors, and so are not trivial to implement.

MPC-based supercontinuum generation was first reported in [113], and as seen in this publication and in the spatio-temporal characterization described in section 5.3, it is a scalable, high efficiency supercontinuum generation process, capable of yielding a good spatial profile.

6.2 Multiplate continuum (MPC) at 400nm

Taking into account the complexity of current setups for nonlinear spectral broadening, e.g., the need for long hollow-core fibers (which suffer from pointing stability issues [122]

and, limited scalability), a MPC supercontinuum centered around 400 nm seems like a very appealing concept. This is based on the expectation that the MPC at 400 nm would enjoy the same properties as the NIR case, e.g, highly efficient pulse broadening and a good spatial profile, with a simple setup. Therefore, the MPC at 400 nm seems to be an ideal UV ultrashort pulse source to test the SD d-scan in the ultraviolet range. With MPC being a hot topic and with the ease of obtaining pump pulses centered at 400 nm by generating a SHG beam from a Ti:sapphire amplifier using a frequency-doubling crystal, the race to obtain the results from MPC in the UV was won with [123] reporting the first measurements in 2017. In this chapter, I will describe work done on the very first SD d-scan measurements from a UV source, and will further explore some aspects that were not addressed in [123], culminating with another variant of the d-scan technique capable of simultaneously retrieving two unknown pulses from a single d-scan trace.

6.3 Experimental setup and results

The experimental setup is made up of two parts: the light source (MPC@400 nm) and the setup for SD d-scan (cf. Figure 6.1). We begin with a beam from our Ti:sapphire laser amplifier which undergoes a waist reduction by a factor of 4 with a telescope. A type-I BBO crystal, 200μm thick is used to frequency double the fundamental beam (~400 mW @800 nm). A dichroic mirror separates the fundamental beam from the UV pump beam, which in turn is focused by a f = 1000 mm lens into a set of five thin fused silica plates (100 μm thick each) placed at Brewster's angle. Starting with a UV pump power of 72 mW @ 400 nm (obtained after the dichroic mirror) we obtain 60 mW at the output of the MPC beam, resulting in an efficiency of 83%, which is comparable with the efficiency obtained in [123]. No extra plates were added, as it did not lead to additional spectral broadening. A further broadening may be possible by introducing a intermediate compression stage and coupling the resulting beam into another MPC stack. The average distance between consecutive plates is ~4 cm, optimized for spectral broadening, thus the MPC broadening is achievable in a length of ~ 20 cm, much shorter compared to hollow-core fibers. This comparison holds true even if we consider the long coupling lens (f = 1000 mm) as part of the MPC supercontinuum setup, since hollow-core fibers generally use long coupling lens (a meter or more) as well.

After the MPC process, the beam is then directed to a pair of DCMs (CM82, Ultrafast Innovations GmbH), where it undergoes a total of 24 bounces, each bounce with a nominal GDD of -50 fs^2 at 400 nm. The emerging beam then traverses a pair of fused silica wedges that impart a variable amount of dispersion. Two parts of the beam are selected

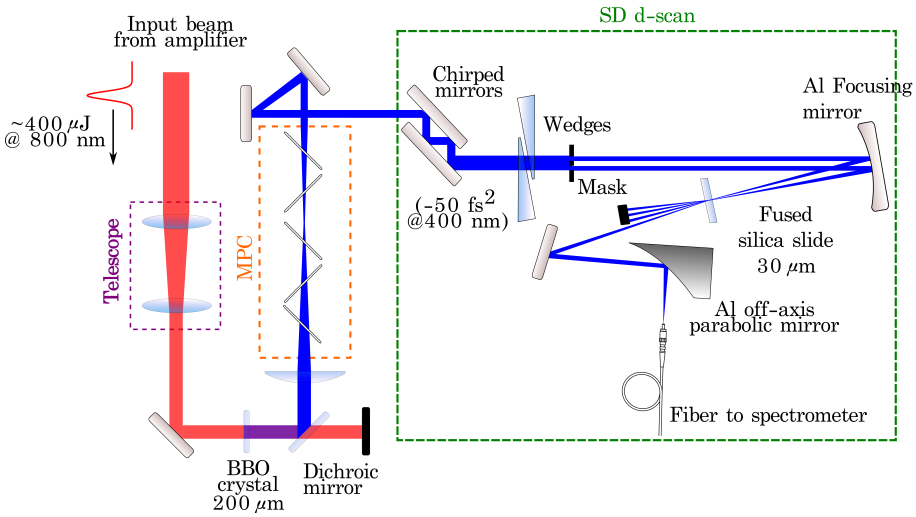

Figure 6.1: UV-MPC generation and measurement setup.

through a mask with two circular holes, separated by ~1 mm and with a diameter of 1.2 mm each, with enough energy for the subsequent self-diffraction effect. The power for both beams at the exit of the mask is 1 mW to avoid any undesirable self-phase modulation in the fused silica slide used to generate the self-diffraction signal [104]. These two beams are then focused onto a 30 μm fused silica slide by a f = 200 mm concave mirror, to generate the self-diffracted beams. One of the self-diffracted orders is then be collected and focused by an 90º off-axis parabolic mirror into the spectrometer fiber and the spectra registered as a function of the insertion of the wedges to record the SD d-scan trace.

Figure 6.2 shows a typical spectral broadening measured after the MPC plates, starting from a UV pump pulse centered at 400 nm, with and energy of 72 μJ. In this measurement, the transform-limited pulse durations of the pump and the output pulse are 24.4 fs and 10.4 fs, respectively.

Spectral broadening by MPC seems like a promising option for the generation of broadband UV pulses, at least from the point of view of efficiency and extent of broadening. However the beam profile (cf. Figure 6.3), besides having a ring structure around the center, which is expected for an MPC process, also has a central part of the beam which does not have a well defined shape. Moreover, the spectrum changes according to the position of the beam, i.e., the beam has spectral spatial inhomogeneity. This inhomogeneity have been observed in [124] in MPC experiments driven by NIR pulses centered

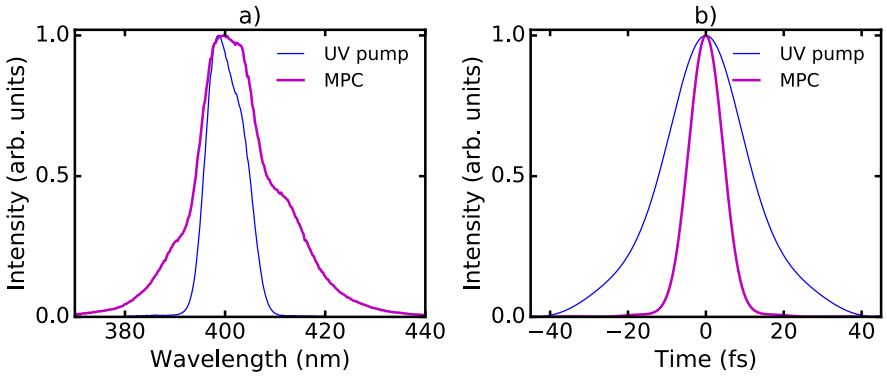

Figure 6.2: a) Typical broadening from the UV-MPC process in our setup, b) envelope of the TL pulse profiles calculated with the spectrum of the UV pump (24.4 fs) and the MPC spectrum (10.4 fs).

at 1025 nm. This spatial inhomogeneity has also been observed by the authors of [123][7] in MPC experiments in the UV and could be due to an incipient filamentation caused by the fact that UV photons are more energetic than NIR ones (very homogeneous beams where obtained in our NIR MPC generation).

In the following discussion, we will disregard the ring structure (i.e., by blocking it with an iris) and focus only on the central portion of the beam.

6.3.1 Beam inhomogeneity in UV-MPC beams

We observe that the beam is spectrally inhomogeneous across its transverse dimensions. This may pose a significant issue in the characterization of ultrashort pulses, as the nonlinear effect is frequently assumed to be due to and expressed as a function of a single electric field, which naturally assumes a homogeneous beam. This assumption is used both in FROG techniques [48] as well as in dispersion scan techniques [78]. In the present case however, the acquired SD d-scan trace should be more accurately described as a result of the interaction of two distinct electric fields, since the pulses that emerge from the mask have different spectral properties. To make sure that the selected beams after the mask remain mostly constant in terms of spectrum, i.e., where they exhibit no dependence or at least a weak dependence along the transverse dimensions, we chose to use small holes, e.g., a hole diameter of 1.2 mm as mentioned before (it was not possible to observe a self-diffraction effect with a smaller diameter of 0.8 mm).

[7] Communication done in conference presentation.

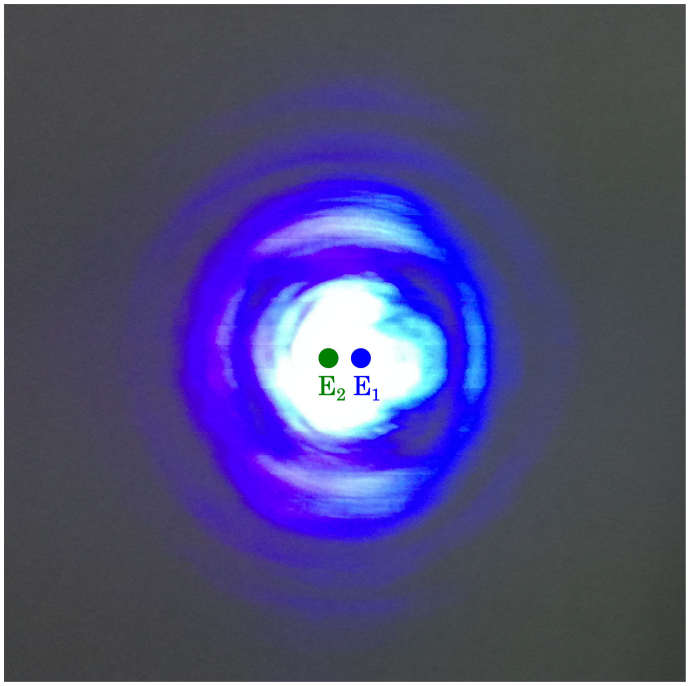

Figure 6.3: Typical UV-MPC beam profile obtained in our setup. Two circles (blue and green) represent the two beam portions that emerge from the mask.

In our experiment a SD d-scan trace is measured along with the fundamental spectrum of each of the two beams, which will be labeled as pulse/beam 1 and pulse/beam 2, respectively. The field E_{NL1} (cf. Figure 6.4) that is generated through the self-diffraction effect is the one whose signal is recorded by the spectrometer's fiber.

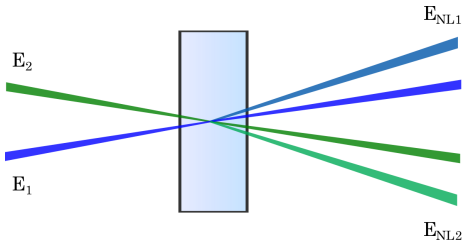

Figure 6.4: SD interaction diagram; generation of the self-diffracted beams.

Consequently, that means that the SD effect can be expressed by a modified version of Eq. 4.4 presented in chapter 4, to take into account the two different fields E_1 and E_2

$$E_{NL1}(t,z) \propto E_1^2(t,z) \times E_2^*(t,z). \tag{6.1}$$

Despite the homogeneous beam constraint from the regular d-scan method, we have tested the capability of SD d-scan to retrieve the measured traces from this setup as is, i.e., still assuming that the homogeneous beam constraint still holds (hence all pulses/beams are identical, $E(t) = E_1(t) = E_2(t)$).

Figure 6.5 shows the acquired trace as well as the trace retrieved using the spectrum from pulse 1.

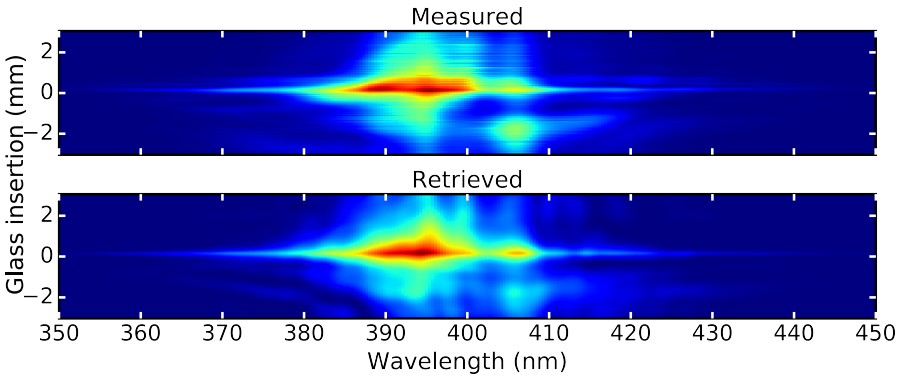

Figure 6.5: Top) Measured SD trace in the UV. Bottom) Retrieved trace with spectrum from pulse 1.

The corresponding spectrum, spectral phase, along with the retrieved pulse intensity is shown in Figure 6.6. The spectrum from pulse 1 can support a TL pulse of 8.1 fs, and the retrieved duration of the pulse was found to be 16.5 $\pm$ 0.1 fs. A d-scan error of 0.032 for a trace with size 210 by 384 points (along the insertion and frequency axes, respectively).

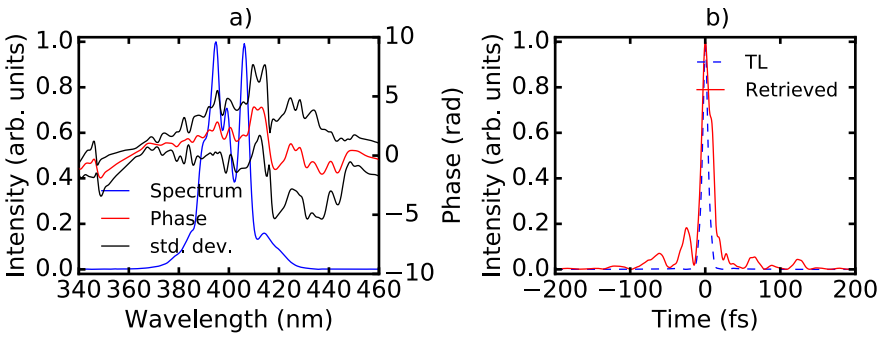

Figure 6.6: a) Spectrum and retrieved spectral phase using the spectrum of pulse 1; b) TL pulse and retrieved pulse.

Clearly, the small uncertainty in the pulse duration cannot be the only metric to describe the quality of retrieval of the pulse, as we can see that the standard deviation of the spectral phase is relatively high (up to ~3.5 rad at some points) throughout the fundamental spectrum.

Figure 6.7 shows the acquired trace along with the trace retrieved using the spectrum from pulse 2.

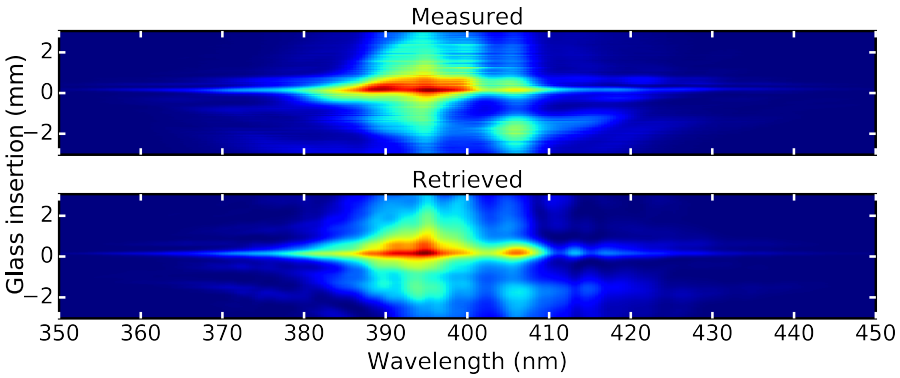

Figure 6.7: Top) Measured SD trace in the UV. Bottom) Retrieved trace using spectrum from pulse 2.

The spectrum from pulse 2 can support a TL pulse of 7.6 fs, and the retrieved pulse duration was found to be 10.2 $\pm$ 0.4 fs. Similar to the case with pulse 1, the algorithm returns a trace that reproduces with some difficulty the measured one, and a spectral phase with relatively high standard deviations. The d-scan error was 0.033 for a trace with size 210 by 384 points along the insertion and frequency axes, respectively.

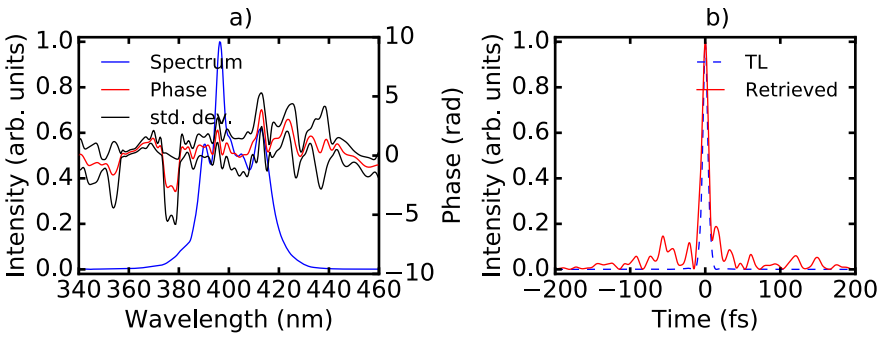

Figure 6.8: a) Spectrum and retrieved spectral phase using the spectrum from pulse 2; b) TL pulse and retrieved pulse.

The results obtained from either pulse seem to have a fair agreement between measured and retrieve traces. The high standard deviation of the spectral phase is also an indication that the retrieval algorithm is struggling to retrieve the pulses under the assumption of a homogeneous beam. We now explore ways to improve the phase retrieval process.

6.4 Dual SD d-scan

In order to overcome the issue mentioned earlier, we must first get rid of this homogeneous beam constraint. We formally consider that the self-diffraction effect is generated by two distinct electric fields, $E_1(t,z)$ and $E_2(t,z)$, where the dependence on glass insertion, z, comes from the propagation inside the pair of wedges. Under these circumstances, the electric fields generated by self-diffraction are given by Eq. 6.1 and

$$E_{NL2}(t,z) \propto E_1^*(t,z) \times E_2^2(t,z). \tag{6.2}$$

$E_1(t,z)$ and $E_2(t,z)$ in turn are expressed as

$$E_1(t,z) = \int_{-\infty}^{+\infty} \tilde{E}_1(\Omega) e^{-izk(\Omega)} e^{i\Omega t} d\Omega, \tag{6.3}$$

$$E_2(t,z) = \int_{-\infty}^{+\infty} \tilde{E}_2(\Omega) e^{-izk(\Omega)} e^{i\Omega t} d\Omega. \tag{6.4}$$

Eq. 6.1 and Eq. 6.2 are not equivalent, as they reflect the dissimilarity of the two input beams. The d-scan trace, $I(\omega,z)$, is then given by

$$I_{SD}(\omega,z) \propto \left| \int_{-\infty}^{+\infty} E_{NL}(t,z) e^{-i\omega t} dt \right|^2, \tag{6.5}$$

where E_{NL} can be either E_{NL1} or E_{NL2}, depending on the nonlinear beam one chooses to measure (in our case E_{NL1}). Figure 6.3 shows the selection by the mask, of the two parts (blue and green) of the inhomogeneous beam. Through the interaction in the 30 μm fused silica slide, two self-diffracted beams are generated. Regardless of the self-diffracted beam chosen (E_{NL1} or E_{NL2}), information on both pulses is encoded in $I_{SD}(\omega,z)$, as both pulses contribute to the trace. The task at hand now, is to figure out a way to retrieve both pulses using a d-scan trace.

Inspired by the fact that a d-scan trace is a quantity that contains more data than the amount strictly necessary to characterize a pulse, we wonder if it is possible to simultane-

ously retrieve both pulses, from a single SD d-scan trace and an additional fundamental spectrum (two spectra in total), i.e, one for pulse 1 and another for pulse 2, in contrast with the conventional d-scan retrieval involving a trace and just one fundamental spectrum.

6.4.1 Dual SD d-scan simulation

To explore the possibility of simultaneously retrieving both pulses, we take the experimentally measured fundamental spectrum of each pulse and generate a SD d-scan trace according to Eq. 6.1, where the spectral phase of each pulse was chosen arbitrarily. The retrieval code is then modified to accommodate not only two fundamental spectra, but also the capability to guess the phase of each respective pulse. For pulse 1 we assumed a phase with 80 fs^{2}of GDD @ 400 nm, while for pulse 2 we assumed a phase with 40 fs^{2}of GDD @ 400 nm plus an additional function given by $10sinh\left[2\left(\omega-\omega_0\right)^3\right]\times sin\left[15(\omega-\omega_0)\right]$, with $\omega_0 = 2\pi\times 0.75\times 10^{15}$ Hz. Figure 6.9 shows the numerically simulated measured trace as well as the retrieved trace.

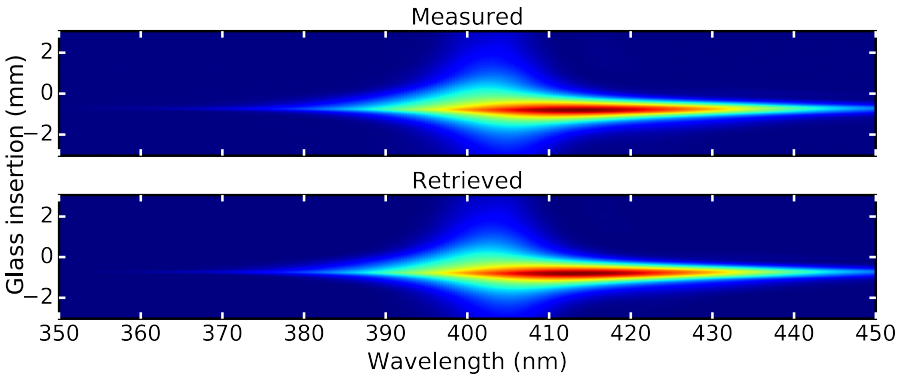

Figure 6.9: Numerically simulated measured and retrieved SD traces.

Trace error of 0.001 for a trace size of 210 by 384 points (along the insertion and frequency axes, respectively). The associated spectra, the simulated and the retrieved spectral phase for each pulse are shown in Figure 6.10.

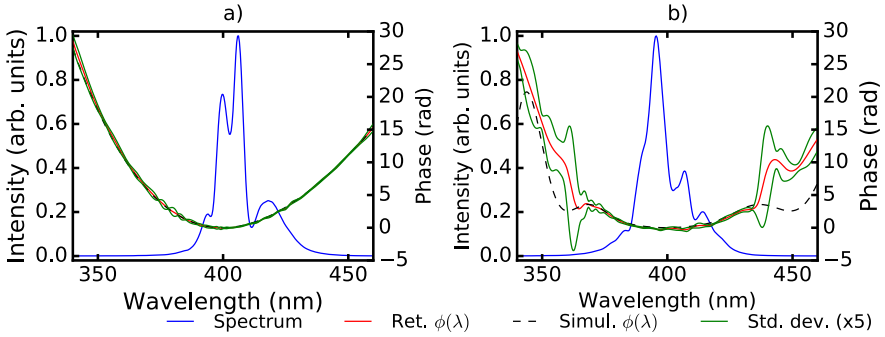

Figure 6.10: Dual d-scan simulated spectra and retrieved spectral phases for a) Pulse 2 and b) Pulse 2. Standard deviations have been multiplied by a factor of 5.

The algorithm is able to deliver retrieved phases in good agreement with the simulated ones in the regions where spectra are not negligible. The standard deviations of the spectral phases were multiplied by a factor of 5 to be easier to visualize. Once again, it is important to stress that the spectral phases were retrieved simultaneously, using only one d-scan trace. The TL duration of pulse 1 and pulse 2 is 7.8 fs and 7.4 fs. The respective intensities for pulse 1 and pulse 2 are shown in Figure 6.11. We can observe a good agreement between the simulated and retrieved pulse profiles for both pulse 1 and pulse 2. The simulated pulse duration for pulse 1 is 23.7 fs, and for pulse 2 is 19.5 fs. The retrieved pulse duration for pulse 1 is 24.3 $\pm$ 0.1 fs, and for pulse 2 is 20.0 $\pm$ 0.2 fs. The field error (Eq. 3.8) is 6.4% for pulse 1 and 13% for pulse 2.

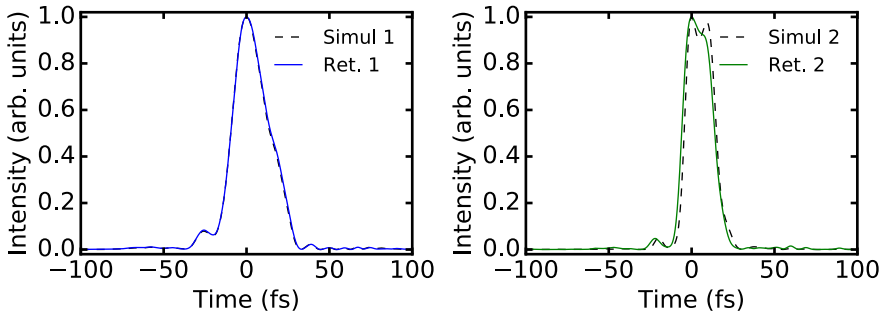

Figure 6.11: Retrieved pulse intensities from dual SD d-scan simulations.

The simulation results are very encouraging, in the sense that the retrieved trace and spectral phases are very close to the simulated ones. We can now discard the homogeneous beam constraint, and proceed to tackle the retrieval of the experimentally measured traces.

6.4.2 Dual SD d-scan results

The application of the retrieval approach mentioned above to experimental data yielded a retrieved trace with a better resemblance to the measured trace, as Figure 6.12 shows.

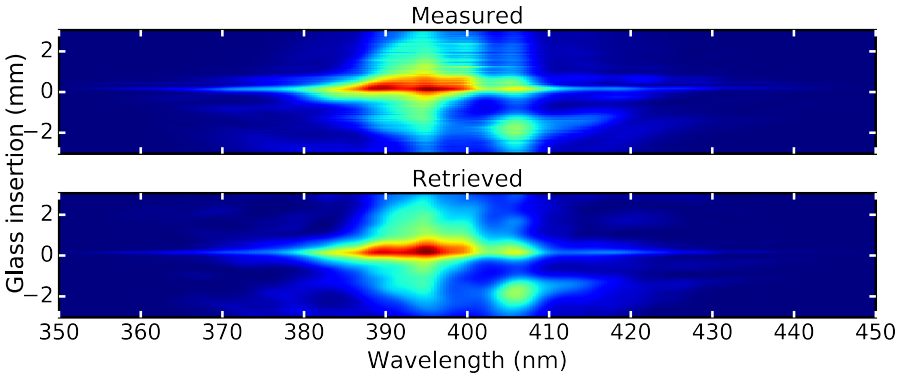

Figure 6.12: Dual d-scan traces. Top) Measured. Bottom) Retrieved.

We can observe that under these new approach to retrieval, the retrieved trace can reproduce more faithfully the features of the measured trace, as compared to either Figure 6.5 or Figure 6.7. The d-scan error is 0.019 for a trace with size 210 by 384 points (along the insertion and frequency axes, respectively) a notable improvement, compared to the retrieval in section 6.3.1. The spectrum and spectral phase for both pulses 1 and 2 are shown in Figure 6.13.

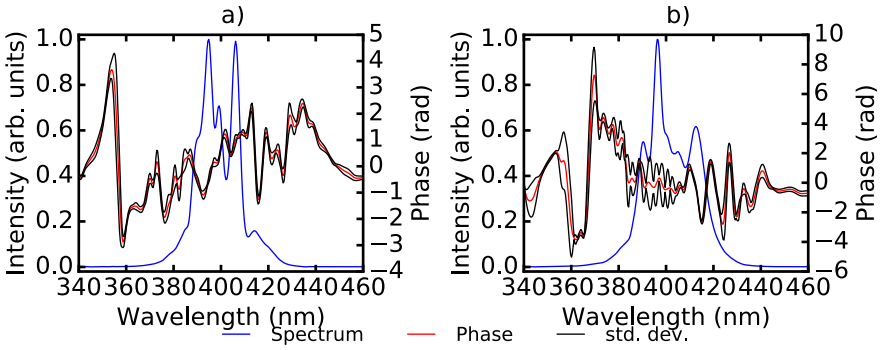

Figure 6.13: Dual SD d-scan spectra and retrieved spectral phases for a) pulse 1 and b) pulse 2.

The retrieved spectral phases have a smaller standard deviation compared to the cases previously shown in Figure 6.6 and Figure 6.8. From the spectra and spectral phases we can then recover the temporal profile of each pulse, as depicted in Figure

6.14. The spectrum for pulse 1 supports a TL pulse duration of 8.1 fs, while pulse 2 supports a TL pulse duration of 7.6 fs.

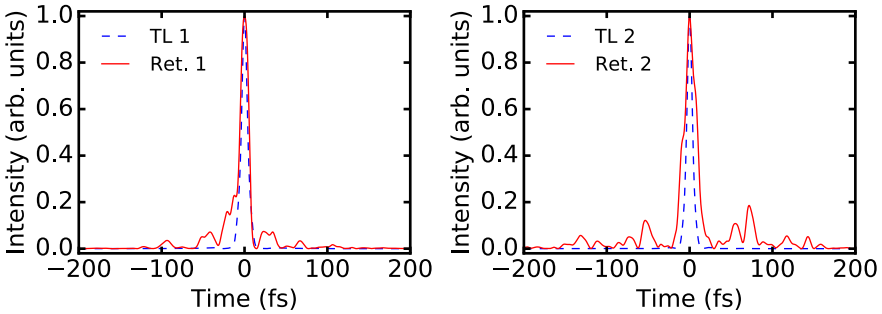

Figure 6.14: Dual SD d-scan retrieved pulse intensities.

The retrieved duration of pulse 1 is 11.6 $\pm$ 0.1 fs, while pulse 2 has a pulse duration of 16.5 $\pm$ 1.7 fs.

6.4.3 Pulse compression

It is clear from the results shown in the previous subsection that two different pulses can be simultaneously characterized. As the two distinct pulses have different spectral phases, one may expect to have two different values for the amount of glass insertion that compresses each pulse. Leveraging the ability of the d-scan technique to obtain the pulses under test (and thus their duration) after a given amount of glass dispersion, we can determine the amount of glass insertion for the optimal compression of pulse 1 and pulse 2. The search for the shortest pulse can be accomplished by searching (along the glass insertion range, z) for the minimum pulse duration of $E(t, z)$, the electric field obtained after linear propagation by an amount z. The values for optimal pulse compression are $z = 0.12$ mm for pulse 1 and $z = 2.53$ mm for pulse 2, yielding pulse durations of 8.5 fs and 11.1 fs, respectively (cf. Figure 6.15).

The achieved pulse durations in optimal compression conditions yield shorter pulse durations (as expected), where in the case of pulse 1 it achieves a value close to the TL limit of 8.1 fs while in the case of pulse 2 the obtained value is not as close to the TL duration of 7.6 fs. This fact may be attributed to non-zero higher-order dispersion as evidenced by the pre- and post-pulse structure around the main pulse.

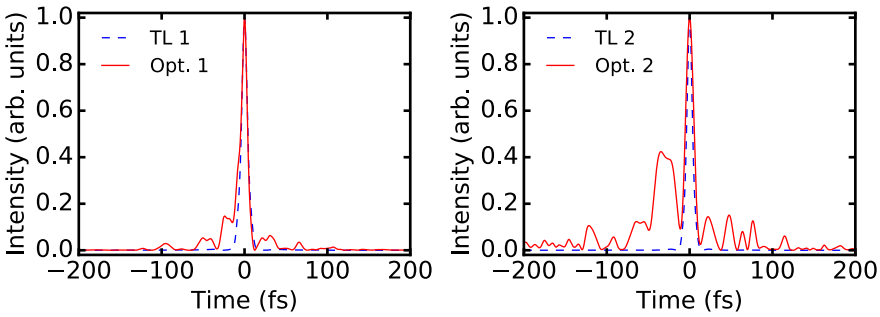

Figure 6.15: Transform-limited pulse intensities and compressed pulse intensities, i.e., pulse intensities associated to the optimal glass insertion for each pulse.

6.5 Conclusions

In this chapter, we presented the very first measurements of ultrashort pulses in the UV using the self-diffraction dispersion scan technique. A recently developed source of broadband UV supercontinuum based on MPC was studied with this technique. Although the characterization of such source posed an issue in the early stages of the work (i.e., spectrally inhomogeneous beam), a new d-scan variant based on the SD effect was devised to overcome said issue and allow us to have a more accurate measurement of such pulses by simultaneously retrieving the fields of the two different pulses that produce the self-diffraction signal. This new method may find use in the measurement of ultrafast laser pulses of an inhomogeneous high-intensity beam. As the MPC is a scalable process, for higher intensities, larger area beams can be used, hence inhomogeneities are more increasingly more likely to appear.

As previously written in this chapter's introduction, the SD d-scan can be used to measure ultrashort pulses in the DUV region of the electromagnetic spectrum, since the self-diffraction effect can happen for any wavelength and it is only limited by the transparency range of the nonlinear medium where it occurs. Sources of DUV can be implemented via HCFs [125, 126, 127, 128], by filamentation [129, 130], spectral broadening during filamentation in gas of third-harmonic pulses from a high-energy dual-stage amplifier [131], and direct harmonic upconversion of few-cycle femtosecond pulses in gases [132, 133, 134]. We believe that this technique is still scalable to even lower wavelengths (< 200 nm) provided that the setup is placed inside a vacuum chamber so as to avoid the absorption of the beam in air.

7 In-situ characterization of sub-4-fs pulses for HHG

Coherent radiation in the spectral region of the extreme ultraviolet (XUV) and soft-X-ray spectral regions is useful in imaging at the nanoscale, with applications in coherent diffraction imaging (CDI) [135, 136] and in spectroscopy, with applications in chemistry [137, 138]. Synchrotron radiation [139] as well as free electron lasers [140] are examples of sources in these spectral regions, though they require the building and operation of large facilities. The observation of high-harmonic generation (HHG) in gases [21], paved the way for the creation of tabletop XUV/soft-X-ray sources using ultrashort laser pulses. In spite of their lower flux they enable higher temporal resolutions (few-fs) than the synchrotron (~50 ps) and free-electron lasers (FELs; tens of fs).

The optimization of the HHG process relies on the knowledge of the driving optical pulse, which is often characterized off-target with a separate apparatus. There are on-target techniques able to characterize ultrashort pulses, like ionization-SPIDER [141], a transient absorption spectroscopy - based measurement technique [142] and attosecond streaking [143, 144]. The ionization-SPIDER is limited to weak pulses (<150 nJ), while [142] requires a pump-probe scheme with an attosecond XUV pulse to retrieve the optical pulse. The attosecond streaking technique has a higher degree of complexity due to the need of photoelectrons time-of-flight spectrometers.

A new, simpler measurement technique based on THG taking place in the same medium used for HHG experiments, a gas jet, is described in this chapter. This technique involves the HHG apparatus itself, does not involve a pump-probe scheme (thus, no need for time delay control between pulses), nor does it need any additional equipment other than off-the-shelf components. The results obtained by this dispersion-scan-based technique has achieved a very good agreement compared with the SEA-F-SPIDER technique [73, 144], taking into account that both techniques are based in completely different processes, SFG in a crystal in the case of SEA-F-SPIDER and THG in gas in our case. A brief introduction will be given, followed by the experimental setup and ending with the pulse retrieval work and discussion of the results. The author contributed with the processing and pulse retrieval of the data as well as with the discussion of the results.

7.1 On High-harmonic generation in gases

High-harmonic generation (HHG) is conceptually simple, as it only requires the focusing of intense ultrashort pulses onto atoms of a noble gas (e.g., argon and neon) in the form of a gas jet or contained in a gas cell placed in vacuum, resulting in newer upshifted frequencies, which are odd multiples of the driving laser frequency [145]. The generation of high-harmonics is also possible in solids, but this process is not described in this work. The interested reader may refer to [146, 147, 148, 149].The experimental implementation HHG in gas requires some complexity though, as it requires the operation of vacuum equipment. Unlike previously believed, each successive harmonic is not necessarily weaker compared to the previous one, i.e, there is no monotonic attenuation, in fact a "plateau" of higher harmonic can be observed [150], culminated by a eventual frequency cutoff which is the signature of a highly nonlinear and nonperturbative process. This phenomenon makes HHG in gas a suitable source for the creation of coherent XUV and soft-Xray radiation. Classically, HHG can be explained by the three-step model [151, 152], whereby an electron undergoes tunnel ionization under the influence of the electric field of the incident laser pulse, and then accelerated, gaining kinetic energy from the laser field. When the sign of the electric field of the pulse reverses, the electron is accelerated back and recombines with its parent ion, releasing higher energy radiation. The harmonic cutoff energy, $\mathcal{E}_c$, can be given by [151, 152],

$$\mathcal{E}_c = I_p + 3.17U_p \tag{7.1}$$

where I_p is the ionization potential of the medium and U_p is the ponderomotive energy, which corresponds to the average kinetic energy of a free electron in the pulse electric field. The ponderomotive energy is given by,

$$U_p = \frac{e^2 E_0^2}{4m_e\omega^2} \tag{7.2}$$

where e, is the electron charge, m_e the electron mass, E_0 and ω, the amplitude and angular frequency of the driving electric field. In the temporal domain, it was shown that HHG spectra can produce a train of attosecond pulses [153], paving the way for new applications [154, 155, 156].

7.2 Goals

The objective of this work is to develop a method that can characterize the driving pulse that generates the HHG right at the location where the harmonics are generated, i.e., in-situ, rather than measuring the driving pulses before they enter the vacuum chamber, using an independent (and usually complex) setup. It was previously mentioned that HHG generates odd multiples of the driving pulse frequency, and often, only the most upshifted frequencies are used. From earlier works [157], it is expected that the HHG spectra show a dependence on the properties of the driving pulse, and so, a manipulation of the driving pulse dispersion should lead to a variation in the HHG spectra. This is the cornerstone of the in-situ THG d-scan method, which is the measurement of the first odd order harmonic (the third-harmonic) as a function of the driving pulse dispersion. This work is different to the previous work on THG d-scan [158, 101], since the pulse characterization implies the creation and subsequent measurement of a THG signal, while in the case of the in-situ THG d-scan, the third-harmonic signal is already available through the HHG process and in-situ. The obtained results are compared with results obtained from SEA-F-SPIDER [73] measurements of the driving pulse before entering the vacuum chamber.

7.3 Experimental setup

The experimental setup for the hollow-core fiber and vacuum chamber at Imperial College (where the experimental part of the work was performed) is detailed in [144]. The simplified schematic of the THG d-scan experimental setup is shown in Figure 7.1. Pulses from a differentially-pumped HCF (pumped by 1 kHz, sub-25-fs pulses from a Ti:Sapphire amplifier at 800 nm) hollow-core fiber are compressed in a double-angle chirped mirror (550-1000 nm) and wedge compressor, resulting in ~200-µJ pulses with a sub-4-fs Fourier-limited duration. The pulses enter a vacuum chamber, where they are steered into a concave mirror used to focus the beam into a small opening located in a gas flow tube, where high-harmonics are generated (either in argon or neon). The high-harmonics as well as the residual fundamental pulse are picked-off by a movable Al mirror, exiting the chamber. While the higher harmonics are absorbed by the chamber window, the THG and the fundamental signal are not. Finally, the fundamental and THG signal can be separated by a prism pair setup that blocks the fundamental beam (see Figure 7.2), allowing us measure only the THG spectrum as a function of the wedge insertion.

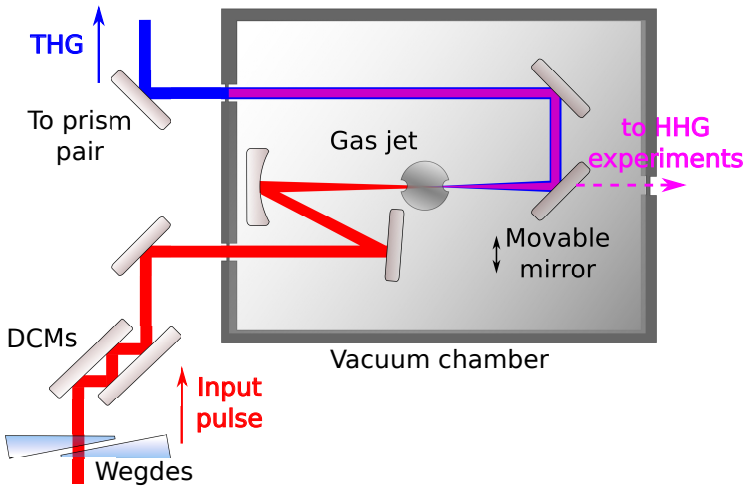

Figure 7.1: HHG setup; (red) input pulse, (blue) THG signal, (purple) full HHG beam.

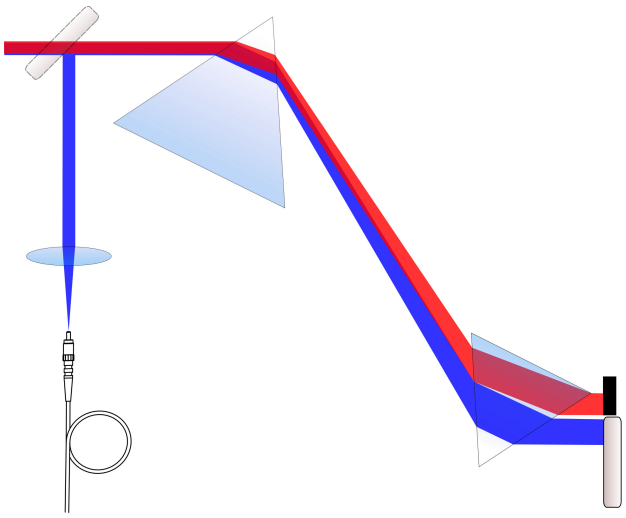

Figure 7.2: Spectral separation of fundamental (red) and third-harmonic (blue) via prism-pair.

7.4 Results and discussion

The measured and retrieved THG d-scan traces obtained for argon by measuring the generated THG spectrum as a function of wedge insertion (dispersion) are shown in Figure 7.3. We see that most of the attributes of the measured trace are reproduced in the retrieved trace, though there are some additional features not accounted for, such as the additional spectrum at insertion which produces minimum signal (close to max-

imum compression, $\simeq$ 3 mm insertion in the photo). The difference in our case is that the THG spectrum generated in the HHG process may not be completely modeled by a perturbative nonlinear-optics approach, i.e., describing the generated nonlinear electric field E_{THG} as the cube [159] of the input electric field E,

$$E_{THG}(t) \propto E^3(t) \tag{7.3}$$

Other factor that could explain the extra nonlinear spectrum is the onset of self-phase modulation (SPM) and/or plasma blueshift. Nevertheless, and despite using this non-perturbative model, the main features as well as the zones in the trace with higher signal are well reproduced, and so, we can consider these effects to be negligible, which is also corroborated by the low achieved d-scan error of 0.005 in the retrieval trace for a trace size of 128 x 768 along the insertion and wavelength axes, respectively.

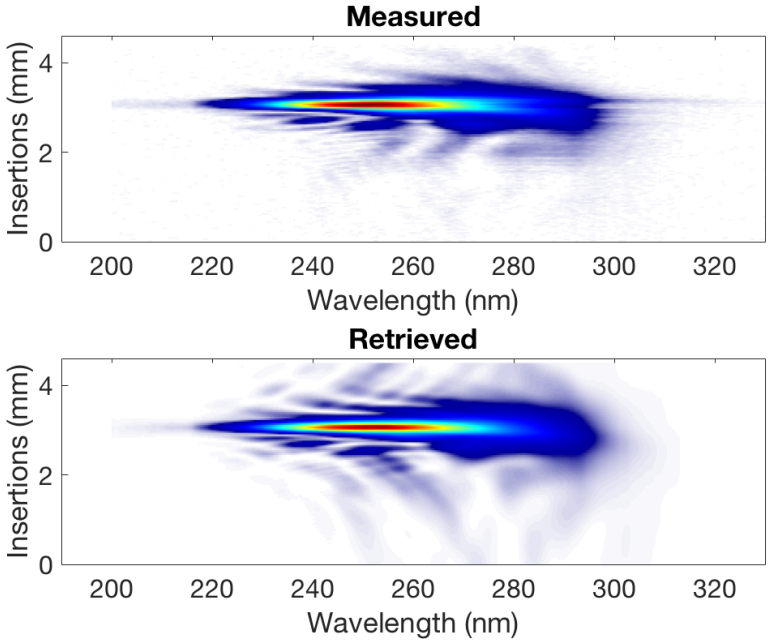

Figure 7.3: In-situ THG d-scan traces made with argon.

The retrieved spectral phase is depicted in Figure 7.4, and is compared to the one obtained with SEA-F-SPIDER [144], yielding an overall good agreement. The standard deviation of the spectral phase retrieved by THG d-scan was multiplied by a factor of 10 to make it easier to visualize.

Figure 7.5 shows the corresponding pulses in the time domain, where an excellent

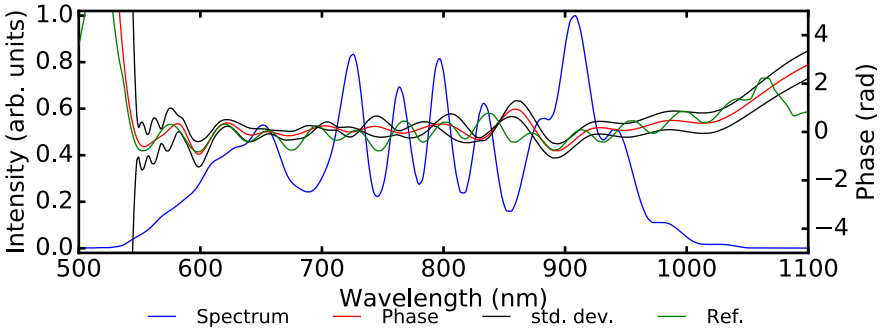

Figure 7.4: Spectrum (blue) and spectral phase of the retrieved pulse obtained with THG d-scan (red) in argon. Spectral phase standard deviation (multiplied by a factor of 10) in black. Spectral phase retrieved by SEA-F-SPIDER, labeled as “reference”.

agreement between SEA-F-SPIDER and d-scan is observed, down to the pre- and post-pulse structure at below 4% of the peak intensity. Measured FWHM pulse durations were 3.8 fs for SEA-F-SPIDER and 3.9±0.1 fs for THG d-scan. This agreement between two independent measurements of a sub-4-fs pulse, made with very different techniques based on different order nonlinear optical effects taking place in very different media (SFG in a crystal for SEA-F-SPIDER; THG in a gas for d- scan) further attests to the accuracy and precision of the method.

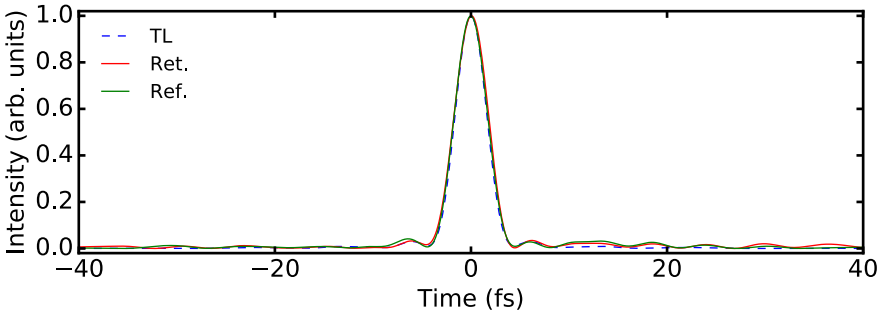

Figure 7.5: Pulse retrieved by THG d-scan in argon, with pulse duration of 3.9 fs. TL pulse 3.6 fs and reference pulse (SEA-F-SPIDER) 3.8 fs.

As for neon, the measured and retrieved traces are shown in Figure 7.6.

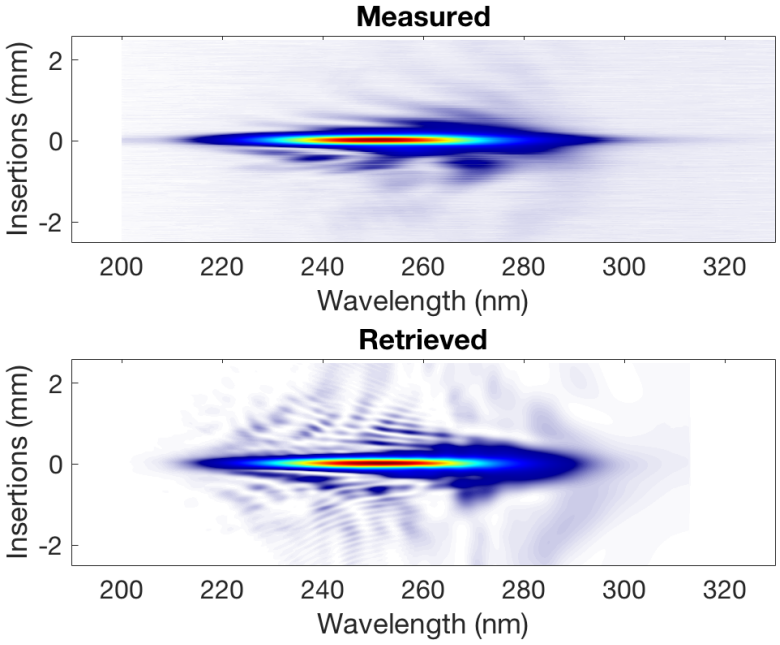

Figure 7.6: In-situ THG d-scan traces in neon. Top) measured. Bottom) retrieved.

The retrieved spectral phase is depicted in Figure 7.7, and is compared to the one obtained with SEA-F-SPIDER, yielding an overall good agreement. The d-scan error is 0.004 for the retrieval of a trace of size 128 x 768 along the insertion and wavelength axes, respectively.

The results in neon are comparable to the results in argon, although with a larger standard deviation due to weaker THG in neon.

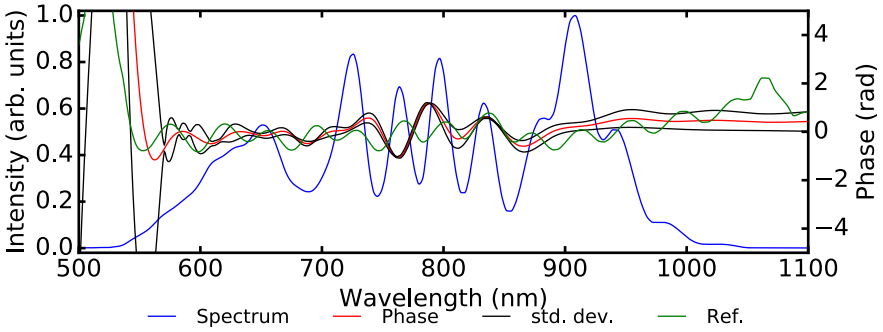

Figure 7.7: Spectrum and spectral phase of the retrieved pulse obtained with THG d-scan (red) in neon. Spectral phase standard deviation (multiplied by a factor of 3) in black. Spectral phase retrieved by SEA-F-SPIDER, labeled as “reference”.

The reconstructed pulses are shown in Figure 7.8.

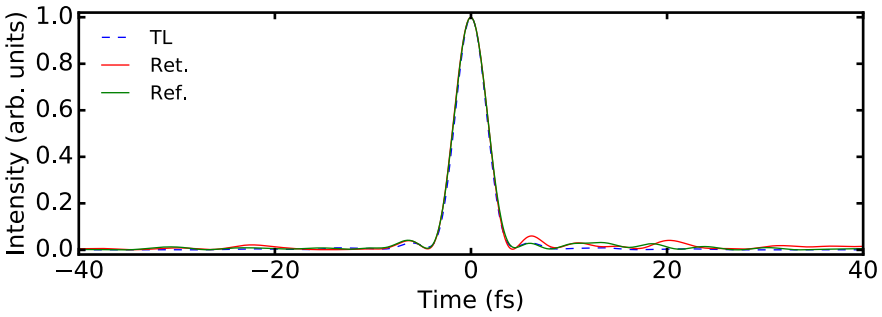

Figure 7.8: Pulse retrieved by THG d-scan in neon, with pulse duration of 3.9 fs. TL pulse 3.6 fs and reference pulse (SEA-F-SPIDER) 3.8 fs.

The pulse duration was found to be 3.8 $\pm$ 0.1 fs, again in close agreement with the result from SEA-F-SPIDER.

7.5 Conclusion

The in-situ THG d-scan technique provides knowledge of the driving pulse right in the place where the higher harmonics are generated and does not require additional components apart from the prism pair for spectral separation and a spectrometer, demonstrating that an optical characterization of the pulse driving HHG can be simple, and accurate compared to alternatives such as attosecond streaking [160]. We believe that, as part of future work, the in-situ THG d-scan retrieval algorithm can be further improved by taking into account the effects of SPM.

8 Conclusions and future work

"Goodbye, goodbye little cookie
Me always remember just you
Goodbye, goodbye little cookie
It now time to bid you adieu"

Cookie monster - 'Goodbye Little Cookie' song

Over the course of my doctoral research activity, it has been possible to bring forward new conceptual and experimental developments on the dispersion-scan technique. This technique is very suitable to the precise temporal characterization of broadband light pulses, with both low or high energy per pulse, and we have implemented new variants over different relevant spectral ranges.

A new dispersion-scan variant based on the third-order self-diffraction effect was successfully demonstrated to characterize high-energy pulses with spectra around 800 nm generated from a hollow-core fiber compressor and compared with the established SHG-based variant. This paves the way to employing the technique for measuring few-cycle laser pulses over any optical spectral range, namely from the mid-infrared to the deep-ultraviolet (the latter lacking adequate systems for producing and detecting an SHG signal), since SD is a wavelength-degenerate nonlinear process, and having a spectrometer to spectrally characterize the light source assures that an SD d-scan trace can also be recorded and hence a temporal characterization can be performed, provided that there is a dispersion-changing block in the desired spectral zone.

New sources of few-cycle laser pulses based on nonlinear optical propagation in bulk media have also been devised, which show promise for scaling the present energy limitations of pulse compression schemes based on guided propagation and may enable extending few-cycle pulse generation and application to present-day multi-terawatt and petawatt laser systems, which should have impact in a number of fields, from laser-particle acceleration to coherent ultrafast x-ray pulse generation. A new supercontinuum generation procedure taking place in a set of unequally spaced thin glass plates, multi-plate continuum (MPC), was explored and temporally characterized by SHG d-scan. Additionally, few-cycle MPC-compressed pulses were generated starting from a relatively

long pulse, higher energy laser system, with ~120 fs of duration, using a single-shot d-scan variant. The complete scalar field of the compressed pulses was also spatio-temporally and spatio-spectrally characterized with the STARFISH technique, yielding vital information for determining its focusability both in space and in time. This information, if used as input for laser-matter simulation codes, will enable a deeper understanding of high intensity laser-matter interaction experiments, and may form the basis of novel, beam and pulse shaping schemes aimed at coherent control of such interactions. The flexibility of the SD d-scan technique to be applied in different spectral ranges was used to obtain the very first self-diffraction d-scan measurement of UV pulses generated by multi-plate continuum around the second-harmonic of a Ti:Sapphire laser amplifier. Here we were able to further improve the technique by accommodating the characterization of spatially spectrally inhomogeneous beams by simultaneously retrieving two pulses from different spatial portions of the beam for the first time, without any simplifying assumptions.

A d-scan variant based on third-harmonic generation (THG) of intense laser pulses, where the nonlinear THG signal was directly produced in the same gas jet used for high-harmonic generation experiments, enabled the temporal characterization of the electric field of the employed intense 4-fs pulses, in excellent agreement with independent measurements based on a much more complex SEA-F-SPIDER setup. THG d-scan in gas jets effectively provides an unprecedentedly simple, in-situ method for measuring intense few-cycle laser pulse on focus and on target, and has enabled answering the question of what actually happens to an intense laser pulses as during extreme and non-perturbative nonlinear optical interactions such as high-harmonic generation. The performed work also points to new and interesting future directions, comprising the demonstration of the performance of SD d-scan over other spectral ranges (such as the increasingly important mid-infrared region), the improvement of the spatial homogeneity of beams generated by MPC, towards a petawatt level laser pulse source, and the application of THG d-scan to on-target pulse shaping and coherent control in high-intensity laser physics experiments.

Annex 1 - Sign conventions

In this annex are shown some tables, compiled from different sources, that introduces the different possible sign conventions for the representation of a ultrashort laser pulse and its propagation. Each known convention is then briefly discussed in the following text.

	Weiner/Diels	Trebino / LR (left-right)	RL (right-left)
$\tilde{E}(\omega)$ field	$\tilde{E}(\omega) = \lvert\tilde{E}(\omega)\rvert exp(i\psi(\omega))$	$\tilde{E}(\omega) = \lvert\tilde{E}(\omega)\rvert exp(-i\varphi(\omega))$	$\tilde{E}(\omega) = \lvert\tilde{E}(\omega)\rvert exp(i\varphi(\omega))$
Spectral phase	$\psi(\omega) = arctan\left(\frac{Im(\tilde{E}(\omega))}{Re(\tilde{E}(\omega))}\right)$	$\varphi(\omega) = -arctan\left(\frac{Im(\tilde{E}(\omega))}{Re(\tilde{E}(\omega))}\right)$	$\varphi(\omega) = arctan\left(\frac{Im(\tilde{E}(\omega))}{Re(\tilde{E}(\omega))}\right)$
n-th dispersion	$-\frac{\partial^{(n)}\psi}{\partial\omega^n}$	$\frac{\partial^{(n)}\varphi(\omega)}{\partial\omega^n}$	$\frac{\partial^{(n)}\varphi(\omega)}{\partial\omega^n}$
Propagation factor	$exp\{-izk(\omega)\}$	$exp\{-izk(\omega)\}$	$exp\{izk(\omega)\}$
Phase after prop.	$\psi'(\omega) = \psi(\omega) - zk(\omega)$	$\varphi'(\omega) = \varphi(\omega) + zk(\omega)$	$\varphi'(\omega) = \varphi(\omega) + zk(\omega)$

Table 4: Sign conventions in frequency domain.

	Weiner/Diels	Trebino / LR (left-right)	RL (right-left)
$E(t)$ field	$E(t) = \lvert E(t)\rvert exp(i\phi(t))$	$E(t) = \lvert E(t)\rvert exp(-i\phi(t))$	$E(t) = \lvert E(t)\rvert exp(i\phi(t))$
Phase	$\phi(t) = arctan\left(\frac{Im(E(t))}{Re(E(t))}\right)$	$\phi(t) = -arctan\left(\frac{Im(E(t))}{Re(E(t))}\right)$	$\phi(t) = arctan\left(\frac{Im(E(t))}{Re(E(t))}\right)$

Table 5: Sign conventions in time domain.

Sign conventions

When dealing with wave phenomena, one must abide by a sign convention in order to obtain a physically meaningful result and interpretation. The sign convention adopted in this thesis (LR) is different from the convention used in the majority of dispersion scan publications (RL), but both are consistent notations. In this chapter we will briefly describe the possible sign conventions.

Field propagation

Let us now consider the linear propagation of a ultrashort pulse through media. We define the electric field $E(t)$ as

$$E(t) = A(t)e^{i\omega_0 t} \tag{8.1}$$

where $A(t)$ is the electric field amplitude and $e^{i\omega_0 t}$ is the oscillating term containing the center frequency ω_0. The Fourier and inverse Fourier transform are defined as follows,

$$\tilde{E}(\omega) = \int_{-\infty}^{+\infty} E(t)e^{-i\omega t}dt \tag{8.2}$$

$$E(t) = \int_{-\infty}^{+\infty} \tilde{E}(\omega)e^{i\omega t}d\omega \tag{8.3}$$

This choice for $E(t)$ allows us to represent its Fourier transform, $\tilde{E}(\omega)$, centered at $+\omega_0$.

Let us consider a propagation through a finite thickness of glass ($z > 0$), where z is the glass thickness. We can either have a pulse propagating from the left to the right (LR) with the glass placed to its right, or we can have a pulse propagating from right to left (RL) with the glass placed to its left as shown in Figure 8.1.

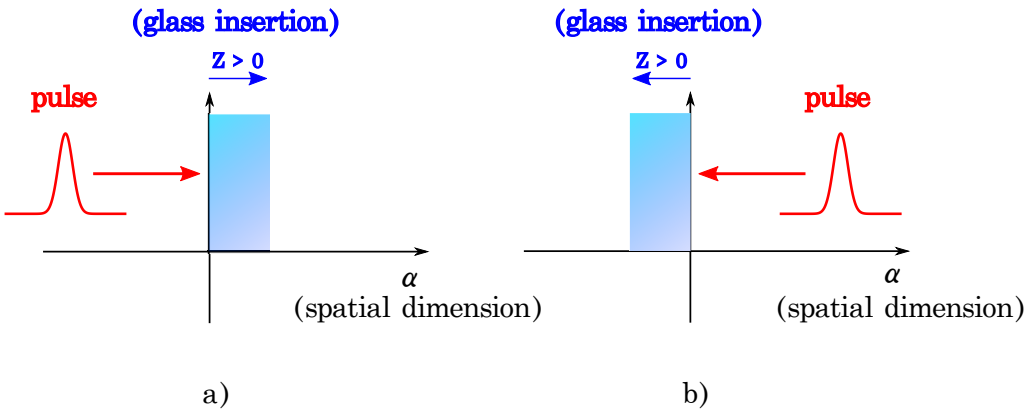

Figure 8.1: LR and RL propagation. Details in text.

Based on purely physical reasoning and regardless of the sign convention, LR or RL, the outcome is the same, a delayed pulse with positive chirp. Should we use LR, then we have a spatial propagation from left to right along the spatial axis α (cf. Figure 8.1), and a delayed pulse in time (t axis) along with positive chirp, with a cumulative phase of $\varphi'(\omega) = \varphi(\omega) + zk(\omega)$.

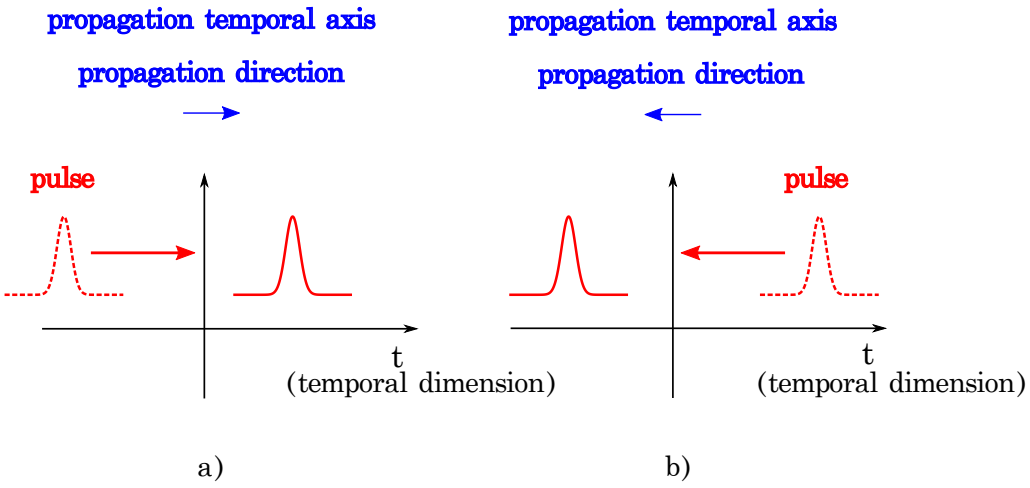

Figure 8.2: LR and RL propagation in time domain. Details in text.

The electric field is then calculated via inverse Fourier transform,

$$\int_{-\infty}^{+\infty} \tilde{E}_{LR}(\omega) e^{i\omega t} d\omega = E(t) \tag{8.4}$$

Should we choose RL instead, we have a pulse propagating from right to left in the spatial axis, a cumulative phase of $\varphi'(\omega) = \varphi(\omega) + zk(\omega)$ (exactly the same as in the LR

case), and a delayed pulse in the temporal axis, t' , that accompanies the propagation [the more it propagates, the more (positive) time it should take from the first edge of the glass to the end edge of the glass], which in our case is the opposite of the previous time axis, t, in other words, $t' = -t$, rather than $t' = t$ in the LR case (cf. Figure 8.2). If we attempt to use the inverse Fourier transform in this case, we have

$$\int_{-\infty}^{+\infty} \tilde{E}_{RL}(\omega) e^{i\omega t} d\omega = \int_{-\infty}^{+\infty} \tilde{E}^*_{LR}(\omega) e^{i\omega t} d\omega = \left(\int_{-\infty}^{+\infty} \tilde{E}_{LR}(\omega) e^{-i\omega t} d\omega \right)^* = E^*(-t) \quad (8.5)$$

$$E^*(-t) \rightarrow |E^*(-t)|^2 = I(-t) = I(t') \quad (8.6)$$

Both previous equations seem to reinforce that the time axis where the propagation is taking place is t', but we still get the intended results, apart from a trivial conjugation. We can, of course change, the time axis t' to a more convenient one t. This change of axis can be accomplished by using the Fourier transform, as follows,

$$\int_{-\infty}^{+\infty} \tilde{E}_{RL}(\omega) e^{-i\omega t} d\omega = \int_{-\infty}^{+\infty} \tilde{E}^*_{LR}(\omega) e^{-i\omega t} d\omega = \left(\int_{-\infty}^{+\infty} \tilde{E}_{LR}(\omega) e^{i\omega t} d\omega \right)^* = E^*(t)$$

Doing the trivial conjugation $E^*(t) \rightarrow E(t)$ recasts the obtained propagation in the preferred time axis, t.

The Weiner sign convention can be regarded as a slight variation of the Trebino/LR convention, this can be easily understood with an example. Suppose (using LR convention) a pulse with a spectral phase of $\varphi(\omega) = 100 \times (\omega - \omega_0)^3$, i.e., with TOD = 100 fs^3 and a central (radial) frequency at ω_0. After propagation through a length , L, of glass, the argument of the exponential function $\tilde{E}(\omega) = \left|\tilde{E}(\omega)\right| exp(-i\varphi'(\omega))$, is $-\varphi'(\omega) = -\left[100 \times (\omega - \omega_0)^3 + k(\omega) \times L\right]$. The imaginary unit was omitted for simplicity.

Now, using the inverse Fourier transform on $\tilde{E}(\omega) = \left|\tilde{E}(\omega)\right| exp(-i\varphi'(\omega))$ we obtain the correct time domain behavior, a pulse with a series of post-pulses.

Consider now, the same pulse but in Weiner notation. Since in this case the dispersion terms are calculated with an additional minus sign, in order to simulate the same pulse as in the Trebino/LR case, we must also introduce a minus sign in the phase (in other words $\psi_{weiner}(\omega) = -\varphi_{trebino}(\omega)$). Thus the spectral phase for Weiner's case becomes, $\psi(\omega) = -100 \times (\omega - \omega_0)^3$. With further propagation through glass, the cumulative spectral phase is $\psi'(\omega) = -\left[100 \times (\omega - \omega_0)^3 + k(\omega) \times L\right]$, which coincides with the argument of

of the exponential in $\tilde{E}(\omega) = \left|\tilde{E}(\omega)\right| exp(i\psi'(\omega))$. Since $\psi'(\omega)$ and $-\varphi'(\omega)$ are numerically equal, their inverse Fourier transform of the $\tilde{E}(\omega)$ field yields the same result, $E(t)$.

Alternative field propagation formulation

The previous representation of the electric field is not unique, as the electric field can also be represented with an oscillating term containing a minus sign. Let us now consider the linear propagation of a ultrashort pulse through media, where

$$E(t) = A(t)e^{-i\omega_0 t} \tag{8.7}$$

where $A(t)$ is the electric field amplitude and $e^{-i\omega_0 t}$ is the oscillating term containing the center frequency ω_0. The choice of the minus sign in the oscillating term prompt us to the redefinition of the Fourier and inverse Fourier transform, as follows

$$\tilde{E}(\omega) = \int_{-\infty}^{+\infty} E(t)e^{i\omega t}dt \tag{8.8}$$

$$E(t) = \int_{-\infty}^{+\infty} \tilde{E}(\omega)e^{-i\omega t}d\omega \tag{8.9}$$

This redefinition of transforms, allows us to maintain $\tilde{E}(\omega)$ centered at $+\omega_0$. This choice of sign convention can be seen in, e.g., R. Alfano's book [109]. We are again faced with the same scenario as depicted in Figure 8.1.

Adopting a propagation factor of $exp(+izk(\omega))$ implies a translation along the spatial axis α(from left to right), i.e., the pulse gets delayed in time and acquires positive chirp. Hence, $\tilde{E}(\omega)$ can be represented as $\tilde{E}(\omega) = \left|\tilde{E}(\omega)\right| exp(i\varphi'(\omega))$, where $\varphi'(\omega) = \varphi(\omega) + zk$ is the cumulative spectral phase. The propagation factor $exp(-izk(\omega))$ describes a pulse traveling from right to left along the spatial axis which gets delayed in time along the time axis that follows the pulse propagation, i.e., $t' = -t$, and acquires positive chirp as well. The cumulative spectral phase remains the same, $\varphi'(\omega) = \varphi(\omega) + zk$. To recast the results in the original time axis, t, we employ the same procedure described in the previous section.

Annex 2

Laser systems and equipment in Femtolab

We have a custom sub-30fs FemtoPower Compact PRO CEP laser amplifier (Femtolasers) with ~1 mJ of energy at a repetition rate of 1 kHz (as shown[8] in Figure 8.3 in the next page), seeded by a sub-8fs, 180 mW oscillator (Rainbow, Femtolasers) with a repetition rate of 80 MHz. A homemade hollow-core fiber (200 μm in diameter) is also available for pulse broadening and further compression with a set of PC70 (Ultrafast Innovations) DCMs.

An Ocean Optics HR4000 spectrometer is used for spectral measurements. A broadband Melles Griot power/energy meter, model 13PEM001, is used for power measurements.

[8] "FEMTOPOWER compact pro CE-PHASE, Femtosecond Multi-pass Amplifier User's manual, version 3.2".

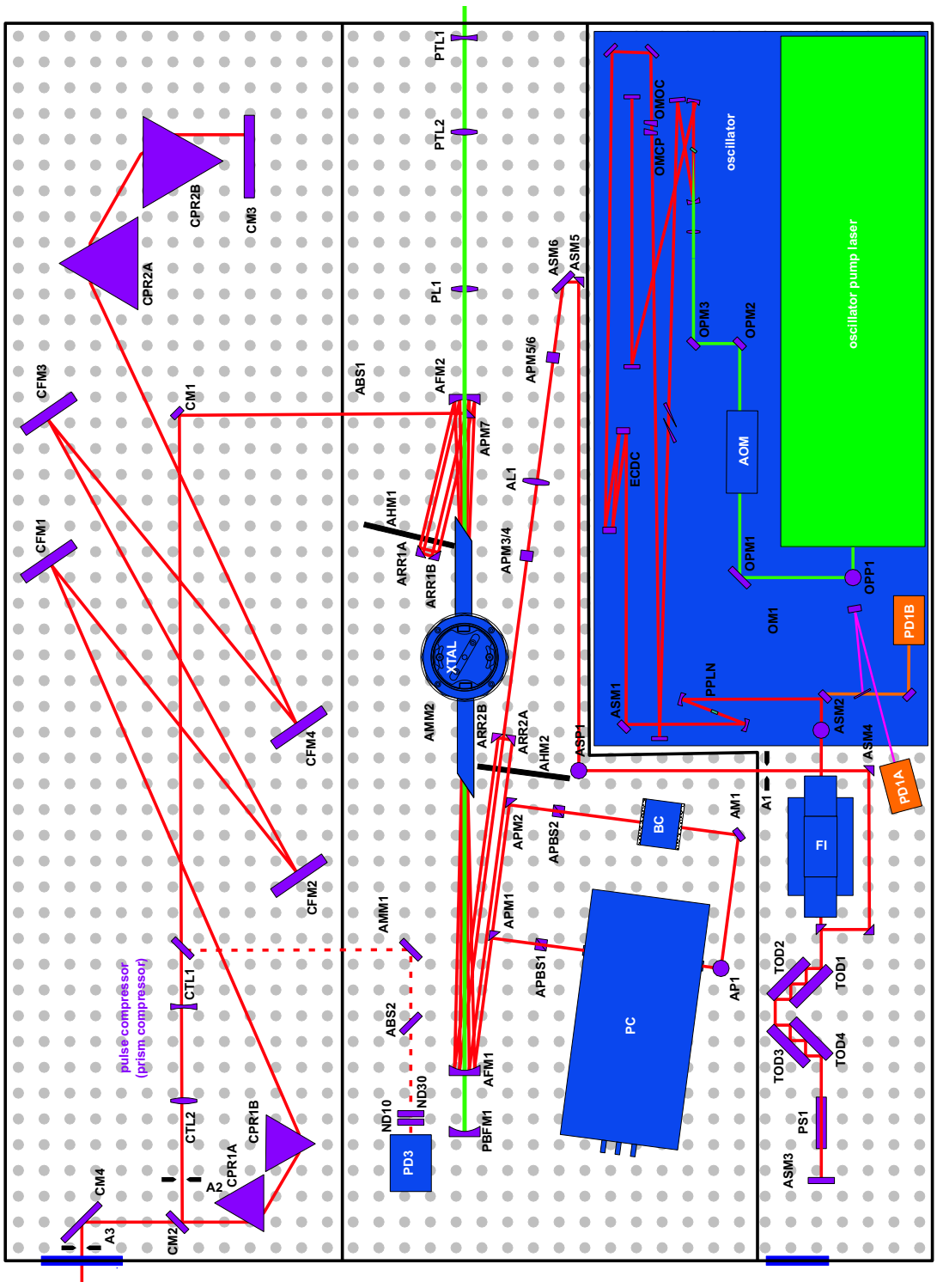

Figure 8.3: FEMTOPOWER optical layout.

References

[1] L. Cohen, *Time-frequency Analysis*. Electrical engineering signal processing, Prentice Hall PTR, 1995.

[2] R. L. Allen and D. Mills, *Signal Analysis: Time, Frequency, Scale, and Structure*. Wiley, 2004.

[3] F. Träger, ed., *Springer Handbook of Lasers and Optics*. New York, NY: Springer New York, 2007.

[4] O. Svelto, *Principles of Lasers*. Springer, 2009.

[5] C. Rullière, *Femtosecond laser pulses: principles and experiments*. Advanced texts in physics, Springer, 2005.

[6] D. E. Spence, P. N. Kean, and W. Sibbett, "60-fsec pulse generation from a self-mode-locked Ti:sapphire laser," *Opt. Lett.*, vol. 16, p. 42, jan 1991.

[7] C. B. Harris, E. P. Ippen, G. A. Mourou, and A. H. Zeweil, *Ultrafast Phenomena VII: Proceedings of the 7th International Conference, Monterey, CA, May 14–17, 1990*. Springer Series in Chemical Physics, Springer Berlin Heidelberg, 1990.

[8] A. E. Siegman, *Lasers*. University Science Books, 1986.

[9] T. Brabec, C. Spielmann, P. F. Curley, and F. Krausz, "Kerr lens mode locking," *Opt. Lett.*, vol. 17, p. 1292, sep 1992.

[10] S. Yefet and A. Pe'er, "A Review of Cavity Design for Kerr Lens Mode-Locked Solid-State Lasers," *Appl. Sci.*, vol. 3, no. 4, pp. 694–724, 2013.

[11] F. S. Brightbill, *Corneal Surgery: Theory, Technique and Tissue*. ClinicalKey 2012, Mosby/Elsevier, 2009.

[12] J. Meijer, K. Du, A. Gillner, D. Hoffmann, V. Kovalenko, T. Masuzawa, A. Ostendorf, R. Poprawe, and W. Schulz, "Laser Machining by short and ultrashort pulses, state of the art and new opportunities in the age of the photons," *CIRP Ann.*, vol. 51, no. 2, pp. 531–550, 2002.

[13] T. Baldacchini, J. E. Carey, M. Zhou, and E. Mazur, "Superhydrophobic Surfaces Prepared by Microstructuring of Silicon Using a Femtosecond Laser," *Langmuir*, vol. 22, pp. 4917–4919, may 2006.

[14] C. S. Gonçalves, A. S. Silva, D. Navas, M. Miranda, F. Silva, H. Crespo, and D. S. Schmool, "A Dual-Colour Architecture for Pump-Probe Spectroscopy of Ultrafast Magnetization Dynamics in the Sub-10-femtosecond Range," *Sci. Rep.*, vol. 6, no. October 2015, p. 22872, 2016.

[15] H.-T. Chang, M. Zürch, P. M. Kraus, L. J. Borja, D. M. Neumark, and S. R. Leone, "Simultaneous generation of sub-5-femtosecond 400 nm and 800 nm pulses for attosecond extreme ultraviolet pump–probe spectroscopy," *Opt. Lett.*, vol. 41, p. 5365, nov 2016.

[16] T. Udem, R. Holzwarth, and T. W. Hänsch, "Optical frequency metrology.," *Nature*, vol. 416, pp. 233–7, mar 2002.

[17] S. T. Cundiff and J. Ye, "Colloquium : Femtosecond optical frequency combs," *Rev. Mod. Phys.*, vol. 75, pp. 325–342, mar 2003.

[18] M. Dunne, "APPLIED PHYSICS: Laser-Driven Particle Accelerators," *Science (80-.).*, vol. 312, pp. 374–376, apr 2006.

[19] K.-L. Yeh, M. C. Hoffmann, J. Hebling, and K. A. Nelson, "Generation of 10μJ ultrashort terahertz pulses by optical rectification," *Appl. Phys. Lett.*, vol. 90, p. 171121, apr 2007.

[20] K. Takeya, K. Okimura, K. Oota, K. Kawase, and H. Uchida, "Pump wavelength-independent broadband terahertz generation from a nonlinear optical crystal," *Opt. Lett.*, vol. 43, p. 4100, sep 2018.

[21] M. Ferray, A. L'Huillier, X. F. Li, L. A. Lompre, G. Mainfray, and C. Manus, "Multiple-harmonic conversion of 1064 nm radiation in rare gases," *J. Phys. B At. Mol. Opt. Phys.*, vol. 21, pp. L31–L35, feb 1988.

[22] R. Samad, L. Courrol, S. Baldochi, and N. Vieir, "Ultrashort Laser Pulses Applications," in *Coherence Ultrashort Pulse Laser Emiss.*, InTech, nov 2010.

[23] R. W. Boyd, *Nonlinear Optics*. Academic Press, Academic Press, 2008.

[24] G. New, *Introduction to Nonlinear Optics*. Introduction to Nonlinear Optics, Cambridge University Press, 2011.

[25] P. E. Powers and J. W. Haus, *Fundamentals of Nonlinear Optics, Second Edition*. CRC Press, 2017.

[26] C. Chen, Y. Wu, A. Jiang, B. Wu, G. You, R. Li, and S. Lin, "New nonlinear-optical crystal: LiB_3O_5," *J. Opt. Soc. Am. B*, vol. 6, p. 616, apr 1989.

[27] H. Telle, G. Steinmeyer, A. Dunlop, J. Stenger, D. Sutter, and U. Keller, "Carrier-envelope offset phase control: A novel concept for absolute optical frequency measurement and ultrashort pulse generation," *Appl. Phys. B*, vol. 69, pp. 327–332, oct 1999.

[28] A. Apolonski, A. Poppe, G. Tempea, C. Spielmann, T. Udem, R. Holzwarth, T. W. Hänsch, and F. Krausz, "Controlling the phase evolution of few-cycle light pulses," *Phys. Rev. Lett.*, vol. 85, no. 4, pp. 740–743, 2000.

[29] J. Ye and S. T. Cundiff, *Femtosecond optical frequency comb: principle, operation, and applications*. Springer, 2005.

[30] E. Treacy, "Optical pulse compression with diffraction gratings," *IEEE J. Quantum Electron.*, vol. 5, pp. 454–458, sep 1969.

[31] R. L. Fork, O. E. Martinez, and J. P. Gordon, "Negative dispersion using pairs of prisms.," *Opt. Lett.*, vol. 9, pp. 150–2, may 1984.

[32] A. Johnson and W. Simpson, "Optically biased tunable femtosecond dye laser and spectral windowing of the compressed second harmonic of Nd:YAG," *IEEE J. Quantum Electron.*, vol. 22, pp. 133–141, jan 1986.

[33] J. D. Kafka and T. Baer, "Prism-pair dispersive delay lines in optical pulse compression.," *Opt. Lett.*, vol. 12, no. 6, pp. 401–403, 1987.

[34] R. L. Fork, C. H. Cruz, P. C. Becker, and C. V. Shank, "Compression of optical pulses to six femtoseconds by using cubic phase compensation.," *Opt. Lett.*, vol. 12, pp. 483–5, jul 1987.

[35] R. Szipöcs, C. Spielmann, F. Krausz, K. Ferencz, R. Szipocs, K. Ferencz, C. Spielmann, and F. Krausz, "Chirped multilayer coatings for broadband dispersion control in femtosecond lasers," *Opt. Lett.*, vol. 19, p. 201, feb 1994.

[36] G. Steinmeyer, "Frontiers in Ultrashort Pulse Generation: Pushing the Limits in Linear and Nonlinear Optics," *Science (80-.).*, vol. 286, pp. 1507–1512, nov 1999.

[37] V. Pervak, I. Ahmad, M. K. Trubetskov, A. V. Tikhonravov, and F. Krausz, "Double-angle multilayer mirrors with smooth dispersion characteristics," *Opt. Express*, vol. 17, p. 7943, may 2009.

[38] F. X. Kärtner, U. Morgner, R. Ell, T. Schibli, J. G. Fujimoto, E. P. Ippen, V. Scheuer, G. Angelow, and T. Tschudi, "Ultrabroadband double-chirped mirror pairs for generation of octave spectra," *J. Opt. Soc. Am. B*, vol. 18, p. 882, jun 2001.

[39] G. Steinmeyer, "Femtosecond dispersion compensation with multilayer coatings: toward the optical octave," *Appl. Opt.*, vol. 45, p. 1484, mar 2006.

[40] S.-H. Chia, G. Cirmi, S. Fang, G. M. Rossi, O. D. Mücke, and F. X. Kärtner, "Two-octave-spanning dispersion-controlled precision optics for sub-optical-cycle waveform synthesizers," *Optica*, vol. 1, p. 315, nov 2014.

[41] O. R. Azskazovskaya, F. K. Rausz, O. Razskazovskaya, F. Krausz, and V. Pervak, "Multilayer coatings for femto- and attosecond technology," *Optica*, vol. 4, p. 129, jan 2017.

[42] D. Strickland and G. Mourou, "Compression of amplified chirped optical pulses," *Opt. Commun.*, vol. 56, no. 3, pp. 219–221, 1985.

[43] J. A. Armstrong, "Measurement of picosecind laser pulse widths," *Appl. Phys. Lett.*, vol. 10, pp. 16–18, jan 1967.

[44] K. Sala, G. Kenney-Wallace, and G. Hall, "CW autocorrelation measurements of picosecond laser pulses," *IEEE J. Quantum Electron.*, vol. 16, pp. 990–996, sep 1980.

[45] W. R. Diels, Jean-Claude, *Ultrashort Laser Pulse Phenomena. Fundamentals, Techniques, and Applications on a Femtosecond Time Scale*.

[46] Jung-Ho Chung and A. Weiner, "Ambiguity of ultrashort pulse shapes retrieved from the intensity autocorrelation and the power spectrum," *IEEE J. Sel. Top. Quantum Electron.*, vol. 7, no. 4, pp. 656–666, 2001.

[47] D. Kane and R. Trebino, "Characterization of arbitrary femtosecond pulses using frequency-resolved optical gating," *IEEE J. Quantum Electron.*, vol. 29, no. 2, pp. 571–579, 1993.

[48] R. Trebino, *Frequency-Resolved Optical Gating: The Measurement of Ultrashort Laser Pulses*. Kluwer Academic, 2000.

[49] R. Trebino and D. J. Kane, "Using phase retrieval to measure the intensity and phase of ultrashort pulses: frequency-resolved optical gating," *J. Opt. Soc. Am. A*, vol. 10, p. 1101, may 1993.

[50] K. W. DeLong, B. Kohler, K. Wilson, D. N. Fittinghoff, and R. Trebino, "Pulse retrieval in frequency-resolved optical gating based on the method of generalized projections," *Opt. Lett.*, vol. 19, p. 2152, dec 1994.

[51] D. J. Kane, "Recent progress toward real-time measurement of ultrashort laser pulses," *IEEE J. Quantum Electron.*, vol. 35, no. 4, pp. 421–431, 1999.

[52] D. J. Kane, "Principal components generalized projections: a review [Invited]," *J. Opt. Soc. Am. B*, vol. 25, p. A120, may 2008.

[53] C. Iaconis and I. A. Walmsley, "Spectral phase interferometry for direct electric-field reconstruction of ultrashort optical pulses," *Opt. Lett.*, vol. 23, p. 792, may 1998.

[54] C. Iaconis and I. Walmsley, "Self-referencing spectral interferometry for measuring ultrashort optical pulses," *IEEE J. Quantum Electron.*, vol. 35, pp. 501–509, apr 1999.

[55] I. A. Walmsley, "Characterization of Ultrashort Optical Pulses in the Few-Cycle Regime Using Spectral Phase Interferometry for Direct Electric-Field Reconstruction," pp. 265–292, aug 2004.

[56] G. Stibenz and G. Steinmeyer, "Optimizing spectral phase interferometry for direct electric-field reconstruction," *Rev. Sci. Instrum.*, vol. 77, no. 7, pp. 0–9, 2006.

[57] B. Xu, J. M. Gunn, J. M. D. Cruz, V. V. Lozovoy, and M. Dantus, "Quantitative investigation of the multiphoton intrapulse interference phase scan method for simultaneous phase measurement and compensation of femtosecond laser pulses," *J. Opt. Soc. Am. B*, vol. 23, no. 4, p. 750, 2006.

[58] V. V. Lozovoy, I. Pastirk, and M. Dantus, "Multiphoton intrapulse interference. IV. Ultrashort laser pulse spectral phase characterization and compensation," *Opt. Lett.*, vol. 29, no. 7, p. 775, 2004.

[59] J. R. Birge, R. Ell, and F. X. Kärtner, "Two-dimensional spectral shearing interferometry for few-cycle pulse characterization," *Opt. Lett.*, vol. 31, p. 2063, jul 2006.

[60] X. Shen, P. Wang, J. Liu, T. Kobayashi, and R. Li, "Self-Referenced Spectral Interferometry for Femtosecond Pulse Characterization," *Appl. Sci.*, vol. 7, p. 407, apr 2017.

[61] G. Stibenz and G. Steinmeyer, "Interferometric frequency-resolved optical gating," *Opt. Express*, vol. 13, no. 7, p. 2617, 2005.

[62] P. Baum, S. Lochbrunner, and E. Riedle, “Zero-additional-phase SPIDER:f ull characterization of visible and sub-20-fs ultraviolet pulses,” *Opt. Lett.*, vol. 29, p. 210, jan 2004.

[63] I. a. Walmsley and C. Dorrer, “Characterization of ultrashort electromagnetic pulses,” *Adv. Opt. Photonics*, vol. 1, no. 2, p. 308, 2009.

[64] Z. Bor, “Distortion of Femtosecond Laser Pulses in Lenses and Lens Systems,” *J. Mod. Opt.*, vol. 35, pp. 1907–1918, dec 1988.

[65] J.-C. Chanteloup, E. Salmon, C. Sauteret, A. Migus, P. Zeitoun, A. Klisnick, A. Carillon, S. Hubert, D. Ros, P. Nickles, and M. Kalachnikov, “Pulse-front control of 15-TW pulses with a tilted compressor, and application to the subpicosecond traveling-wave pumping of a soft-x-ray laser,” *J. Opt. Soc. Am. B*, vol. 17, p. 151, jan 2000.

[66] C. Dorrer and I. A. Walmsley, “Simple linear technique for the measurement of space–time coupling in ultrashort optical pulses,” *Opt. Lett.*, vol. 27, p. 1947, nov 2002.

[67] P. Bowlan, P. Gabolde, A. Shreenath, K. McGresham, R. Trebino, and S. Akturk, “Crossed-beam spectral interferometry: a simple, high-spectral-resolution method for completely characterizing complex ultrashort pulses in real time,” *Opt. Express*, vol. 14, no. 24, p. 11892, 2006.

[68] P. Gabolde and R. Trebino, “Self-referenced measurement of the complete electric field of ultrashort pulses,” *Opt. Express*, vol. 12, p. 4423, sep 2004.

[69] P. Gabolde and R. Trebino, “Single-shot measurement of the full spatio-temporal field of ultrashort pulses with multi-spectral digital holography.,” *Opt. Express*, vol. 14, no. 23, pp. 11460–11467, 2006.

[70] F. Bonaretti, D. Faccio, M. Clerici, J. Biegert, and P. Di Trapani, “Spatiotemporal Amplitude and Phase Retrieval of Bessel-X pulses using a Hartmann-Shack Sensor,” *Opt. Express*, vol. 17, p. 9804, jun 2009.

[71] E. Rubino, D. Faccio, L. Tartara, P. K. Bates, O. Chalus, M. Clerici, F. Bonaretti, J. Biegert, and P. Di Trapani, “Spatiotemporal amplitude and phase retrieval of space-time coupled ultrashort pulses using the Shackled-FROG technique,” *Opt. Lett.*, vol. 34, no. 24, p. 3854, 2009.

[72] A. S. Wyatt, I. A. Walmsley, G. Stibenz, and G. Steinmeyer, "Sub-10 fs pulse characterization using spatially encoded arrangement for spectral phase interferometry for direct electric field reconstruction," *Opt. Lett.*, vol. 31, p. 1914, jun 2006.

[73] T. Witting, F. Frank, C. A. Arrell, W. A. Okell, J. P. Marangos, and J. W. G. Tisch, "Characterization of high-intensity sub-4-fs laser pulses using spatially encoded spectral shearing interferometry," *Opt. Lett.*, vol. 36, p. 1680, may 2011.

[74] B. Alonso, Í. J. Sola, Ó. Varela, J. Hernández-Toro, C. Méndez, J. San Román, A. Zaïr, and L. Roso, "Spatiotemporal amplitude-and-phase reconstruction by Fourier-transform of interference spectra of high-complex-beams," *J. Opt. Soc. Am. B*, vol. 27, p. 933, may 2010.

[75] B. Alonso, Í. J. ÍSola, Ó. Varela, C. Méndez, I. Arias, J. S. Román, A. Zaïr, and L. Roso, "Spatio-temporal characterization of laser pulses by spatially resolved spectral interferometry," *Opt. Pura Apl.*, vol. 43, pp. 1–7, 2010.

[76] B. Alonso, M. Miranda, Í. J. Sola, and H. Crespo, "Spatiotemporal characterization of few-cycle laser pulses.," *Opt. Express*, vol. 20, pp. 17880–93, jul 2012.

[77] B. Alonso, M. Miranda, F. Silva, V. Pervak, J. Rauschenberger, J. San Román, Í. J. Sola, and H. Crespo, "Characterization of sub-two-cycle pulses from a hollow-core fiber compressor in the spatiotemporal and spatiospectral domains," *Appl. Phys. B*, vol. 112, pp. 105–114, mar 2013.

[78] M. Miranda, T. Fordell, C. Arnold, A. L'Huillier, and H. Crespo, "Simultaneous compression and characterization of ultrashort laser pulses using chirped mirrors and glass wedges," *Opt. Express*, vol. 20, p. 688, jan 2012.

[79] M. Miranda, C. L. Arnold, T. Fordell, F. Silva, B. Alonso, R. Weigand, A. L'Huillier, and H. Crespo, "Characterization of broadband few-cycle laser pulses with the d-scan technique.," *Opt. Express*, vol. 20, pp. 18732–43, aug 2012.

[80] M. Miranda, J. Penedones, C. Guo, A. Harth, M. Louisy, L. Neoričić, A. L'Huillier, and C. L. Arnold, "Fast iterative retrieval algorithm for ultrashort pulse characterization using dispersion scans," *J. Opt. Soc. Am. B*, vol. 34, p. 190, jan 2017.

[81] C. Dorrer and I. a. Walmsley, "Accuracy criterion for ultrashort pulse characterization techniques: application to spectral phase interferometry for direct electric field reconstruction," *J. Opt. Soc. Am. B*, vol. 19, p. 1019, may 2002.

[82] V. Loriot, G. Gitzinger, and N. Forget, "Self-referenced characterization of femtosecond laser pulses by chirp scan," *Opt. Express*, vol. 21, no. 21, pp. 24879–24893, 2013.

[83] F. Silva, B. Alonso, W. Holgado, R. Romero, J. S. Román, E. C. Jarque, H. Koop, V. Pervak, H. Crespo, and Í. J. Sola, "Strategies for achieving intense single-cycle pulses with in-line post-compression setups," *Opt. Lett.*, vol. 43, p. 337, jan 2018.

[84] B. Alonso, I. J. Sola, and H. Crespo, "Self-calibrating d-scan: measuring ultrashort laser pulses on-target using an arbitrary pulse compressor," sep 2017.

[85] M. Miranda, F. Silva, A. L'Huillier, and C. L. Arnold, "Ultrashort Pulse Characterization from Dispersion Scans with a Grating Compressor," in *Conf. Lasers Electro-Optics*, (Washington, D.C.), p. JTu5A.67, OSA, 2016.

[86] R. E. Sherriff, "Analytic expressions for group-delay dispersion and cubic dispersion in arbitrary prism sequences," *J. Opt. Soc. Am. B*, vol. 15, p. 1224, mar 1998.

[87] B. Alonso, Í. J. Sola, and H. Crespo, "Self-calibrating d-scan: measuring ultrashort laser pulses on-target using an arbitrary pulse compressor," *Sci. Rep.*, vol. 8, p. 3264, dec 2018.

[88] D. Fabris, W. Holgado, F. Silva, T. Witting, J. W. G. Tisch, and H. Crespo, "Single-shot implementation of dispersion-scan for the characterization of ultrashort laser pulses," *Opt. Express*, vol. 23, no. 25, p. 32803, 2015.

[89] M. Louisy, C. Guo, L. Neoričić, S. Zhong, A. L'Huillier, C. L. Arnold, and M. Miranda, "Compact single-shot d-scan setup for the characterization of few-cycle laser pulses," *Appl. Opt.*, vol. 56, p. 9084, nov 2017.

[90] F. Silva, Í. J. Sola, H. Crespo, R. Romero, M. Miranda, C. L. Arnold, A. L'Huillier, J. Trull, and C. Cojocaru, "Monolithic single-shot dispersion-scan: a new tool for real-time measurement and optimization of femtosecond pulses," in *2017 Eur. Conf. Lasers Electro-Optics Eur. Quantum Electron. Conf.*, p. CF_11_3, Optical Society of America, 2017.

[91] M. Miranda, P. Rudawski, C. Guo, F. Silva, C. L. Arnold, T. Binhammer, H. Crespo, and A. L'Huillier, "Ultrashort laser pulse characterization from dispersion scans: a comparison with SPIDER," in *CLEO 2013*, (Washington, D.C.), p. JTh2A.31, OSA, 2013.

[92] F. Silva, M. Miranda, and H. Crespo, “Measuring few-cycle laser pulses: A comparative study between dispersionscan and FROG,” in *2013 Conf. Lasers Electro-Optics Eur. Int. Quantum Electron. Conf. CLEO Eur.*, vol. 70, pp. 1–1, IEEE, may 2013.

[93] J. Rodenburg, “Ptychography and Related Diffractive Imaging Methods,” pp. 87–184, 2008.

[94] M. Dierolf, P. Thibault, A. Menzel, C. M. Kewish, K. Jefimovs, I. Schlichting, K. von König, O. Bunk, and F. Pfeiffer, “Ptychographic coherent diffractive imaging of weakly scattering specimens,” *New J. Phys.*, vol. 12, p. 035017, mar 2010.

[95] A. M. Maiden, M. J. Humphry, F. Zhang, and J. M. Rodenburg, “Superresolution imaging via ptychography,” *J. Opt. Soc. Am. A*, vol. 28, p. 604, apr 2011.

[96] A. M. Maiden and J. M. Rodenburg, “An improved ptychographical phase retrieval algorithm for diffractive imaging,” *Ultramicroscopy*, vol. 109, pp. 1256–1262, sep 2009.

[97] P. Sidorenko, O. Lahav, Z. Avnat, and O. Cohen, “Ptychographic Reconstruction Algorithm for FROG : Supreme Robustness and Super-Resolution,” vol. 3, no. m, pp. 6–7, 2016.

[98] E. Zeek, A. Shreenath, P. O’Shea, M. Kimmel, and R. Trebino, “Simultaneous automatic calibration and direction-of-time removal in frequency-resolved optical gating,” *Appl. Phys. B*, vol. 74, pp. s265–s271, jun 2002.

[99] N. X. Truong, J. Tiggesbäumker, and T. Döppner, “Shaper-assisted removal of the direction-of-time ambiguity in second-harmonic generation frequency-resolved optical gating,” *Meas. Sci. Technol.*, vol. 21, p. 085303, aug 2010.

[100] F. Silva, M. Miranda, S. Teichmann, M. Baudisch, M. Massicotte, F. Koppens, J. Biegert, and H. Crespo, “Pulse measurement from near to mid-IR using third harmonic generation dispersion scan in multilayer graphene,” in *2013 Conf. Lasers Electro-Optics Eur. Int. Quantum Electron. Conf. CLEO Eur.*, vol. 105, pp. 1–1, IEEE, may 2013.

[101] M. Hoffmann, T. Nagy, T. Willemsen, M. Jupé, D. Ristau, and U. Morgner, “Pulse characterization by THG d-scan in absorbing nonlinear media,” *Opt. Express*, vol. 22, p. 5234, mar 2014.

[102] A. Tajalli, B. Chanteau, M. Kretschmar, H. Kurz, D. Zuber, M. Kovačev, U. Morgner, and T. Nagy, "Few-cycle optical pulse characterization via cross-polarized wave generation dispersion scan technique," *Opt. Lett.*, vol. 41, p. 5246, nov 2016.

[103] A. Tajalli, M. Ouillé, A. Vernier, F. Böhle, E. Escoto, J. Csontos, R. Romero, U. Morgner, H. Crespo, R. L. Martens, G. Steinmeyer, and T. Nagy, "XPW and SHG d-scan characterization of sub-1.5-cycle pulses," in *High-Brightness Sources Light. Interact.*, p. HW3D.2, Optical Society of America, 2018.

[104] M. Canhota, F. Silva, R. Weigand, and H. M. Crespo, "Inline self-diffraction dispersion-scan of over octave-spanning pulses in the single-cycle regime," *Opt. Lett.*, vol. 42, p. 3048, aug 2017.

[105] E. Escoto, A. Tajalli, T. Nagy, and G. Steinmeyer, "Advanced phase retrieval for dispersion scan: a comparative study," *J. Opt. Soc. Am. B*, vol. 35, p. 8, jan 2018.

[106] H. Timmers, Y. Kobayashi, K. F. Chang, M. Reduzzi, D. M. Neumark, and S. R. Leone, "Generating high-contrast, near single-cycle waveforms with third-order dispersion compensation," *Opt. Lett.*, vol. 42, no. 4, p. 811, 2017.

[107] F. Silva, M. Miranda, B. Alonso, J. Rauschenberger, V. Pervak, and H. Crespo, "Simultaneous compression, characterization and phase stabilization of GW-level 1.4 cycle VIS-NIR femtosecond pulses using a single dispersion-scan setup," *Opt. Express*, vol. 22, p. 10181, may 2014.

[108] D. N. Nikogosyan, "Beta barium borate (BBO) - A review of its properties and applications," *Appl. Phys. A Solids Surfaces*, vol. 52, no. 6, pp. 359–368, 1991.

[109] R. R. Alfano, *The Supercontinuum Laser Source: The Ultimate White Light*. Springer New York, 2016.

[110] P. F. Moulton, "Ti:sapphire lasers: Out of the lab and back in again," *Opt. Photonics News*, vol. 1, p. 20, aug 1990.

[111] M. Nisoli, S. De Silvestri, and O. Svelto, "Generation of high energy 10 fs pulses by a new pulse compression technique," *Appl. Phys. Lett.*, vol. 68, no. 20, pp. 2793–2795, 1996.

[112] P. He, Y. Liu, K. Zhao, H. Teng, X. He, P. Huang, H. Huang, S. Zhong, Y. Jiang, S. Fang, X. Hou, and Z. Wei, "High-efficiency supercontinuum generation in solid thin plates at 01 TW level," *Opt. Lett.*, vol. 42, p. 474, feb 2017.

[113] C.-H. Lu, Y.-J. Tsou, H.-Y. Chen, B.-H. Chen, Y.-C. Cheng, S.-D. Yang, M.-C. Chen, C.-C. Hsu, and A. H. Kung, "Generation of intense supercontinuum in condensed media," *Optica*, vol. 1, p. 400, dec 2014.

[114] Y.-C. Cheng, C.-H. Lu, Y.-Y. Lin, and A. H. Kung, "Supercontinuum generation in a multi-plate medium," *Opt. Express*, vol. 24, no. 7, p. 7224, 2016.

[115] A. Cannizzo, "Ultrafast UV spectroscopy: from a local to a global view of dynamical processes in macromolecules.," *Phys. Chem. Chem. Phys.*, vol. 14, pp. 11205–23, aug 2012.

[116] P. Baum, S. Lochbrunner, and E. Riedle, "Tunable sub-10-fs ultraviolet pulses generated by achromatic frequency doubling," *Opt. Lett.*, vol. 29, p. 1686, jul 2004.

[117] I. Kozma, P. Baum, S. Lochbrunner, and E. Riedle, "Widely tunable sub-30 fs ultraviolet pulses by chirped sum frequency mixing," *Opt. Express*, vol. 11, p. 3110, nov 2003.

[118] B. Zhao, Y. Jiang, K. Sueda, N. Miyanaga, and T. Kobayashi, "Sub-15fs ultraviolet pulses generated by achromatic phase-matching sum-frequency mixing," *Opt. Express*, vol. 17, p. 17711, sep 2009.

[119] J. Liu, K. Okamura, Y. Kida, T. Teramoto, and T. Kobayashi, "Clean sub-8-fs pulses at 400 nm generated by a hollow fiber compressor for ultraviolet ultrafast pump-probe spectroscopy," *Opt. Express*, vol. 18, p. 20645, sep 2010.

[120] E. T. J. Nibbering, O. Dühr, and G. Korn, "Generation of intense tunable 20-fs pulses near 400 nm by use of a gas-filled hollow waveguide," *Opt. Lett.*, vol. 22, p. 1335, sep 1997.

[121] O. Dühr, E. T. J. Nibbering, G. Korn, G. Tempea, and F. Krausz, "Generation of intense 8-fs pulses at 400nm," *Opt. Lett.*, vol. 24, p. 34, jan 1999.

[122] T. Kanai, A. Suda, S. Bohman, M. Kaku, S. Yamaguchi, and K. Midorikawa, "Pointing stabilization of a high-repetition-rate high-power femtosecond laser for intense few-cycle pulse generation," *Appl. Phys. Lett.*, vol. 92, no. 6, pp. 90–93, 2008.

[123] Y.-Y. Liu, K. Zhao, P. He, H.-D. Huang, H. Teng, and Z.-Y. Wei, "High-Efficiency Generation of 0.12 mJ, 8.6 Fs Pulses at 400nm Based on Spectral Broadening in Solid Thin Plates," *Chinese Phys. Lett.*, vol. 34, p. 074204, jul 2017.

[124] J. E. Beetar, S. Gholam-Mirzaei, and M. Chini, "Spectral broadening and pulse compression of a 400 μ J, 20 W Yb:KGW laser using a multi-plate medium," *Appl. Phys. Lett.*, vol. 112, p. 051102, jan 2018.

[125] C. G. Durfee, S. Backus, H. C. Kapteyn, and M. M. Murnane, "Intense 8-fs pulse generation in the deep ultraviolet.," *Opt. Lett.*, vol. 24, pp. 697–9, may 1999.

[126] A. E. Jailaubekov and S. E. Bradforth, "Tunable 30-femtosecond pulses across the deep ultraviolet," *Appl. Phys. Lett.*, vol. 87, p. 021107, jul 2005.

[127] T. Nagy and P. Simon, "Generation of 200-microJ, sub-25-fs deep-UV pulses using a noble-gas-filled hollow fiber.," *Opt. Lett.*, vol. 34, pp. 2300–2, aug 2009.

[128] Y. Kida, J. Liu, T. Teramoto, and T. Kobayashi, "Sub-10 fs deep-ultraviolet pulses generated by chirped-pulse four-wave mixing.," *Opt. Lett.*, vol. 35, pp. 1807–9, jun 2010.

[129] T. Fuji, T. Horio, and T. Suzuki, "Generation of 12 fs deep-ultraviolet pulses by four-wave mixing through filamentation in neon gas," *Opt. Lett.*, vol. 32, p. 2481, sep 2007.

[130] T. Fuji, T. Suzuki, E. E. Serebryannikov, and A. Zheltikov, "Experimental and theoretical investigation of a multicolor filament," *Phys. Rev. A - At. Mol. Opt. Phys.*, vol. 80, no. 6, pp. 2–6, 2009.

[131] M. Ghotbi, P. Trabs, and M. Beutler, "Generation of high-energy, sub-20-fs pulses in the deep ultraviolet by using spectral broadening during filamentation in argon.," *Opt. Lett.*, vol. 36, pp. 463–5, feb 2011.

[132] S. Backus, J. Peatross, Z. Zeek, a. Rundquist, G. Taft, M. M. Murnane, and H. C. Kapteyn, "16-fs, 1-microJ ultraviolet pulses generated by third-harmonic conversion in air.," *Opt. Lett.*, vol. 21, pp. 665–7, may 1996.

[133] U. Graf, M. Fieß, M. Schultze, R. Kienberger, F. Krausz, and E. Goulielmakis, "Intense few-cycle light pulses in the deep ultraviolet," *Opt. Express*, vol. 16, p. 18956, nov 2008.

[134] F. Reiter, U. Graf, M. Schultze, W. Schweinberger, H. Schröder, N. Karpowicz, A. M. Azzeer, R. Kienberger, F. Krausz, and E. Goulielmakis, "Generation of sub-3 fs pulses in the deep ultraviolet.," *Opt. Lett.*, vol. 35, pp. 2248–50, jul 2010.

[135] A. Ravasio, D. Gauthier, F. R. N. C. Maia, M. Billon, J.-P. Caumes, D. Garzella, M. Géléoc, O. Gobert, J.-F. Hergott, A.-M. Pena, H. Perez, B. Carré, E. Bourhis, J. Gierak, A. Madouri, D. Mailly, B. Schiedt, M. Fajardo, J. Gautier, P. Zeitoun, P. H. Bucksbaum, J. Hajdu, and H. Merdji, "Single-Shot Diffractive Imaging with a Table-Top Femtosecond Soft X-Ray Laser-Harmonics Source," *Phys. Rev. Lett.*, vol. 103, p. 028104, jul 2009.

[136] J. Miao, T. Ishikawa, I. K. Robinson, and M. M. Murnane, "Beyond crystallography: Diffractive imaging using coherent x-ray light sources," *Science (80-.).*, vol. 348, pp. 530–535, may 2015.

[137] P. H. Bucksbaum, "The Future of Attosecond Spectroscopy," *Science (80-.).*, vol. 317, pp. 766–769, aug 2007.

[138] C. Vozzi, R. Torres, M. Negro, L. Brugnera, T. Siegel, C. Altucci, R. Velotta, F. Frassetto, L. Poletto, P. Villoresi, S. De Silvestri, S. Stagira, and J. P. Marangos, "High harmonic generation spectroscopy of hydrocarbons," *Appl. Phys. Lett.*, vol. 97, p. 241103, dec 2010.

[139] G. V. Marr, *Handbook on Synchrotron Radiation: Vacuum Ultraviolet and Soft X-ray Processes*. Handbook on Synchrotron Radiation, Elsevier Science, 2013.

[140] M. W. Guetg, A. A. Lutman, Y. Ding, T. J. Maxwell, F.-J. Decker, U. Bergmann, and Z. Huang, "Generation of High-Power High-Intensity Short X-Ray Free-Electron-Laser Pulses," *Phys. Rev. Lett.*, vol. 120, p. 014801, jan 2018.

[141] A. J. Verhoef, A. Mitrofanov, A. Zheltikov, and A. Baltuška, "Plasma-blueshift spectral shear interferometry for characterization of ultimately short optical pulses," *Opt. Lett.*, vol. 34, p. 82, jan 2009.

[142] A. Blättermann, C. Ott, A. Kaldun, T. Ding, V. Stooß, M. Laux, M. Rebholz, and T. Pfeifer, "In situ characterization of few-cycle laser pulses in transient absorption spectroscopy," *Opt. Lett.*, vol. 40, p. 3464, aug 2015.

[143] E. Goulielmakis, M. Uiberacker, R. Kienberger, A. Baltuska, V. Yakovlev, A. Scrinzi, T. Westerwalbesloh, U. Kleineberg, U. Heinzmann, M. Drescher, and F. Krausz, "Direct measurement of light waves.," *Science*, vol. 305, pp. 1267–9, aug 2004.

[144] F. Frank, C. Arrell, T. Witting, W. A. Okell, J. McKenna, J. S. Robinson, C. A. Haworth, D. Austin, H. Teng, I. A. Walmsley, J. P. Marangos, and J. W. G. Tisch,

"Invited Review Article: Technology for Attosecond Science," *Rev. Sci. Instrum.*, vol. 83, p. 071101, jul 2012.

[145] J. L. Krause, K. J. Schafer, and K. C. Kulander, "High-order harmonic generation from atoms and ions in the high intensity regime," *Phys. Rev. Lett.*, vol. 68, pp. 3535–3538, jun 1992.

[146] S. Ghimire, A. D. DiChiara, E. Sistrunk, P. Agostini, L. F. DiMauro, and D. A. Reis, "Observation of high-order harmonic generation in a bulk crystal," *Nat. Phys.*, vol. 7, no. 2, pp. 138–141, 2011.

[147] S. Ghimire, A. D. DiChiara, E. Sistrunk, G. Ndabashimiye, U. B. Szafruga, A. Mohammad, P. Agostini, L. F. DiMauro, and D. A. Reis, "Generation and propagation of high-order harmonics in crystals," *Phys. Rev. A*, vol. 85, p. 043836, apr 2012.

[148] G. Ndabashimiye, S. Ghimire, M. Wu, D. A. Browne, K. J. Schafer, M. B. Gaarde, and D. A. Reis, "Solid-state harmonics beyond the atomic limit," *Nature*, vol. 534, pp. 520–523, jun 2016.

[149] Y. S. You, Y. Yin, Y. Wu, A. Chew, X. Ren, F. Zhuang, S. Gholam-Mirzaei, M. Chini, Z. Chang, and S. Ghimire, "High-harmonic generation in amorphous solids," *Nat. Commun.*, vol. 8, p. 724, dec 2017.

[150] G. G. Paulus, W. Nicklich, H. Xu, P. Lambropoulos, and H. Walther, "Plateau in above threshold ionization spectra," *Phys. Rev. Lett.*, vol. 72, pp. 2851–2854, may 1994.

[151] K. Varjú, P. Johnsson, J. Mauritsson, A. L'Huillier, and R. López-Martens, "Physics of attosecond pulses produced via high harmonic generation," *Am. J. Phys.*, vol. 77, pp. 389–395, may 2009.

[152] K. L., "High-Harmonic Generation," in *Adv. Solid State Lasers Dev. Appl.*, InTech, feb 2010.

[153] P. M. Paul, "Observation of a Train of Attosecond Pulses from High Harmonic Generation," *Science (80-.).*, vol. 292, pp. 1689–1692, jun 2001.

[154] L. Gallmann, C. Cirelli, and U. Keller, "Attosecond Science: Recent Highlights and Future Trends," *Annu. Rev. Phys. Chem.*, vol. 63, no. 1, pp. 447–469, 2012.

[155] F. Lépine, G. Sansone, and M. J. Vrakking, "Molecular applications of attosecond laser pulses," *Chem. Phys. Lett.*, vol. 578, pp. 1–14, jul 2013.

[156] M. J. J. Vrakking, “Attosecond imaging,” *Phys. Chem. Chem. Phys.*, vol. 16, no. 7, p. 2775, 2014.

[157] C. Winterfeldt, C. Spielmann, and G. Gerber, “Colloquium : Optimal control of high-harmonic generation,” *Rev. Mod. Phys.*, vol. 80, pp. 117–140, jan 2008.

[158] F. Silva, M. Miranda, S. Teichmann, M. Baudish, M. Massicotte, F. Koppens, J. Biegert, and H. Crespo, “Near to mid-IR ultra-broadband third harmonic generation in multilayer graphene: few-cycle pulse measurement using THG dispersion-scan,” *CLEO Sci. Innov.*, pp. CW1H—-5, 2013.

[159] A. Spott, A. Becker, and A. Jaroń-Becker, “Transition from perturbative to non-perturbative interaction in low-order-harmonic generation,” *Phys. Rev. A*, vol. 91, p. 023402, feb 2015.

[160] T. Witting, F. Frank, W. a. Okell, C. A. Arrell, J. P. Marangos, and J. W. G. Tisch, “Sub-4-fs laser pulse characterization by spatially resolved spectral shearing interferometry and attosecond streaking,” *J. Phys. B At. Mol. Opt. Phys.*, vol. 45, no. 7, p. 074014, 2012.